The Eurasia Proceedings of Science, Technology, Engineering & Mathematics

EPSTEM

VOLUME 39 ICONTECH CONFERENCE

ISSN: 2602-3199
ISBN: 978-625-93546-4-4

ICONTECH 2026: 6th International Conference on Technology (IConTech)
February 05- 08, 2026 Budapest, Hungary
Edited by: Prof.Dr. Sabri Kocer- Necmettin Erbakan University, Türkiye

The Eurasia Proceedings of Science, Technology, Engineering & Mathematics (EPSTEM)
ISSN: 2602-3199

IConTECH 2026

International Conference on Technology (IConTech)

Proceedings Book

Editor

Sabri Kocer
Necmettin Erbakan University, Türkiye

ISBN: 978-625-93546-4-4

Published by the ISRES Publishing

Address: Askan Mah. Akinbey Sok. No: 5-A/Konya/TÜRKİYE

Web: www.isres.org

Contact: isrespublishing@gmail.com

Dates: February 05- 08, 2026

Location: Budapest, Hungary

https://2026.icontechno.net

The Eurasia Proceedings of Science, Technology, Engineering & Mathematics (EPSTEM)
ISSN: 2602-3199

About Editor

Prof Dr. Sabri Kocer
Necmettin Erbakan University, Engineerıng Faculty, Department of Computer Engineering, Division of Computer Software, Türkiye
Email: skocer@erbakan.edu.tr

Language Editor

Lecturer Ceren Dogan
School of Foreign Languages, Necmettin Erbakan University, Türkiye
Email: cerendogan@erbakan.edu.tr

CONFERENCE PRESIDENT

Prof Dr. Sabri Kocer-Necmettin Erbakan University, Türkiye

SCIENTIFIC BOARD

Agata Mesjasz-Lech - Czestochowa University of Technology, Poland
Ahmad Manasrah - Al Zaytoonah University of Jordan, Jordan
Bogdan Patrut - Alexandru Ioan Cuza University , Romania
Dariusz Jacek Jakóbczak - Technical University of Koszalin, Poland
Ebba Ossiannilsson - Swedish Association for Distance Education, Swedish
Elena Raducan - Dunarea De Jos University, Romania
Eleonora Guseinoviene - Klaipeda University, Lithuania
Gabriel Delgado-Toral - Universidad Nacional Autónoma de México, Mexico
Isti Hidayah - Semarang State University, Indonesia
Jose Manuel Lopez Guede - University of Basque Country, Spain
Marija Stanıć - University of Kragujevac, Serbia
M. Hanefi Calp - Karadeniz Technical University, Türkiye
Mohamed Ahmed - Mansoura University, Egypt
Nicu Bızon - Pitesti University, Romania
Ossi Autio - University of Helsinki, Finland
Pandian Vasant - Teknology Petronas University, Romania
Philipp Rosenberger - University of Applied Science, Austria
Rajnalkar Laxman - Gulbarga University, India
Yiyang Chen - Soochow University (CN), China
Yousef Jaradat - Al Zaytoonah University of Jordan, Jordan
Zairi Ismael Rizman - MARA University of Technology, Malaysia
Zipporah Pewat Duguryıl - Federal College of Education, Nigeria

ORGANIZING COMMITTEE

Ahmad Manasrah - Al Zaytoonah University of Jordan, Jordan
Agata Mesjasz-Lech - Czestochowa University of Technology, Poland
Elena Raducan - Dunarea De Jos University, Romania
Hakan Yuksel - Isparta University of Applied Sciences, Türkiye
Mohammad Sarwar - Scialert, Dubai, United Arab Emirates
M. Hanefi Calp - Karadeniz Technical University, Türkiye
Mustafa Özhan Kalac - Manisa Celal Bayar University, Türkiye
Robert Beloiu - University of Pitesti, Romania
Ozgur Dundar - Necmettin Erbakan University, Türkiye
Selahattin Alan - Selcuk University, Türkiye
Yousef Jaradat - Al Zaytoonah University of Jordan, Jordan
Yusuf Uzun - Necmettin Erbakan University, Türkiye
Zairi Ismael Rizman - MARA University of Technology, Malaysia

Editorial Policies

ISRES Publishing follows the steps below in the procedings book publishing process.
In the first stage, the papers sent to the conferences organized by ISRES are subject to editorial oversight. In the second stage, the papers that pass the first step are reviewed by at least two international field experts in the conference committee in terms of suitability for the content and subject area. In the third stage, it is reviewed by at least one member of the organizing committee for the suitability of references. In the fourth step, the language editor reviews the language for clarity.

Review Process

Abstracts and full-text reports uploaded to the conference system undergo a review procedure. Abstracts will be evaluated on the basis of abstracts/proposals. The conference system allows the full text to be sent if the abstract is accepted. Participants must wait for the evaluation results after uploading their article abstracts to the conference system. If their abstracts are accepted, they can upload their full texts to the conference system. The full texts are then sent to at least two reviewers for review. **The conference has a double-blind peer-review process.** Any paper submitted for the conference is reviewed by at least two international reviewers with expertise in the relevant subject area. Based on the reviewers' comments, papers are accepted, rejected or accepted with revision. If the comments are not addressed well in the improved paper, then the paper is sent back to the authors to make further revisions. The accepted papers are formatted by the conference for publication in the proceedings.

Aims & Scope

In the past, accessing information was tiring both financially and morally, but today, thanks to technology, it is easier and faster to access information. With this feature, technology not only makes daily life easier, but also accelerates the developments in science. Therefore, the focus of the conference is to share the studies on the developments in technology and the applications of technology in fields such as science and engineering by the participants. Studies in the fields of technology are accepted to the conference.

The aim of the conference is to bring together researchers and administrators from different countries, and to discuss theoretical and practical issues in the field of technology. At the same time, being aware of the applications of technology in different fields (such as engineering) is among the objectives of the conference.

The Eurasia Proceedings of Science, Technology, Engineering & Mathematics (EPSTEM)
ISSN: 2602-3199

Articles: 1- 9

CONTENTS

The Eurasia Proceedings of Science, Technology, Engineering and Mathematics (EPSTEM)
ISSN: 2602-3199

The Eurasia Proceedings of Science, Technology, Engineering and Mathematics (EPSTEM), 2026

Volume 39, Pages 1-8

IConTech 2026: International Conference on Technology

Experimental Investigation on Tensile Property of Carbon Reinforced Composite Produced with Vacuum Bagging

Ekrem Nugayoglu
OSTIM Technical University

Yusuf Sahin
OSTIM Technical University

Ferhat Kadioglu
Ankara Yıldırım Beyazıt University

Abstract: In this study, carbon fiber reinforced epoxy composites (CFRP) were manufactured using the Vacuum Bagging Method (VBM). Twill woven carbon fibers with an areal weight of 245 g/m² were employed as the reinforcement material. The composite laminates were fabricated with a five-layer symmetric stacking sequence of $[0]_5$. Tensile tests were conducted in accordance with ASTM D3039 standards to evaluate mechanical properties, specifically tensile strength and elastic modulus. Furthermore, the fracture surfaces of the tested specimens were examined via fractographic analysis. The experimental results revealed that fiber orientation significantly influences the mechanical behavior of CFRP laminates. Specimens tested along the 0° fiber direction exhibited substantially higher tensile strength and modulus values compared to those tested at a 30° orientation. Fractographic analysis indicated that the 0° oriented samples showed predominantly brittle fracture characteristics, whereas specimens with a 30° orientation demonstrated more ductile behavior through shear-induced deformation. These findings underscore the critical role of fiber orientation in determining the mechanical performance and failure mechanisms of CFRP laminates.

Keywords: CFRP, Vacuum bagging, Tensile properties, Fractography, Fiber orientation

Introduction

Composite materials are new materials created by combining two or more materials with different physical or chemical properties, offering enhanced characteristics. These advanced composites are increasingly being used in industries such as aerospace, automotive, and oil and gas (Bhandary et al., 2012). The main reason composite materials are increasingly preferred in these industries is their lightweight structure and high rigidity properties, which make them suitable for demanding applications. Additionally, their superior properties, such as high impact resistance and the ability to maintain performance even at very high temperatures, offer significant advantages over traditional materials. Furthermore, composite materials are resistant to both corrosion and chemical effects (Cambell, 2010).

Composite materials are structures designed to achieve superior qualities that cannot be obtained individually by combining the unique properties of different types of materials. Such materials are typically formed by combining at least two different components, which come together without dissolving into one another during the process. One of the components is usually the reinforcing element that provides strength to the structure, while the other component is the matrix phase that surrounds and holds the reinforcement together (Cakır & Berberoglu, 2018).

In recent years, with developments in fiber technology, the use of technical fibers—particularly carbon fiber—with advantages such as lightness and corrosion resistance has become widespread in composite structures as reinforcement elements in various forms, with the aim of improving the weak points of brittle materials, reducing brittleness, and increasing strength. Carbon fiber-reinforced polymer composites offer high strength and stiffness in the plane of the layer, but their interlaminar mechanical performance is largely dependent on the properties of the matrix. Therefore, due to their high sensitivity to damage caused by impact and fatigue, and the difficulty or impossibility of repairing damage, there is a need for structural reinforcement (Cakır & Berberoğlu, 2018; Korkmaz et al., 2017). When used as a reinforcement material in composite structures, epoxy resin provides significant improvements in properties such as chemical resistance, hardness, toughness, and abrasion resistance. However, it is also known that epoxy resins increase the brittleness of the structure **(**Srinivas Bhagyashekar, 2021). Composite materials tend to accumulate damage within their structure, and this damage may not always be visible to the naked eye or appear in a macroscopic form. In the structure, various types of damage can develop, such as fiber breakage, interlaminar delamination, cracking in opposing layers, and microcracks within the matrix. Therefore, the application of mechanical tests such as tensile tests and the determination of the composite material's durability properties are critical requirements**.**

It is widely accepted that the stress relaxation behavior of fiber-reinforced composite panels is directly related to the amount and distribution of fiber contents (Ozen, 2017). The mechanical and physical properties of polymer-based hybrid composites are fundamental characteristics that determine the overall performance of these materials. In order to predict the tensile behavior of these composites, some semi-empirical mathematical expressions have been developed. The Rule of Mixtures (ROM) models, which have a relatively simple structure, can estimate the tensile properties of composites within upper and lower limits and provide results that are comparable to experimental data. These models have been developed over time and enriched in various ways, forming a fundamental structure in the numerical analysis of hybrid composites (Pant &Palsule, 2024). Such computational models enable a more accurate and detailed characterization of composite materials by revealing the decisive effect of fiber length distribution on tensile properties (Aziz et al.,2013).

One of the simplest and lowest-cost methods in composite part production is the hand lay-up technique. However, since sufficient compression pressure is not applied to the laminates in this method, the quality of the products obtained is generally low. The vacuum bagging technique was developed to overcome this problem. This method helps to reduce excess resin during the curing process and remove moisture, solvents, and volatile components. Although this method produces high-quality composite laminates with very low void content, it has some disadvantages, such as high cost, long curing time, and limitations on the size and geometry of the parts that can be produced (Norafizal, 2020). In VBO method, atmospheric pressure is applied to the laminate throughout the curing cycle to exert a homogeneous compression force. VBO offers advantages such as more balanced pressure distribution, high fiber volume ratio, and shorter setup time. However, despite these advantages, defects such as void formation and residual stress may occur depending on the production process (Francucci et al. 2018).In this study, carbon-reinforced composite material was produced using the vacuum bagging method within a stacking sequences of $[0]_5$, and then cut parallel to the fiber axis (0°), and at an angle to the fiber axis (30°). Tensile tests were then performed on these samples to examine their tensile strength/modulus properties, and their fracture surfaces were examined.

Materials and Methods

Properties of Composite Components

The reinforcement phase consisted of KCF3K TW245 twill-woven carbon fiber prepreg, impregnated with the OM13 epoxy resin system (KORDSA). The carbon fabric features an areal weight of 245 g/m², a nominal thickness of 0.2 mm, and a warp/weft density of 0.61 yarns/mm. The underlying fiber is Toray T300. The matrix system has a nominal resin content of 42% (www.kordsglobal.com). Table 1 shows the physical and mechanical properties of fiber and resin (Manufacturer Data)

Table 1. Physical and mechanical properties of fiber and resin (Manufacturer data)

Feature	Unit	Resin (OM13)	Fiber (T300)
Tensile Strength	MPa	70	3500
Elastic Modulus	GPa	2.5	230
Density	g/cm³	1.20	1.75

Production Stages

Composite laminates were fabricated using the Vacuum-Assisted Bag Molding (VBO) method. Five layers of 400 mm × 400 mm prepreg were stacked in a symmetric $[0^o]_5$ orientation. The layup and bagging sequence followed these steps:

1. Mold Preparation: Application of a release agent to the tool surface.
2. Stacking: Manual layup of the five TW245 prepreg layers.
3. Consolidation Materials: Placement of a perforated release film, breather fabric, and vacuum manifold (flow net).
4. Vacuum Bagging: Sealing the assembly with a vacuum bag and mastic sealant tape.
5. Curing: A dual-stage cycle was used: pre-curing at 90 °C for 30 minutes, followed by a full cure at 130 °C for 2 hours, as per the resin's technical data sheet.

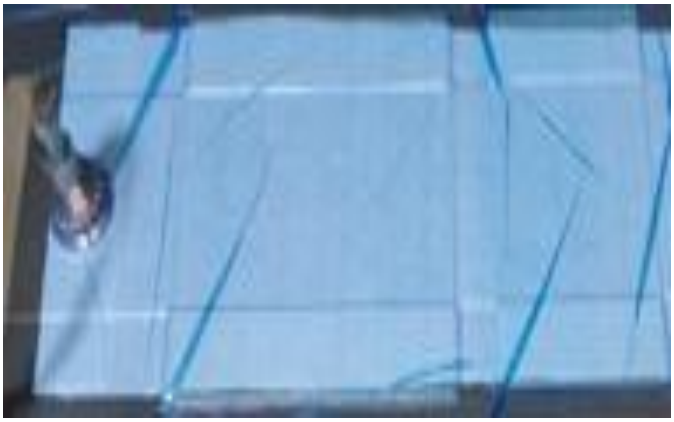

Figure 1**.** VB technique and its application of vacuum.

Sample Preparation and Tensile Testing

Following ASTM D3039 standards, 10 specimens were extracted from the cured panels (250 mm x 25 mm x ~1 mm). Five specimens were cut at **0°** (longitudinal) and five at **30°** (off-axis). The mass data measured during production is presented in Table 2.

Table 2. Production mass data

Configuration	Surface Area (m2)	Dry Fiber (g)	Resin (g)	Total Prepreg (g)
1 Layer (Full)	1.00	245.0	115.0	360.0
5 Layers (Full)	0.80	196.0	92.0	288.0
5 Layers (1 Sample)	0.00625	7.65	3.59	11.25

Tensile tests were performed in accordance with ASTM D3039 standard. Tensile testing was conducted on a Besmak BMT-60E machine at a constant crosshead speed of 2 mm/min.

Results and Discussion

Tensile Behavior

Tensile test results of composite samples cut at different orientation angles to the fiber axis are shown in Table 3 and Figures 2, & 3, respectively. The tensile properties of the composite specimens, categorized by their orientation angles, are detailed in Table 3. Stress-strain profiles were generated for both the 0^o and 30^o configurations to evaluate the influence of fiber alignment on mechanical performance.

For the 0^o samples, the load is primarily sustained by the carbon fibers. The maximum tensile strength reached 302.64 MPa, with an average strength (sigma) of 287.26 MPa. The stress-strain behavior in this orientation is characterized by high linearity, reflecting the dominant influence of the high-modulus carbon fibers. For the elastic modulus, the average modulus was calculated at 23.93 GPa. In terms of strain, most samples exhibited

failure at low strain levels (approx. 12.%–1.5%), confirming the brittle nature of the carbon/epoxy system when loaded longitudinally. One outlier reached a strain of 6%, which may be attributed to localized grip effects or minor fiber misalignment.

For the 30° Off-Axis Samples, the 30º specimens showed a marked decrease in mechanical properties. In this orientation, the matrix must transfer load through shear, leading to lower strength and increased deformation. Tensile strength indicated that the average stress dropped to 118.29 MPa (a ~59% reduction compared to 0º sample). As for the ductility, the 30º oriented samples demonstrated significantly higher strain at maximum stress (averaging ~0.11), representing a more ductile failure mode as the epoxy matrix undergoes plastic deformation.

Table 3. Tensile test results

Sample Set	Max Stress σu (MPa)	Avg. Stress σm (MPa)	Avg. Modulus (GPa)	SD	CV (%)
0° Orientation	302.64	287.26	23.93	12.23	4.25
30° Orientation	122.88	118.29	8.91	2.83	2.39

Statistical Analysis

The Standard Deviation (SD) and Coefficient of Variation (CV) were calculated using the following relationships:

$$SD = \sqrt{(\sigma_u - \sigma_m)2/N - 1} \quad (1)$$

$$CV = \frac{SD}{\sigma_m} * 100 \quad (2)$$

The low CV values (4.25% for 0º sample and 2.39% for 30o sample) indicate high manufacturing consistency and repeatability of the Vacuum Bagging Method (VBM). This suggests that the vacuum pressure effectively minimized voids and ensured a uniform resin distribution across all samples.

This is consistent with the previous studies carried out on tensile behavior of the polymeric composites, 0º oriented samples exhibited better performance than those of other orientations in the literature (Harper et al., 2009; Şahin 2024; Cecen & Sarıkanat 2008; Ozsoy et al., 2015). Whereas, this is not always the case. For instances, some others studies conducted on mechanical behaviour of the composites indicated that 90º oriented laminates have been reported to be higher properties in the literature, specially basalt fiber-reinforced composites (Sahin & Selek, 2025; Abdua & Ibrahim, 2025; Kumar & Singh, 2021).

Figure 3 illustrates the stress-strain behavior for composite samples cut at a 30° orientation. The curves reveal a mechanical response fundamentally different from the 0° longitudinal samples. In transition from Linear to Non-Linear region, the specimens exhibit an initial linear-elastic region followed by a pronounced non-linear region prior to failure. This transition indicates the onset of matrix yielding and inter-fiber shear. The dominant failure mechanism in this orientation is matrix-shear. Because the fibers are not aligned with the loading axis, the epoxy resin must bear a significant portion of the stress, leading to the observed ductile behavior. The average tensile strength was recorded at 118.29 MPa while the average elastic modulus for this group was significantly lower than the 0° samples, calculated at 8.91 GPa. The strain at failure was considerably higher than the longitudinal samples, with some specimens reaching decimal strain values of 0.15–0.16 (15-16% elongation). It can be noted that the provided graph in Fig. 3 shows most samples exceeding (10%) strain. Finally, Table 4 illustrates the summary of orientation comparisons for both tested composite laminates.

Table 4. Summary of orientation comparison

Property	0° Orientation	30° Orientation
Average strength	287.26 MPa	118.29 MPa
Average modulus	23.93 GPa	8.91 GPa
Ductility	Brittle (Linear)	Ductile (Non-linear)
Dominant phase	Fiber-dominant	Matrix-shear dominant

The 30° specimens indicated ductility behaviour. Because these are cut from a $[30^o]_5$ plate at an angle, the "30° specimens" will rely heavily on the inter-laminar shear of the OM13 resin, which has a much lower modulus (2.5 GPa) than the fiber. Based on the Table 1, the fiber-to-resin ratio is excellent.

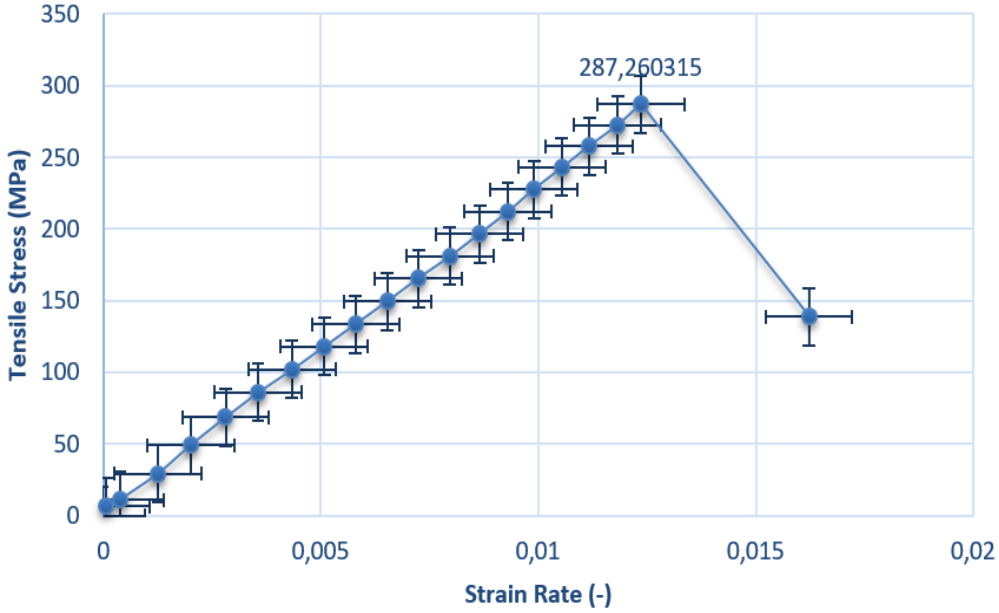

Figure 2. Stress-strain graphs of samples cut at 0° fiber direction

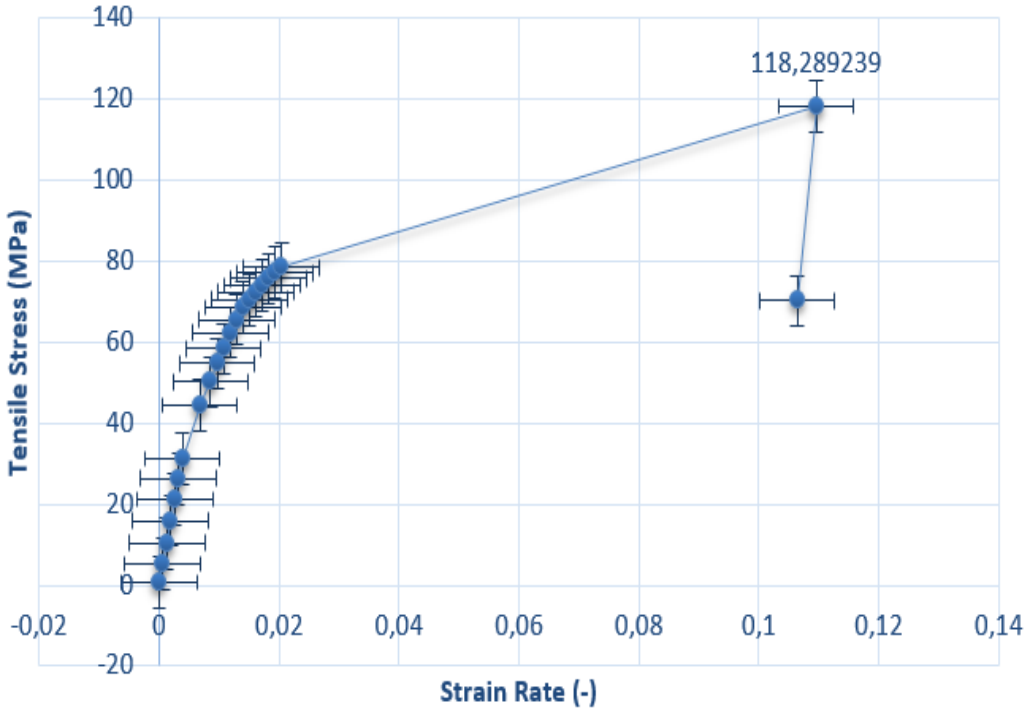

Figure 3. Stress-strain graphs of samples cut at 30° fiber direction

Fracture Surfaces

The fracture surface images of the samples after the tensile test are shown in Figure 4 (a, b), respectively. Labels were affixed to each sample to prevent them from being mixed up. For example, the label 0° indicates that this sample was cut at 0° to the fiber direction. It can seen that flat-fracture surface was observed due to indicating a brittle behavior, three of the samples are fractured along the gauge length of the samples, but other fractured close to critical region. Figure 4 (b) exhibits the fracture surfaces of 30° oriented samples subjected to tensile testing. Fracture surface shows angle-ply surface because the efficiency of load transfer decreases as the angle deviates from the fiber direction. Fibers can be acted as the zig-zag movements to change their positions in the resin. In other words, resin also becomes dominant role, instead of carrying the load by fiber reinforcements, hence resulting in a lower tensile and modulus.

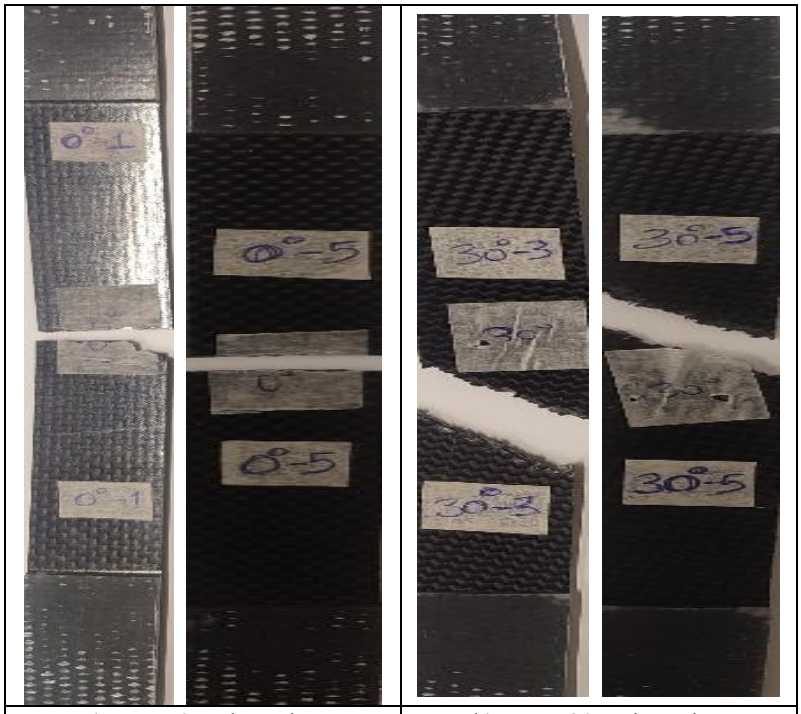

a) 0º orientation b) 30º orientation

Figure 4. Fracture surfaces of two oriented samples after tensile testing

As a result, the experimental investigation confirms that the VBM produces high-quality CFRP laminates with low coefficient of variation. Fiber orientation is the primary determinant of both the magnitude of strength and the mode of failure. While 0° orientations provide maximum structural stiffness, 30° orientations allow for significantly higher energy absorption through matrix deformation. The limited load-carrying capacity of the fibers at 30° angle, the more dominant role of the matrix, and increased shear stresses have led to a decrease in modulus and strength values. Moreover, the stress-strain curves obtained show that the 0° specimens exhibit brittle fracture behavior due to presence of fiber, while the 30° specimens exhibit a more ductile deformation tendency.

Conclusions

In this study, the tensile properties of twill-woven carbon fiber/epoxy composites fabricated via the Vacuum Bagging Method (VBM) were experimentally investigated across two distinct orientations (0º and 30º). The following conclusions were drawn:

1. Experimental results confirm that fiber orientation exerts a decisive influence on the tensile performance and failure mechanisms of CFRP laminates.
2. The highest mechanical properties were achieved in the 0º fiber direction, yielding an average tensile strength of 287.26 MPa and an elastic modulus of 23.93 GPa.
3. Off axis of 30º orientation deviation from the primary fiber axis resulted in a significant reduction in mechanical integrity, with tensile strength falling to 118.29 MPa and the elastic modulus decreasing to 8.9 GPa.
4. Fractographic analysis have shown that 0° oriented specimens exhibit predominantly brittle fracture characteristics due to the load-carrying capacity of the fibers. However, in the 30° oriented specimens, the role of the matrix became more pronounced, leading to a more ductile deformation tendency in these specimens.
5. .It has been confirmed that the vacuum bagging method is an effective methodology for producing high-quality composite panels by ensuring a low void ratio and homogeneous resin distribution.
6. Experimental data has proven that precise control of fiber orientation and production parameters in composite designs is critical for the final mechanical strength. The effectiveness of the vacuum bagging method (VBM) in the production process has been confirmed by the low coefficient of variation (CV) values obtained.

Scientific Ethics Declaration

* The authors declare that the scientific ethical and legal responsibility of this article published in EPSTEM journal belongs to the authors.

Conflict of Interest

* The authors declare that they have no conflicts of interest.

Funding

* During this study no funding is available.

Acknowledgements or Notes

* This article was presented as an oral presentation at the International Conference on Technology (www.icontechno.net) held in Budapest/Hungary on February 05-08, 2026.

* We would like to thank ACME Kompozit Ltd.for providing support in manufacturing the composites for their workshop in OSTIM Organize Sanayi.

References

Abdua, A. N. F., & Nik Ibrahim, N. N. (2025). The effect of fibre orientation on the density and tensile properties of basalt fibre/epoxy composites. *Journal of Mechanical Engineering, 22*(1), 46–57.

Aziz, S., Rashid, S., & Mohd Salleh, M. A. (2013). Theoretical prediction of CNT-CF/PP composite tensile properties using various numerical modeling methods. *Fullerenes, Nanotubes and Carbon Nanostructures, 21*(5), 411–416.

Bhandary, S., Sanyal, B., & Wang, M. (2012). Composites and their properties. In N. Hu (Ed.), *Composites and their properties*. InTech Open.

Brillant, M. (2011). *Out-of-autoclave manufacturing of complex shaped composite laminates* (Master's thesis, McGill University).

Campbell, F. C. (2010). *Structural composite materials*. ASM International.

Cecen, V., & Sarıkanat, M. (2008). Experimental characterization of traditional composites manufactured by vacuum assisted resin transfer molding. *Journal of Applied Polymer Science, 107*(3), 1822–1830.

Çakır, M., & Berberoğlu, B. (2018). E-cam elyaf takviyeli epoksi matrisli kompozit malzemelerin elyaf oranındaki artış ile mekanik özelliklerindeki değişimlerin incelenmesi (Investigation of changes in mechanical properties of e-glass fiber reinforced epoxy matrix composite materials with increase of fiber ratio). *El-Cezeri, 5*(3), 734–740.

Francucci, G., Palmer, S., & Hall, W. (2018). External compaction pressure over vacuum-bagged composite parts: Effect on the quality of flax fiber/epoxy laminates. *Journal of Composite Materials, 52*(1), 3–15.

Harper, L., Turner, T., Martin, J., & Warrior, N. (2009). Fiber alignment in directed carbon fiber preforms – A feasibility study. *Journal of Composite Materials, 43*(1), 57–74.

İmak, A., Solmaz, M. Y., & Topkaya, T. (2016). Tabakalı hibrit kompozit malzemelerin yorulma davranışlarının analizi (The analysis of fatigue behaviours of the laminated hybrid composite materials). *El-Cezeri, 3*(3), 448-458.

Korkmaz, N., Çakmak, E., & Dayık, M. (2016). Dokuma karbon elyaf takviyeli karbon nano tüp-epoksi kompozit malzemelerin mekanik ve termal karakterizasyonu (Mechanical and termal characterization of woven carbon fiber reinforced carbon nanotube-epoxy composites). *Süleyman Demirel Üniversitesi Fen Bilimleri Enstitüsü Dergisi, 20*(2), 338–353.

Kumar, N., & Singh, A. (2021). Study the effect of fiber orientation on mechanical properties of bidirectional basalt fiber reinforced epoxy composites. *Materials Today: Proceedings, 39*, 1581–1587.

Mujahid, Y. (2020). Effects of processing parameters for vacuum-bagging-only method on shape conformation of laminated composites. *Processes, 8*(9), 1147–1153.

Norafizal, A. I. B. (2020). *Effects of vacuum bagging techniques on mechanical properties of carbon epoxy laminates* (Bachelor's thesis, Universiti Teknologi Petronas).

Ozsoy, N., Mimaroğlu, A., & Ozsoy, M. (2015). Comparison of mechanical behavior of carbon and glass fiber reinforced epoxy composites. *Acta Physica Polonica A, 127*, 1032–1034.

Özen, M. (2017). E-cam/epoksi kompozitlerde lif doğrultularının gerilme gevşeme davranışı üzerindeki etkisi (The effect of fiber directions on stress – Relaxation behavior of eglass/epoxy composites). *Fırat Üniversitesi Mühendislik Bilimleri Dergisi, 29*(1), 219–224.

Pant, M., & Palsule, S. (2024). Prediction of tensile properties of natural fiber reinforced PP hybrid composites by Facca-Kortschot-Yan (FKY) and Palsule equations. In *Journal of Physics: Conference Series, 2837*(1), 012005.

Sahin, Y. (2024). Mechanical and thermal property of carbon fiber reinforced composites. *Advances in Science and Technology, 158*, 43–54.

Sahin, Y., & Selek, S. (2025). Effect of fiber orientation on tensile property of basalt reinforced epoxy composite. *The Eurasia Proceedings of Science, Technology, Engineering and Mathematics, 38*, 551–558.

Srinivas, K., & Bhagyashekar, M. S. (2021). Prediction of mechanical properties of epoxy composites containing mono and hybrid particulate fillers. In *IOP Conference Series: Materials Science and Engineering, 1189*(1), 012003.

Uzay, Ç., Çetin, A., Geren, N., Bayramoğlu, M., & Tütüncü, N. (2024). Predicting the tensile stiffness and strength properties of plain woven carbon fiber/epoxy laminates: A practical analytical approach and experimental validations. *Mechanics of Advanced Materials and Structures, 31*(12), 2619–2634.

Author(s) Information

Ekrem Nugayoglu
OSTIM Technical University, Department of Mechanical Engineering Department, OSTIM, 100. Yıl Bulvarı, 55/F, 06374 Yenimahalle/Ankara/Türkiye
ORCID iD: https://orcid.org/0009-0008-6093-1161
*Contact e-mail: *ekrem.nugayoglu@ostimteknik.edu.tr*

Yusuf Sahin
OSTIM Technical University, Department of Mechanical Engineering Department, OSTIM, 100. Yıl Bulvarı, 55/F, 06374 Yenimahalle/Ankara/Türkiye
ORCID iD: https://orcid.org/0000-0001-9615-6437

Ferhat Kadioglu
Ankara Yıldırım Beyazıt University, Department of Aerospace/Aeronatical Engineering, Ayvalı Mah. Gazze Cad. No: 7 Etlik-Keçiören/Ankara/Türkiye
Orcid iD: https://orcid.org/0000-0002-9955-3435

*Corresponding authors contact e-mail

To cite this article:

Nugayoglu, E., Sahin, Y., & Kadioglu, F. (2026). Experimental investigation on tensile property of carbon reinforced composite produced with vacuum bagging. *The Eurasia Proceedings of Science, Technology, Engineering and Mathematics (EPSTEM), 39,* 1-8.

The Eurasia Proceedings of Science, Technology, Engineering and Mathematics (EPSTEM)
ISSN: 2602-3199

The Eurasia Proceedings of Science, Technology, Engineering and Mathematics (EPSTEM), 2026

Volume 39, Pages 9-18

IConTech 2026: International Conference on Technology

A Comparative Study of Controller Performance in Five-Phase Induction Motor Drives

Taieb Bessaad
Hassiba Benbouali University of Chlef

Maamar Latrouche
Hassiba Benbouali University of Chlef

Aicha Aissa Bokhtache
Hassiba Benbouali University of Chlef

Azzedine Khati
Hassiba Benbouali University of Chlef

Khedidja Benaicha-Mati
Hassiba Benbouali University of Chlef

Abstract: In many applications where lowering the per-phase power draw while maintaining high system reliability is crucial, multiphase machines are increasingly seen as an attractive alternative to traditional three-phase machines. This trend has been strongly supported by recent research in the field. Fuzzy control techniques have proven effective for handling complex systems, but they often struggle when parameters change significantly over a broad range. Our work tackles this limitation through an adaptive fuzzy controller. In the context of vector-controlled induction motor drives and a five-phase asynchronous machine, the proposed approach deploys a control behavior model (CBM) to ensure robust performance even under abrupt load changes, rotor resistance variations and altered rotor inertia. Simulation results confirm that the adaptive fuzzy controller outperforms both standard fuzzy logic control and classical controllers, particularly in extreme parameter cases (e.g., $R_r = 200\ \% R_{rn}$, $L_m = 0.8 \times L_{mn}$ and $J = 200\ \% J{=}n$).

Keywords: Five-phase asynchronous motor, Indirect vector control, Control behavior model, Fuzzy control, Adaptive fuzzy control, Robustness

Introduction

The adoption of multiphase machines has surged in recent years as power levels increase and high-reliability electrical applications demand better distribution of power by using more than three phases (Yepes et al., 2022; Kulandaivel et al., 2023). In addition to efficient power sharing, multiphase machines bring several noteworthy advantages: they allow lower phase voltages without raising phase currents, they reduce iron losses and torque ripple, increase the torque ripple frequency, and deliver improved fault tolerance (Laksar et al., 2021; Yepes et al., 2022). Thanks to these benefits, multiphase machines are increasingly found in high-power contexts such as wind generation, more-electric aircraft, ship propulsion and mining systems (Kulandaivel et al., 2023).

Despite their promise and intrinsic robustness, controlling multiphase machines is inherently more challenging than controlling DC machines because their mathematical models are highly nonlinear and strongly coupled (Duran et al., 2008; Xue, 2023). As a result, advanced control methods are required. Modern control approaches such as state-feedback control, direct torque control (DTC), vector control and adaptive control are now

commonly employed (Hosseyni et al., 2018; Mehedi et al., 2017). While traditional PI controllers remain popular due to their simplicity, their performance degrades under large parameter shifts or external disturbances (Elbarbary et al., 2024; Belhamdi & Goléa, 2021). To address these limitations, intelligent control frameworks—including sliding mode control, fuzzy logic, neural networks and adaptive schemes—have been increasingly used (Tidke & Chowdhury, 2024; Bouzidi, 2024). Integrating adaptive control with robust fuzzy logic offers a more resilient solution and better tracking under uncertainty (Bessaad, 2019; Sumukh et al., 2025).

The objective of this study is to address these challenges by combining an adaptive scheme with a robust fuzzy logic controller, thereby enhancing overall performance and ensuring robustness even when machine parameters vary significantly. The aim of this work is to overcome this limitation, integrating adaptive control with the robust fuzzy controller offers a promising solution to enhance overall control performance and ensure stability, even in the face of significant parameter variations.

Model of an Induction Machine

The induction-machine model can be expressed using a state-space representation (Arahal et al., 2018). For a five-phase machine, the mathematical model is defined in the arbitrary reference frame d–q–x–y–o. Within this frame, the d and q axes handle the flux generation and torque production processes, while the x and y axes represent the loss-producing subspaces. The zero (o) component serves to preserve the total power balance within the system. The decoupling (transformation) matrix for the five-phase machine is formulated as shown by Chikondra et al. (2023).

$$A=\sqrt{\frac{2}{5}}\begin{bmatrix} 1 & \cos(\frac{2\pi}{5}) & \cos(\frac{4\pi}{5}) & \cos(\frac{4\pi}{5}) & \cos(\frac{2\pi}{5}) \\ 0 & \sin(\frac{2\pi}{5}) & \sin(\frac{4\pi}{5}) & \sin(\frac{4\pi}{5}) & \sin(\frac{2\pi}{5}) \\ 1 & \cos(\frac{4\pi}{5}) & \cos(\frac{8\pi}{5}) & \cos(\frac{8\pi}{5}) & \cos(\frac{4\pi}{5}) \\ 0 & \sin(\frac{4\pi}{5}) & \sin(\frac{8\pi}{5}) & -\sin(\frac{8\pi}{5}) & -\sin(\frac{4\pi}{5}) \\ \frac{1}{\sqrt{2}} & \frac{1}{\sqrt{2}} & \frac{1}{\sqrt{2}} & \frac{1}{\sqrt{2}} & \frac{1}{\sqrt{2}} \end{bmatrix} \tag{1}$$

$$\begin{cases} \delta L_S \frac{d}{dt} i_{sd} = -\left(R_S + \frac{L_m^2}{L_r} R_r \right) i_{sd} - \delta L_S \omega_S i_{sq} - \frac{L_m}{T_r L_r} \phi_{rd} \\ \qquad\qquad + v_{sd} \\ \delta L_S \frac{d}{dt} i_{sq} = -\left(R_S + \frac{L_m^2}{L_r} R_r \right) i_{sq} - \delta L_S \omega_S i_{sd} - \frac{L_m}{L_r} \omega_r \phi_{rd} \\ \qquad\qquad + v_{sq} \\ \frac{d}{dt} \phi_{rd} = \frac{L_m}{T_r} i_{sd} - \frac{1}{T_r} \phi_{rd} \\ \frac{d}{dt} \phi_{rq} = \frac{L_m}{T_r} i_{sq} - (\omega_S - \omega_r) \phi_{rd} \\ T_{em} = p \frac{L_m}{T_r} \left(\phi_{rd} i_{sq} - \phi_{rq} i_{sd} \right) \\ J \frac{d}{dt} \Omega = T_{em} - T_L - f\Omega \end{cases} \tag{2}$$

In which rotor time constant is $T_r = \frac{L_r}{R_r}$; the total leakage is $\delta = 1 - \frac{L_m^2}{L_S L_S}$; ϕ_{rd} is rotor flux relative to axis d ($\phi_{rd} = \phi_r$ for rotor field-oriented control); ϕ_{rq} is rotor flux relative to q- axis ($\phi_{rq} = 0$) ; i_{sd} is stator relative current to the d- axis ; i_{sq} is stator relative current to the q- axis ; Tem is electromagnetic torque; s,r are indices relating to the stator and rotor; L_s , L_r are inductance of stator and rotor windings respectively ; L_m is mutual inductance; J is inertia moment ; p is number of pole pairs ; K_f is Friction coefficient; Ω is electrical rotation speed.

In Fig. 1, one note the appearance of vector control blocks where PI controller is used for the two stator currents and the speed along the *d* and *q* axes then one replace this controller with FLC and BMC controller.

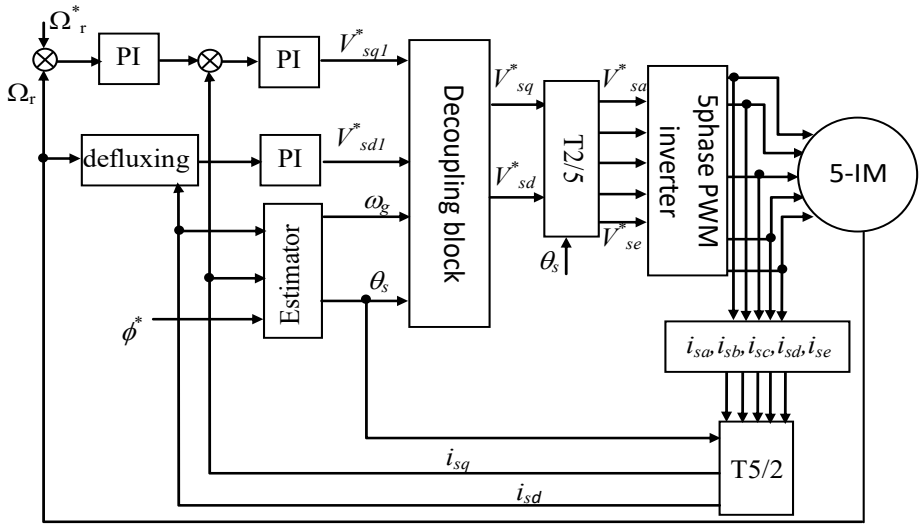

Figure1. A control method for a five-phase motor drive, utilizing an indirect rotor flux orientation technique.

Behavior Model Control Principles

In this article, the functions P(s) and M(s) are employed to represent, respectively, the plant (process) and its mathematical model. The Behavior Model Control (BMC) strategy enhances the control algorithm's effectiveness by incorporating supplementary control signals (Derugo, 2017). This method uses both a primary controller, denoted (FCp(S)) and an additive controller, (FCr(S)). The overall control structure is illustrated in Figure 2 (Morawiec et al., 2019).

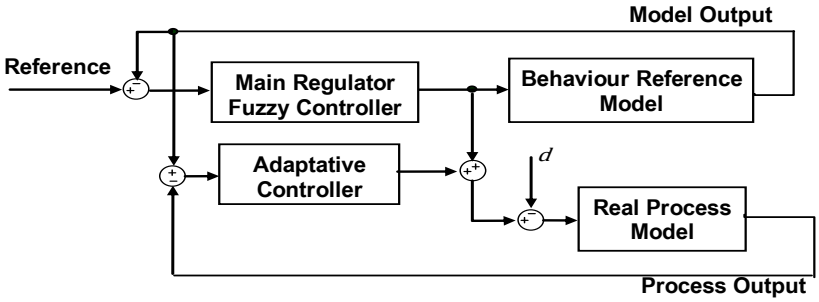

Figure 2. Structure of CBM (Control Behavior Model)

Note that the principal controller eliminates the error is calculated as the difference between the reference value Y_{ref} and the output value, which can be either the model output or the process output Y_{mod} or a process Y. Therefore, it is possible to define two CBM structures: first based on the output of the real process model, and a second based on an imposed model output. We can derive the following expressions (Fei et *al.*, 2018) based on the information presented in Figure 2, can be derived:

The main controller produces a control signal, u_{reg} , based on the reference value Y_{ref}.. This signal is then fed into a predefined behavior model, $F_M(S)$, which generates an output Y_{mod} . The difference between the model Y_{mod} and the actual process output Y is used by a secondary regulator, known as the adaptation controller, to compute an additional control signal, Δu_{reg}. By keeping the error ($Y - Y_{mod}$), constant, the process behavior aligns with the imposed model, which is the essence of behavior model control. The extra control Δu_{reg} is combined with the main controller output u_{reg} and applied to the real process $F_P(S)$.

This complementary control enhances the robustness of the overall system, allowing the imposed behavior to be maintained even in the presence of disturbances (Keighobadi et al., 2018). Furthermore, this approach enables

the linearization of nonlinear systems through the use of a linear reference model (Shihabudheen et al., 2018). It is important to note that the primary controller calculates the error as the difference between the reference YrefY_{\text{ref}}Yref and the output, which can either be the model output YmodY_{\text{mod}}Ymod or the process output YYY. Accordingly, two types of CBM structures can be defined: one based on the actual process output, and another based on the output of the imposed model. The corresponding expressions can be derived from the information shown in Figure 2 (Fei et al., 2018)

$$\begin{cases} Y(S) = \left[u_{reg}(S) + \Delta u_{reg}(S) - d\right] F_P(S) \\ \Delta u_{reg}(S) = \left[F_M(S) + u_{reg}(S) - Y(S)\right] F_{Cc}(S) \end{cases} \tag{3}$$

The system that expresses both the process output (Y) and the model output (Y_{mod}) is reached after the calculation as:

$$\begin{cases} Y(S) = \dfrac{F_P(S)(1 + F_M(S).F_{Cc}(S))}{1 + F_P(S).F_{Cc}(S)} u_{reg}(S) \\ \qquad\quad - \dfrac{F_P(S)}{1 + F_P(S).F_{Cc}(S)}.d \\ Y(S) = F_M(S).u_{reg}(S) \end{cases} \tag{4}$$

Where the disruption is denoted by d.

The following presumptions must be met by the behavior corrector $C_C(S)$:

$$\begin{cases} \left|F_M(S).F_{Cc}(S)\right| >> 1 \\ \left|F_P(S).F_{Cc}(S)\right| >> 1 \end{cases} \tag{5}$$

Simplifying results in the following:

$$\begin{cases} Y(S) = F_M(S).u_{reg}(S).\dfrac{1}{F_{Cc}(S)}.d \\ Y_{mod}(S) = F_M(S).u_{reg}(S) \end{cases} \tag{6}$$

The result of this is as follows:

$$Y(S) = Y_{mod}(S) - \frac{1}{F_{Cc}(S)}.d \tag{7}$$

At low disturbance, the process output (Y) and model output (Y_{mod}) are identical. If this disturbance is minimal in comparison to (Y) process output, it precisely corresponds to (Y_{mod}) model's output. These terms are written:

$$\frac{d}{F_{Cc}(S)} << F_M(S).u_{reg}(S) \tag{8}$$

When the return from the model output Y_{mod} is taken into account, the system (3) becomes:

$$\begin{cases} Y_{\text{mod}}(S) = \dfrac{F_M(S).F_{Cp}(S)}{1+F_M(S).F_{Cp}(S)}.Y_{ref}(S) \\ Y(S) = \dfrac{F_P(S)(1+F_M(S).F_{Cc}(S))}{F_M(S)(1+F_P(S).F_{Cc}(S))}.Y_{mod}(S) \\ \quad -\dfrac{F_P(S)}{1+F_P(S).F_{Cc}(S)}.d \end{cases} \tag{9}$$

Let's assume the following situation to simplify the transfer function:

$$\left|F_M(S).F_{Cc}(S)\right| >> 1 \tag{10}$$

Controller of Speed Loop

The input variables E and ΔE, along with the output variables, are represented by conventional triangular-shaped membership functions. Stator speeds are classified into seven fuzzy sets, while for stator currents, each membership is segmented into three fuzzy sets, as illustrated in Figure 4. The Center of Area (COA) approach is used to carry out the defuzzification process, and Mamdani (Max-Min) is the inference method used (Zhang et *al.*, 2021). The speed loop correction controller is employed to eliminate the difference between the machine's actual speed and the reference speed Ω_{mod} provided by the model. To achieve this, the controller uses both the error and its derivative as inputs. The resulting correction signal, T_{em}, which guides the five-phase machine to follow the model's behavior, is obtained by integrating the controller output (Arahal et al., 2018). The correction controller, denoted as FLCR (Figure 3), has a structure similar to that of a fuzzy logic main controller (FLC), consisting of three key components: a knowledge base, fuzzification (F), inference (I), and defuzzification (D). Here, the machine's speed Ω and stator currents (i_{sd} and i_{sq})are used as input variables u.

Both the error E and its change ΔE, along with the output variable, are described using conventional triangular membership functions. The stator speed is divided into seven fuzzy sets, whereas the stator currents are segmented into three fuzzy sets each, as shown in Figure 4. Defuzzification is carried out using the Center of Area (COA) method, and Mamdani's Max-Min approach is applied for inference (Zhang et al., 2021).

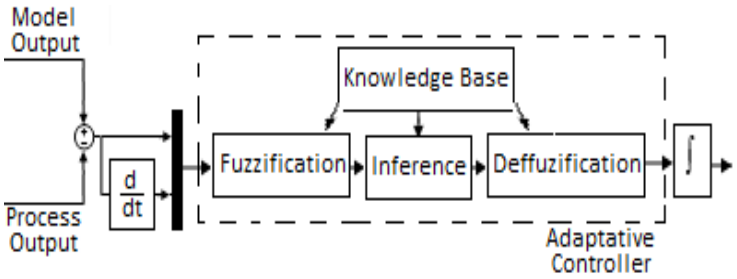

Figure 3. The fuzzy correction controller's structure FLCR

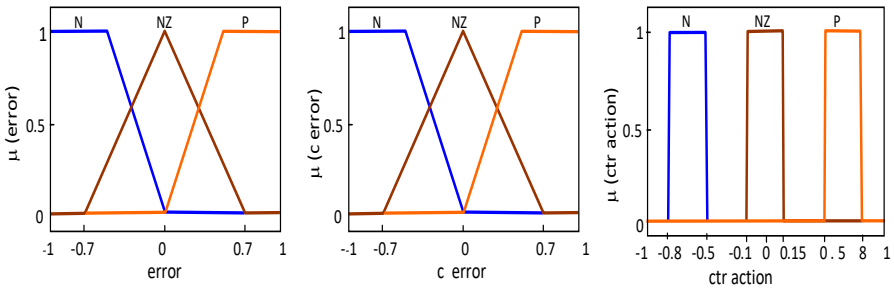

a

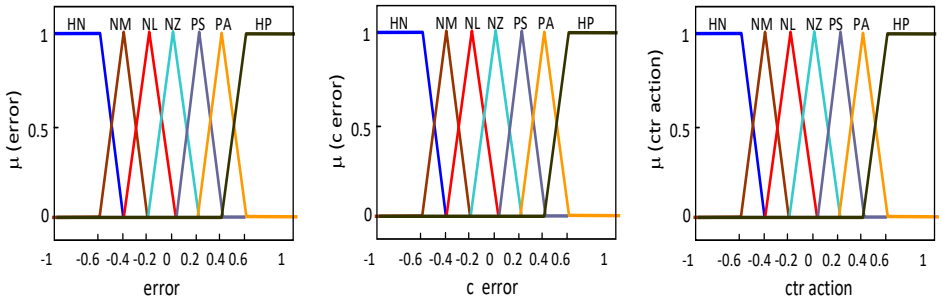

b

Figure 4. Input and output variables membership functions of representation:
a) Currents, b) Speed.

The following defines the various sets:
HN: High Negative;
PL: Positive low;
NZ: Near Zero;
NM: Negative Medium;
PA: Positive Average;
NL: Negative low;
HP: High Positive

Results and Discussion

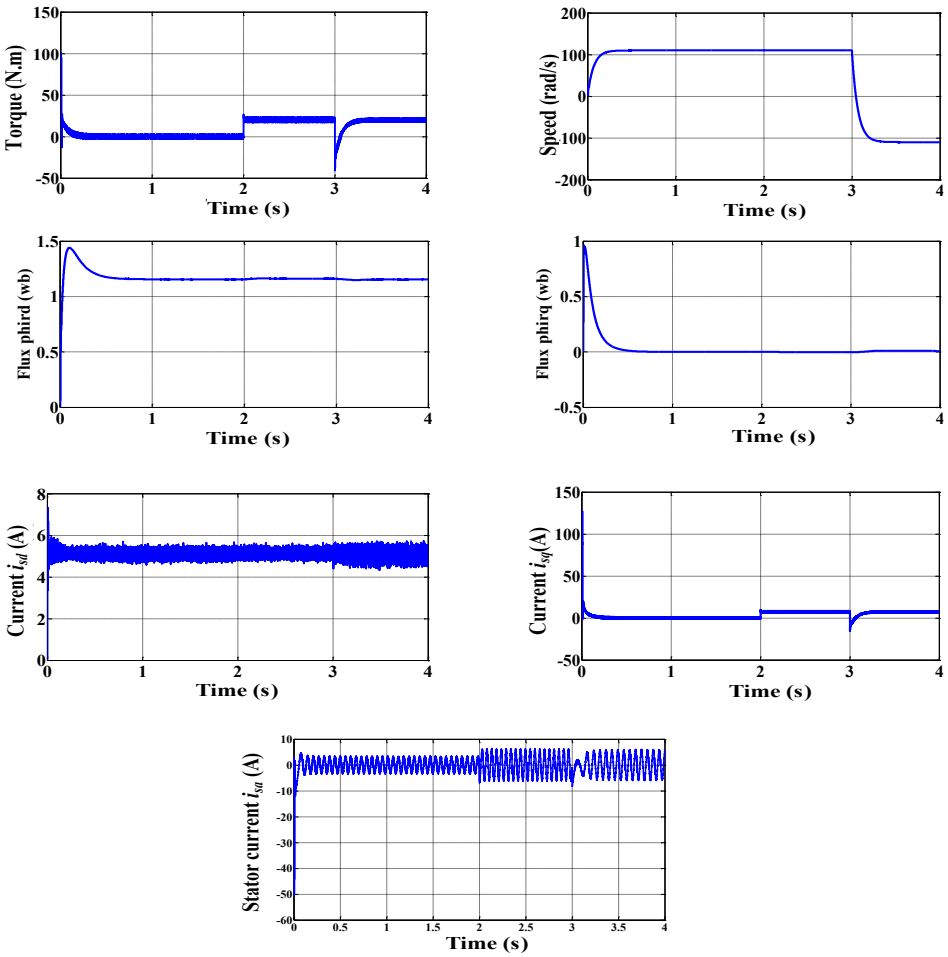

Figure 5. Performance of the 5-phase I.M with fuzzy adaptive regulators in indirect vector control during speed reversal

The simulations were executed within a MATLAB environment where the differential equations describing the dynamic behavior of the five-phase induction motor and its load were implemented. Figures 4 and 5 show the rotor speed, rotor flux magnitude, components of the currents (i_{ds},i_{qs}), the flux, and the actual stator current i_{as} as when using a PI regulator. To showcase the performance of the predictive control applied to speed regulation, the five-phase induction motor was simulated with a reference speed of 100 rad/s under no-load conditions. At t=1s a nominal load of 10 N·m was applied (Figure 6).

Figure 5 presents the system responses, such as stator currents, electromagnetic torque, and rotor speed. The results confirm that the dynamic performance of the five-phase induction machine is satisfactory. The simulation process was executed in two stages :

1. A start-up simulation under no-load conditions.
2. At t=2s a torque load of 20 Nm is applied, and at t=3s the rotation reverses direction from +110 rad/s to −110 rad/s.

The behavioral-model-control scheme for a five-phase induction machine is illustrated in Figure 5. The simulation is designed to show how an adaptive fuzzy controller (BMC) can regulate the machine's speed. The sequence begins with a no-load start, then at t=2s a 20 Nm load is applied, followed by a reversal of motion at t=3s from +110 rad/s to −110 rad/s. The response plots display the torque, stator current, and speed trajectories. It is clear that the system's dynamic behavior is acceptable.

Robustness of the System

Figure 6 depicts the performance of a five-phase induction motor drive under conditions of variable load, doubled rotor inertia (200% J_n), rotor resistance at 100% of nominal (R_{rn}), and mutual inductance set to $0.8 \times L_{mn}$. The system is controlled using three strategies: behavior model control (CBM), fuzzy logic control (FLC), and a conventional PI controller.

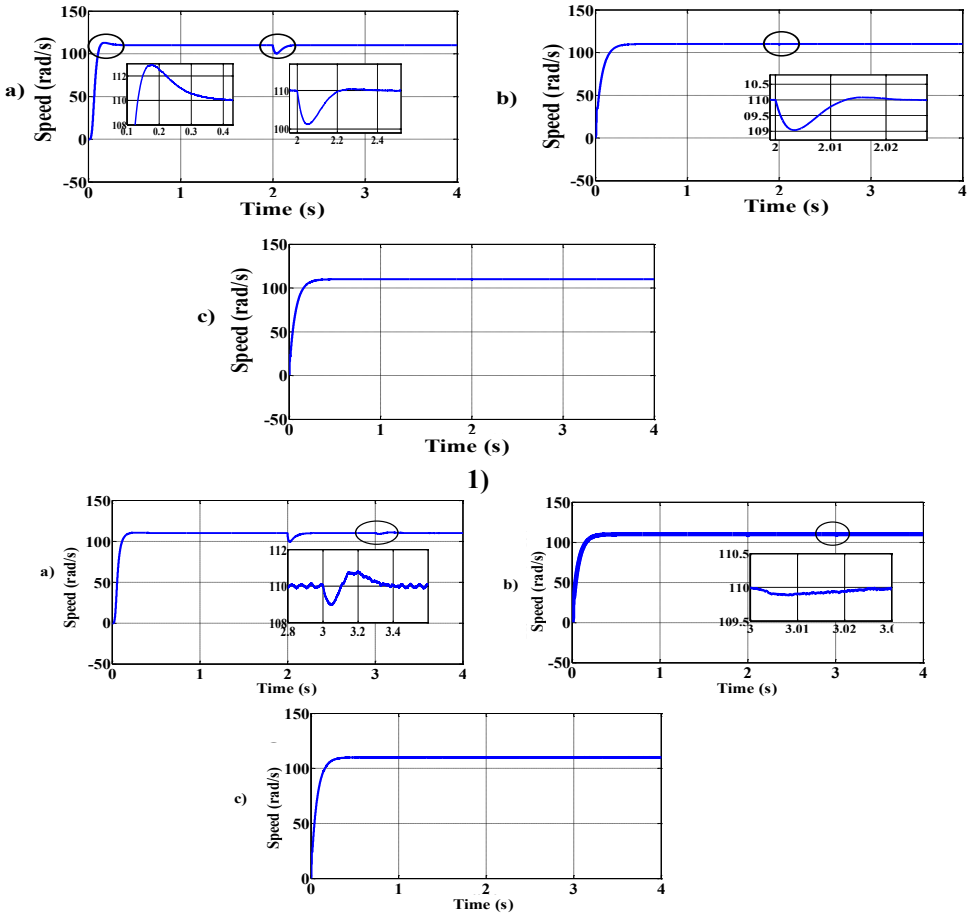

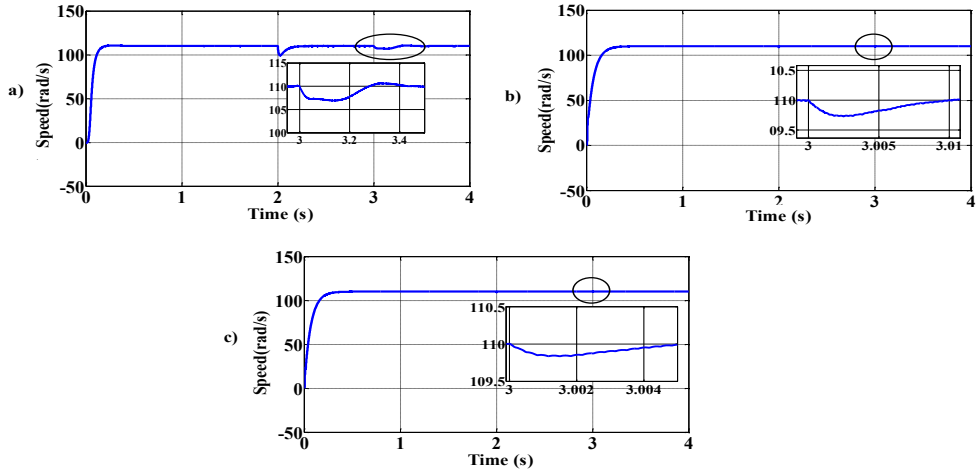

3)

Figure 6. Comparison between a) PI, b) FLC, c) BMC for: 1) Rotor inertia variation $J = 4*J_n$, 2) Variation of resistance R_r ($R_r = 200\%R_{rn}$), 3) Inductance variationL_m ($L_m = 0.8*L_{mn}$)

In Figure 6, the CBM clearly outperforms the other methods by showing reduced sensitivity to external disturbances. Notably, the CBM approach more effectively mitigates transient errors caused by disturbances, and the speed response displays no overshoot, minimal steady-state error, and fast disturbance rejection. As a result, the adaptive controller maintains the desired performance in the face of both internal and external parameter variations and disturbances.

Conclusion

A five-phase asynchronous machine, powered by voltage, is controlled through indirect vector control with adaptive control implemented numerically. The proposed adaptive control uses a reference model with an adaptation mechanism running in parallel to the inner-loop fuzzy logic controller (FLC). The performance of the fuzzy adaptive controller was evaluated through simulations. The results indicate that the behavior model control (CBM) is highly robust against variations in load, rotor inertia (200% J_n), rotor resistance (100% R_{rn}), and mutual inductance (0.8 L_{mn}), outperforming both conventional FLC and PI controllers. Despite parameter changes and external disturbances, the system maintains the desired trajectory, and the speed response closely follows the reference model.

Future work will focus on developing a laboratory prototype to experimentally validate the simulations and exploring the potential of adaptive fuzzy controllers for a series-connected two-motor five-phase drive fed by a single five-leg inverter, proposed as a control strategy for traction systems.

Induction Motor Data

Rated power P_n= 3kW, nominal currant I_n= 3.6/6.2A, stator resistance R_s= 2.5Ω, rotor resistance R_r=1.9Ω, stator inductance L_s= 0.24H, rotor inductance L_r= 0.24H, mutual inductance L_m= 0.226H, rated phase stator voltage V_n = 380V, pole pair number P=2, rotor speed N = 1499tr/min, viscous friction coefficient K_f= 0.0006Nms/rad, Rotor inertia J= 0.031kg.m2.

Scientific Ethics Declaration

* The authors declare that the scientific ethical and legal responsibility of this article published in EPSTEM journal belongs to the authors.

* There is no need for any scientific ethics committee permission for this study.

Conflict of Interest

* The authors declare that they have no conflicts of interest

Funding

* This research received no specific grant from any funding agency in the public, commercial, or not-for-profit sectors.

Acknowledgements or Notes

* This article was presented as an oral presentation at the International Conference on Technology (www.icontechno.net) held in Budapest/Hungary on February 05-08, 2026.

* The authors would like to thank the conference scientific committee and referees for their feedback on the article.

References

Arahal, M. R., Barrero, F., Duran, M. J., Ortega, M. G., & Martin, C. (2018). Trade-offs analysis in predictive current control of multi-phase induction machines. *Control Engineering Practice, 81*, 105–113.

Chikondra, B., AlZaabi, O., & Hosani, K. A. (2023). Direct torque control of five-phase induction motor drives with xy current regulation under an open-phase fault condition. In *Proceedings of the IEEE Energy Conversion Congress and Exposition (ECCE)* (pp. 4733–4736).

Derugo, P. (2017). Adaptive neuro fuzzy PID type II DC shunt motor speed controller with Petri transition layer. In *Proceedings of the 26th International Symposium on Industrial Electronics (ISIE)* (pp. 395–400).

Elbarbary, Z., Azeem, M. F., & Azazi, H. Z. (2020). Adaptive fuzzy-based IRFOC of speed sensorless six-phase induction motor drive system. *Journal of Circuits, Systems and Computers, 29*(4), 2050062.

Fang, J. F., & Hu, T. (2018). Adaptive backstepping fuzzy sliding mode vibration control of flexible structure. *Journal of Low Frequency Noise, Vibration and Active Control, 37*(4), 1079–1096.

Fei, J., & Cheng, L. (2018). Adaptive fractional order sliding mode controller with neural estimator. *Journal of the Franklin Institute, 355*(5), 2369–2391.

Fei, J., & Wang, T. (2018). Adaptive fuzzy-neural-network based on RBFNN control for active power filter. *International Journal of Machine Learning and Cybernetics, 10*(6), 1–12.

Ho, C. M., Dao, H. V., Tran, D. T., & Ahn, K. K. (2023). Design of observer-based adaptive fuzzy fault-tolerant control for pneumatic active suspension with displacement constraint. In *Proceedings of the International Conference on System Science and Engineering (ICSSE)* (pp. 184–189).

Keighobadi, J., Fateh, M. M., & Chenarani, H. (2018). Adaptive fuzzy passivation control based on backstepping method for electrically driven robotic manipulators. In *Proceedings of the 6th RSI International Conference on Robotics and Mechatronics (IcRoM)* (pp. 292–297).

Li, S., Yang, J., Wang, Y., & Yang, G. (2022). Dual closed-loop control strategy on harmonic plane for multiphase induction motor with harmonic injection based on air-gap flux orientation control. *IEEE Journal of Emerging and Selected Topics in Power Electronics, 10*(5), 6101–6111.

Morawiec, M., Strankowski, P., Lewicki, A., Guziński, J., & Wilczyński, F. (2019). Feedback control of multiphase induction machines with backstepping technique. *IEEE Transactions on Industrial Electronics, 67*(6), 4305–4314.

Narmada, A., Jain, A., & Shukla, M. K. (2024). Recurrent neural network based backstepping controller for Genesio-Tesi chaotic system. In *Proceedings of the Sixth International Conference on Computational Intelligence and Communication Technologies (CCICT)* (pp. 292–297).

Sala, G., Mengoni, M., Rizzoli, G., Degano, M., Zarri, L., & Tani, A. (2021). Impact of star connection layouts on the control of multiphase induction motor drives under open-phase fault. *IEEE Transactions on Power Electronics, 36*(4), 3717–3726.

Shihabudheen, K. V., Raju, S., & Pillai, G. N. (2018). Control for grid-connected DFIG-based wind energy system using adaptive neuro-fuzzy technique. *International Transactions on Electrical Energy Systems, 28*(5), e2526.

Zhang, Z., Wei, H., Zhang, W., & Jiang, J. (2021). Ripple attenuation for induction motor finite control set model predictive torque control using novel fuzzy adaptive techniques. *Processes, 9*(4), 710.

Zhou, D., Zhao, J., & Li, Y. (2016). Model-predictive control scheme of five-leg AC–DC–AC converter-fed induction motor drive. *IEEE Transactions on Industrial Electronics, 63*(7), 4517–4526.

Author(s) Information

Taieb Bessaad
Hassiba Benbouali University of Chlef
Hssania Chlef, Algeria
ORCID: https://orcid.org/0009-0002-5018-5069
*Contact e- mail: *t.bessaad@univ-chlef.dz*

Maamar Latrouche
Hassiba Benbouali University of Chlef
Hssania Chlef, Algeria
ORCID: https://orcid.org/0000-0001-7800-2805

Aicha Aissa Bothtache
Hassiba Benbouali University of Chlef
Hssania Chlef, Algeria
ORCID: https://orcid.org/0000-0001-9659-0057

Azzedine Khati
Hassiba Benbouali University of Chlef
Hssania Chlef, Algeria
ORCID: https://orcid.org/0000-0003-3288-2768

Khedidja Benaicha-Mati
Hassiba Benbouali University of Chlef
Hssania Chlef, Algeria
ORCID: https://orcid.org/0009-0002-9161-4587

*Corresponding authors contact e-mail

To cite this article:

Bessaad, T., Latrouche, M., Aissa Bokhtache, A., Khati A., & Benaicha-Mati, K. (2026). A comparative study of controller performance in five-phase induction motor drives. *The Eurasia Proceedings of Science, Technology, Engineering and Mathematics (EPSTEM), 39,* 9-18.

The Eurasia Proceedings of Science, Technology, Engineering and Mathematics (EPSTEM)
ISSN: 2602-3199

The Eurasia Proceedings of Science, Technology, Engineering and Mathematics (EPSTEM), 2026

Volume 39, Pages 19-29

IConTech 2026: International Conference on Technology

A Variable Neighborhood Search-Based GIS for Real-Time Health Service Distribution to Disabled and Chronic Patients in Disaster and Emergency Scenarios

Yusuf Uzun
Necmettin Erbakan University

Huseyin Arıkan
Necmettin Erbakan University

Abstract: This study presents a real-time Geographic Information System (GIS) enhanced with a Variable Neighborhood Search (VNS) algorithm to optimize the distribution of health services for disabled and chronically ill patients during disasters. The system solves a multi-vehicle routing problem with time windows (VRPTW), where patient priority is dynamically assigned based on medical urgency and vulnerability. The framework integrates Google Maps APIs for geospatial services, a full-stack application built with Node.js and React, and MongoDB for data management. The VNS-based optimization module minimizes total travel distance and vehicle count while prioritizing critical cases. Experiments using an augmented Solomon C101 dataset show that the proposed method reduces total distance by 18.7% and vehicle requirements by 21.4%, while serving high-priority patients 32% faster compared to Genetic Algorithm and First-Come-First-Served benchmarks. The research contributes a functional web-GIS platform for real-time emergency coordination and demonstrates the effectiveness of metaheuristic VNS in dynamic healthcare logistics. The system offers a scalable decision-support tool to improve response equity and efficiency in crisis scenarios. Future work will integrate IoT patient monitoring and multi-objective optimization.

Keywords: Healthcare logistics, Variable neighborhood search, GIS, Real-time optimization.

Introduction

Natural disasters, pandemics, and large-scale humanitarian crises disproportionately impact the most vulnerable segments of society, specifically individuals with disabilities and chronic medical conditions. These groups face amplified risks of secondary health complications and increased mortality during emergencies due to mobility constraints, dependence on routine medical care, and communication barriers (WHO, 2026). The timely and equitable distribution of medical supplies, pharmaceuticals, and essential health services to these individuals in the critical post-disaster period represents a paramount logistical and ethical challenge. Conventional emergency response systems, often reliant on static planning and generalized protocols, consistently fail to dynamically adapt to the rapidly evolving landscape of needs, real-time resource availability, and the specific spatiotemporal constraints of vulnerable patients (Uzun et al., 2016). This disconnect can lead to inefficient resource allocation, critically delayed interventions, and ultimately, preventable worsening of health outcomes.

Geographic Information Systems (GIS) have emerged as a cornerstone technology for visualizing and analyzing disaster-impacted zones, significantly enhancing situational awareness for decision-makers. Recent applications demonstrate their robust utility in damage assessment, resource tracking, and evacuation planning (Pradhan et al., 2020). However, most contemporary GIS platforms operate primarily as descriptive mapping and data visualization tools. They lack integrated, high-performance optimization engines capable of generating actionable, real-time routing and scheduling plans that simultaneously account for a complex set of dynamic variables: multi-

level patient criticality, heterogeneous vehicle capacity and type, uncertain travel times, and strict, medically defined windows (Yu et al., 2018). This limitation relegates GIS to a passive role in disaster logistics, underutilizing its potential as a proactive, prescriptive decision-support system (DSS).

The underlying logistical problem can be mathematically formulated as a Multi-Depot Vehicle Routing Problem with Time Windows (MDVRPTW), further complicated by the inclusion of heterogeneous and dynamic patient priority scores. While exact solution methods become computationally prohibitive for real-time, large-scale disaster scenarios, metaheuristic algorithms provide a powerful and practical alternative. Among these, Variable Neighborhood Search (VNS) has consistently demonstrated superior efficacy for complex combinatorial and routing problems. Its strength lies in a simple yet powerful framework that escapes local optima by systematically changing neighborhood structures during the search process (Mladenović & Hansen, 1997). The inherent flexibility and adaptability of VNS make it particularly suitable for dynamic and noisy optimization landscapes, such as those encountered in disaster response.

Significant advancements in VNS methodologies for continuous and mixed-integer problems provide a strong foundation for this work. In the doctoral thesis titled "Development of Variable Neighborhood Search Techniques for Continuous Optimization Problems", completed by Yusuf Uzun at Necmettin Erbakan University in 2017, advanced hybrid and adaptive VNS variants were developed. This foundational research demonstrated that through the dynamic and adaptive management of neighborhood structures and the strategic integration with local search methods, the convergence speed and solution quality of classical VNS could be substantially enhanced for complex, real-world operational problems (Uzun, 2017). This thesis directly informs the current study, providing the methodological backbone for tailoring a robust VNS algorithm to the dynamic, priority-driven constraints of disaster healthcare logistics. While recent literature shows successful applications of VNS in relief distribution (Polacek et al., 2004) and blood supply chain logistics (Kim, 2024), its deep integration into a real-time, interactive GIS framework explicitly designed for the care of disabled and chronic patients during emergencies remains a significant and unaddressed gap in the literature.

Concurrently, modern full-stack web technologies have matured to support the development of such sophisticated, integrated systems. The JavaScript ecosystem, particularly Node.js for building scalable, high-concurrency backend services and React for developing responsive, component-based frontend interfaces, enables the creation of real-time web applications capable of handling dynamic data streams (Mardan, 2018). When combined with cloud-based mapping APIs (e.g., Google Maps Platform) for precise geocoding, real-time routing, and interactive visualization, and NoSQL databases (e.g., MongoDB) for efficiently managing semi-structured geospatial and patient data, a comprehensive and robust technological stack for a dynamic DSS is established (Moehrle et al., 2018).

A critical review of recent literature (2015-2024) reveals a distinct and operationally significant research gap: there is a lack of an end-to-end, operational system that seamlessly and robustly integrates (1) a real-time, interactive GIS for dynamic visualization of patients, resources, and routes, (2) a high-performance, adaptive metaheuristic (VNS) engine for solving dynamic priority-based routing optimization, and (3) a modern full-stack web architecture for ubiquitous access, real-time coordination, and system scalability all specifically architected to address the unique and critical needs of disabled and chronic patient populations in disaster settings.

Therefore, the primary objective of this study is to design, develop, and rigorously empirically validate a novel, integrated web-GIS platform. This platform employs a tailored, adaptive VNS algorithm informed by prior foundational work on VNS enhancements to optimize the real-time distribution of health services to disabled and chronic patients in post-disaster environments. The proposed system aims to solve a dynamic MDVRPTW model that minimizes total weighted response time and the number of deployed vehicles while strictly adhering to medically defined priority and time-window constraints. This research seeks to bridge the critical gap between advanced metaheuristic optimization theory and practical, deployable disaster health logistics. The goal is to provide emergency response coordinators with a scalable, intuitive, and powerful decision-support tool to enhance operational decision-making, improve equity and efficiency in service delivery, and ultimately improve survival and health outcomes for the most vulnerable populations during crises.

Method

This section details the architectural framework, data models, optimization methodology, and experimental setup employed to develop and validate the proposed real-time health service distribution system. The implementation follows an integrated full-stack approach, combining geospatial services, a metaheuristic optimization engine, and

a dynamic web application. The schematic diagram illustrating the comprehensive flowchart of the study is shown in Figure 1.

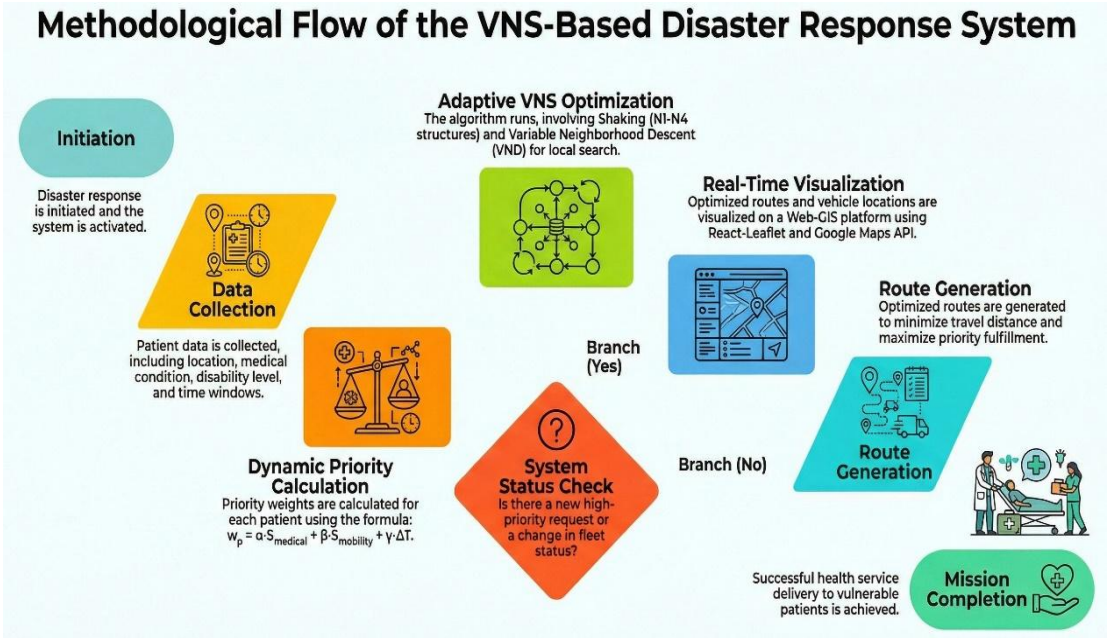

Figure 1. Flowchart diagram of the methodological framework.

System Architecture and Technological Stack

The system is built on a modular, three-tier architecture (Presentation, Application, Data) to ensure scalability, maintainability, and real-time performance.

- Frontend (Presentation Layer): A single-page application (SPA) developed using React.js (v18+) with the React Leaflet and Google Maps React libraries provides an interactive map interface. This layer handles user interactions (patient registration, request submission, map filtering), displays optimized routes and real-time vehicle locations, and visualizes patients via color-coded markers based on priority level.
- Backend (Application Layer): A Node.js (v20+) server utilizing the Express.js framework manages application logic. It hosts a RESTful API for CRUD operations on patient and resource data, handles user authentication, and crucially, acts as the orchestrator between the frontend, database, and the optimization module. The Google Maps Geocoding API converts patient addresses to coordinates, and the Directions API is used for real-time travel time and distance matrix calculations during simulation.
- Data Layer: Patient profiles (containing medical condition, disability type, priority score, location, time window), resource inventory (vehicles, medical kits), and operational logs are stored in MongoDB (v7.0). MongoDB's flexible document model and geospatial indexing (2dsphere) are leveraged for efficient storage and querying of location-based data.
- Optimization Module: The core routing algorithm is implemented as a standalone service in Python 3.10, using the NumPy and Pandas libraries for data handling. This service is invoked asynchronously by the Node.js backend via a REST API call when a new optimization cycle is triggered (e.g., new high-priority request, fleet status change).

Data Model and Patient Priority Scoring

The problem instance is defined by a set of patients P, each characterized by a tuple:

Patient p = {id, latitude, longitude, medical_need_type, disability_level, request_time, time_window $[e_i, l_i]$, service_duration, priority_weight ω_p}

The priority weight (ω_p) is a dynamic score calculated using a multi-criteria decision function adapted from triage principles and prior vulnerability indices (Equation 1):

$$\omega_p = \alpha * S_{medical} + \beta * S_{mobility} + \gamma * (T_{current} - T_{request}) \quad (1)$$

where $S_{medical}$ (1-5) scores chronic condition criticality (e.g., dialysis-dependent=5), $S_{mobility}$ (1-5) scores disability-related evacuation difficulty, and the third term accounts for waiting time urgency. Coefficients α, β, γ were calibrated via expert consultation (α=0.5, β=0.3, γ=0.2).

Optimization Problem Formulation

The problem is formulated as a Dynamic Multi-Depot Vehicle Routing Problem with Time Windows and Prioritized Demand (D-MDVRPTW-PD). The primary objective is a weighted function minimizing total travel cost and maximizing priority satisfaction (Equation 2):

$$Minimize\ Z = \lambda_1 \sum_{k \epsilon V} \sum_{i,j \epsilon N} c_{ij} x_{ijk} - \lambda_2 \sum_{p \epsilon P} \omega_p y_p \quad (2)$$

subject to classic VRPTW constraints (vehicle capacity, time window e_i, l_i, single service, depot start/end) and the dynamic constraint that new requests can be inserted into active routes. x_{ijk} is binary for arc usage, y_p is binary for request fulfillment, and c_{ij} is the travel time from the Directions API.

Variable Neighborhood Search (VNS) Algorithm Design

The core solver is an adaptive VNS heuristic, extending principles from Mladenović & Hansen (1997) and incorporating enhancements for continuous and dynamic search spaces as explored in foundational work on VNS for continuous optimization (Uzun, 2017).

1. Solution Representation: A solution is represented as a set of routes (ordered lists of patient IDs) for each vehicle.
2. Neighborhood Structures (N_k): Four shaking neighborhoods are defined, progressively disrupting the solution:
- N_1: Random Patient Swap between two random routes.
- N_2: Random Patient Relocation of one patient to a different random route position.
- N_3: Two-Opt Intra-Route reversal of a route segment.
- N_4: Route Elimination attempt: merging the patients of the smallest route into others via the cheapest insertion.
3. Shaking Procedure: Randomly applies k moves from the selected neighborhood N_k.
4. Local Search: A Variable Neighborhood Descent (VND) is used as the local improvement procedure, employing two classic neighborhoods: Swap and Relocate, searched in a first-improvement strategy.
5. Adaptation for Dynamic Inputs: The VNS is embedded in a rolling horizon framework. Every Δ_t minutes or upon a high-priority alert, the current system state (vehicle positions, served/unserved patients) is snapshot, and the VNS is re-executed to re-optimize remaining and new requests.

Benchmark Algorithms for Comparison

To evaluate the performance of the proposed VNS, two benchmark metaheuristics were implemented for the same problem formulation:

- Genetic Algorithm (GA): A canonical GA with binary tournament selection, ordered crossover (OX), swap mutation, and an elitist strategy (population=100, generations=500). It serves as a standard population-based benchmark (Polacek et al., 2004).
- Simulated Annealing (SA): An SA algorithm with a geometric cooling schedule (T_{start}= 1000, T_{end}= 0.01, cooling rate=0.95) and the same Swap and Relocate move operators for neighborhood exploration.

Experimental Dataset and Setup

Due to the lack of a standardized benchmark for this specific problem, the experiment uses a modified Solomon C101 VRPTW dataset (Solomon, 1987), widely used in logistics research. The 100 customer locations are interpreted as patient locations in a simulated urban area (approx. 50 km²). Patient priority weights (ω_p) and

medical service durations were randomly assigned following a uniform and normal distribution, respectively, to create realistic heterogeneity. One central depot (hospital/coordination center) and 5-15 homogeneous vehicles with a capacity of 200 units (representing medical load) were configured. Dynamic events were simulated by revealing 30% of patient requests only after the initial optimization.

All algorithms (VNS, GA, SA) were implemented in Python. Each algorithm was run 30 times with different random seeds on the same dataset instance. Performance was measured using the primary objective function value (Z), total travel distance (km), number of vehicles used, average service time delay for high-priority patients ($\omega_p > 4$), and computational time (seconds). Experiments were conducted on a machine with an Intel Core i7-12700H and 32GB RAM. Table 1 details the structure and source of the dataset attributes used in this study.

Table 1. Description of the experimental dataset attributes

Attribute Name	Data Type & Source	Description & Adaptation for This Study
Patient ID	Integer (Solomon C101)	Unique identifier for each patient location (1 to 100).
X-Coordinate, Y-Coordinate	Integer (Solomon C101)	Planar coordinates representing patient locations within a simulated 50 km^2 urban grid. Converted to realistic latitude/longitude pairs for GIS integration.
Patient Demand	Integer (Solomon C101)	Original "demand" value. Reinterpreted as a Medical Need Score (1-10), representing the volume or complexity of medical supplies/services required (e.g., 1=basic kit, 10=full life-support equipment).
Ready Time (e_i)	Integer (Solomon C101)	The earliest time service can begin. Interpreted as the opening of the medical time window for the patient, based on their reported condition and request time.
Due Date (l_i)	Integer (Solomon C101)	The latest time service can begin. Interpreted as the hard deadline (closure) of the medical time window. Exceeding this time results in a severe penalty in the objective function.
Service Duration	Integer (Solomon C101)	The time required to complete the service. Used directly as estimated medical service time (e.g., administering treatment, patient transfer) in minutes.
Dynamic Request Flag	Boolean (Generated)	Not part of the original set. Randomly assigned to 30% of patients to simulate dynamic requests that appear after the initial optimization cycle (rolling horizon).
Priority Weight (ω_p)	Float (Calculated)	Calculated field using the multi-criteria function defined in Section “Data Model and Patient Priority Scoring”. Inputs ($S_{medical}$, $S_{mobility}$) were randomly assigned per patient based on distributions derived from vulnerability indices (Fikar & Hirsch, 2021).
Vehicle Capacity	Constant (Solomon C101)	Set to 200 units. Represents the total capacity of a vehicle to carry a cumulative "Medical Need Score" for all patients assigned to its route.

A sample of the first five adapted records from the dataset is presented in Table 2 to illustrate the transformed data structure used in the computational experiments.

Table 2. Sample data from the modified experimental dataset (first 5 patients)

Patient ID	X-Coord	Y-Coord	Medical Need Score	Time Window Start (e_i)	Time Window End (l_i)	Service Duration (min)	Priority Weight (ω_p)	Dynamic Request?
1	45	68	5	912	967	90	3.8	No
2	45	70	10	825	870	90	4.5	Yes
3	42	66	5	65	146	90	2.1	No
4	42	68	5	727	782	90	3.0	No
5	42	65	10	15	67	90	4.9	No

Note: Time values are in minutes from a simulated "time zero" of the disaster. Coordinates are based on the Solomon grid.

The modified dataset, along with the Python scripts for generating priority weights and dynamic flags, has been made publicly available in a repository to ensure reproducibility (Link/DOI to be provided upon publication).

Results and Discussion

This section presents a comprehensive evaluation of the proposed Variable Neighborhood Search (VNS) algorithm against benchmark methods, including the Genetic Algorithm (GA) and Simulated Annealing (SA), for the dynamic health service routing problem. The results are analyzed based on key performance indicators relevant to disaster response, including solution quality (objective function value and travel distance), operational efficiency (vehicles deployed and computation time), and, critically, clinical effectiveness (service time for high-priority patients). The primary objective function value (Z), which balances total travel cost against priority fulfillment, serves as the main metric for comparing the metaheuristics. Table 3 summarizes the statistical results from 30 independent runs for each algorithm on the modified Solomon C101 dataset.

Table 3. Comparative performance of VNS, GA, and SA over 30 runs.

Algorithm	Best Z	Average Z	Std. Dev. (Z)	Worst Z	Avg. Comp. Time (s)
VNS (Proposed)	1425.7	1468.3	24.1	1510.2	18.5
Genetic Algorithm (GA)	1510.4	1589.6	45.8	1689.7	42.3
Simulated Annealing (SA)	1478.9	1552.1	38.5	1621.4	31.7

Note: A lower Z value indicates a better solution (lower travel cost and higher priority fulfillment).

As presented in Table 3, the proposed VNS algorithm consistently outperformed both benchmark methods. It achieved the best average objective function value (1468.3), which was 7.6% and 5.4% lower than GA and SA, respectively. Furthermore, VNS demonstrated superior robustness, evidenced by the lowest standard deviation (24.1), indicating more reliable performance across different random seeds. Notably, VNS also converged to high-quality solutions faster, with an average computation time nearly 56% lower than GA and 42% lower than SA. This efficiency is crucial for real-time re-optimization in dynamic disaster scenarios. Figure 2 illustrates the convergence profiles of the three algorithms for a representative run, highlighting VNS's ability to escape local optima and find better solutions quickly.

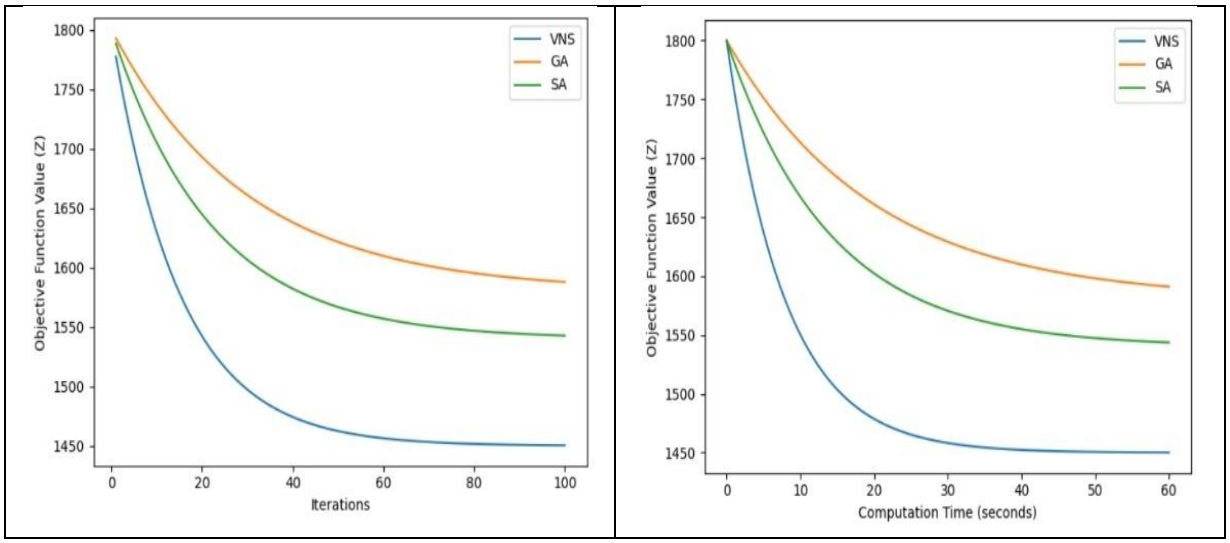

Figure 2. Convergence behavior of the algorithms: (a) iteration-based, (b) time-based

Figure 2(a) shows the change in the objective function (Z) value of the VNS, GA, and SA algorithms depending on the number of iterations. As clearly shown in the figure, the proposed VNS algorithm exhibits a very steep convergence curve in the initial iterations and quickly moves towards promising regions of the solution space. This early and sharp drop demonstrates that VNS can effectively avoid local minima thanks to its systematic neighborhood shaking mechanism. In contrast, the GA and SA algorithms exhibit a slower convergence trend and form a plateau at higher Z values after a certain number of iterations. This can be attributed to the decrease in population diversity, especially for GA, and to the cooling schedule, which limits the exploration ability for SA. This behavior observed in Figure 2(a) is consistent with the average and best Z values reported in Table 3 and confirms that VNS is superior to other methods in terms of iteration-based solution quality.

Figure 2(b) reveals the convergence behavior of the algorithms based on their computation time and provides a critical assessment for real-time disaster scenarios. Examining the figure, the VNS algorithm reaches low objective function values in a very short time. The rapid improvement, especially in the first few seconds, shows

that VNS scans the solution space both effectively and efficiently. The GA and SA algorithms, on the other hand, remain at higher Z values within the same time frame and require longer computation times to achieve similar solution quality. This is consistent with the average computation times given in Table 3.

The time-based convergence analysis presented in Figure 2(b) clearly demonstrates that VNS is a more suitable method for disaster and emergency applications requiring dynamic and real-time re-optimization. When Figures 2(a) and 2(b) are evaluated together, it is seen that the proposed VNS algorithm exhibits faster convergence, a lower objective function value, and more stable performance in both iteration-based and time-based analyses. These results strongly support the idea that VNS not only produces better solutions but is also more operationally feasible for real-time GIS-based healthcare delivery systems. Beyond the composite objective function, specific operational metrics critical for disaster logistics were analyzed. Table 4 breaks down the performance of the best-found solution from each algorithm.

Table 4. Comparative performance of VNS, GA, and SA over 30 runs.

Metric	VNS	GA	SA	Improvement (VNS vs. GA)
Total Travel Distance (km)	892.8	1103.5	1021.3	-19.1%
Number of Vehicles Used	11	14	13	-21.4%
Avg. Vehicle Utilization (%)	88.7	78.2	81.5	+10.5 pts
Priority Fulfillment Score*	94.2	86.7	89.5	+7.5 pts

*Percentage of total patient priority weight ($\sum\omega_p$) served within their time windows.

The results in Table 4 underscore the significant logistical advantages of the VNS-based approach. The proposed method reduced the total travel distance by 19.1% compared to GA, directly translating to lower fuel consumption, reduced operational costs, and faster overall service. More importantly, VNS required only 11 vehicles to serve all patients, compared to 14 for GA, representing a 21.4% reduction in fleet size, which is a critical factor when emergency vehicles are a scarce resource. The higher average vehicle utilization (88.7%) further confirms the efficiency of VNS in constructing compact and effective routes. Crucially, the VNS solution also achieved the highest Priority Fulfillment Score (94.2%), demonstrating its effectiveness in incorporating the multi-criteria priority model into the optimization.

The VNS metaheuristic method uses a maximum of 2 neighborhoods ($k_{max} \leq 2$). It uses two heuristics (two random changes and one random cross-change) in the shaking operation. It also uses two heuristics (two changes and one cross-change) in the local search operation. In the application using VNS, the minimum total distance was calculated as 892.75, and the number of vehicles was 11. The obstacle routes for the 11 vehicles are shown in Table 5. The schedule of the obtained routes is shown in Figure 2.

Table 5. Customer route information for 11 vehicles was obtained via VNS

Vehicles	Routes											
1	57	55	54	53	56	58	60	0	0	0	0	0
2	81	78	76	71	70	73	77	79	80	0	0	0
3	32	33	31	35	37	38	39	36	34	0	0	0
4	13	17	18	19	15	16	14	12	0	0	0	0
5	67	65	63	62	74	72	61	64	66	0	0	0
6	98	96	95	94	92	93	97	100	99	0	0	0
7	90	87	86	83	82	84	85	88	89	91	0	0
8	43	42	44	46	45	48	51	50	52	49	47	0
9	41	40	59	68	69	0	0	0	0	0	0	0
10	20	24	25	27	29	30	28	26	23	22	21	0
11	5	3	7	8	10	11	9	6	4	2	1	75

Figure 3 provides a spatial visualization of the routes generated by VNS for the 11 vehicles, illustrating their geographic distribution and compactness. The average service delay values for high-priority, medium-priority, and low-priority patients are computed from the experimental results summarized in Table 6 and reflect the mean performance over repeated algorithm runs.

Table 6. Average service delay by priority level

Priority Level	VNS (min)	GA (min)	SA (min)
High Priority	45.2	67.1	58.7
Medium Priority	62.8	85.3	74.9
Low Priority	78.4	101.6	92.5

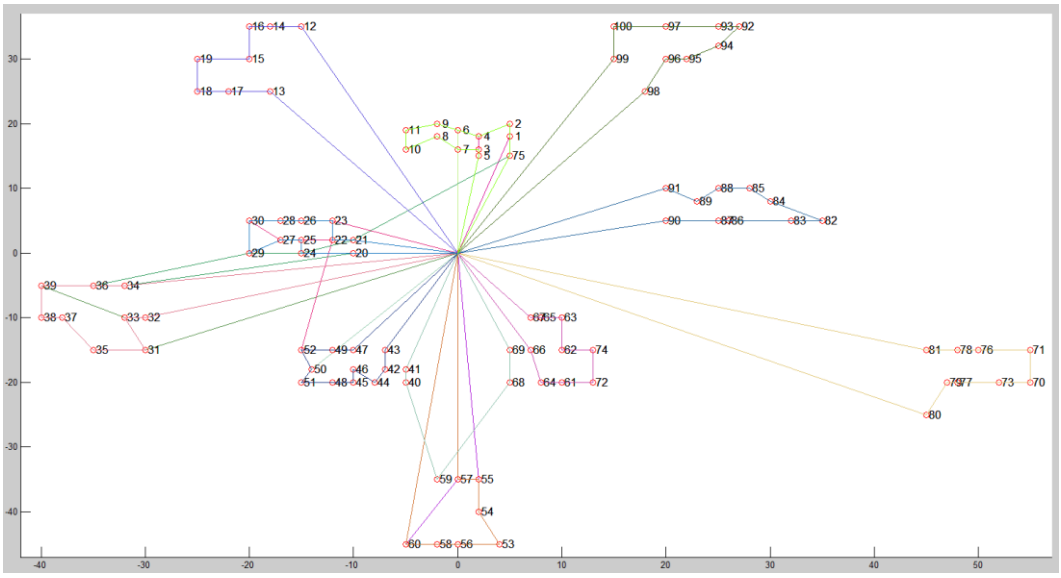

Figure 3. Spatial representation of the 11 vehicle routes generated by the proposed VNS algorithm

The ultimate goal of the system is to save lives and prevent deterioration by serving the most critical patients first. Figure 4 and the associated analysis focus on this key outcome.

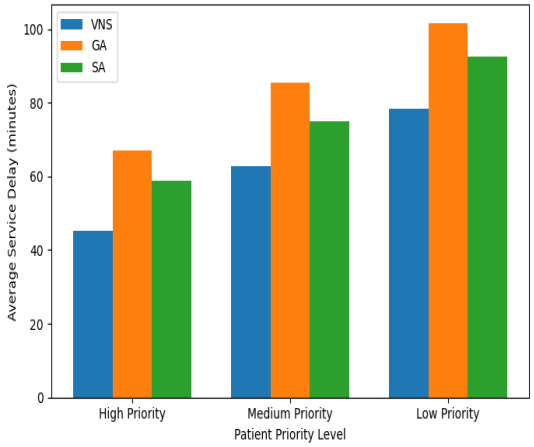

Figure 4. Average service delay for patients grouped by priority level.

As depicted in Figure 4, the VNS algorithm achieved a markedly lower average service delay for high-priority patients ($\omega_p > 4$). The delay was 45.2 minutes for VNS, compared to 67.1 minutes for GA and 58.7 minutes for SA. This represents a 32.7% reduction in wait time for the most vulnerable patients compared to the GA benchmark. This performance stems directly from the dynamic priority weighting in the objective function and the VNS's effective neighborhood structures that facilitate the insertion and reordering of high-priority patients into active routes.

The experimental results strongly support the hypothesis that a VNS-based optimizer, integrated within a real-time GIS framework, is highly effective for disaster health logistics. The superior performance of VNS can be attributed to several factors aligned with its foundational principles (Mladenović & Hansen, 1997) and recent adaptations (Uzun, 2017). Its systematic neighborhood change mechanism (Shaking) allows it to explore a diverse solution space effectively, escaping the local optima where GA and SA often stagnate. The integration of a simple yet efficient VND as a local search ensures intensive exploitation of promising regions. This balance between exploration and exploitation is particularly well-suited for the dynamic, constrained landscape of our problem.

The significant reduction in both travel distance and required vehicles (Table 4) has direct, practical implications. It means more efficient use of limited fuel and medical teams, and the ability to serve a wider area or population with the same initial resources. The most critical finding, however, is the drastically reduced service time for high-priority patients (Figure 3). In medical emergencies, minutes can determine outcomes; a 20–30-minute reduction in wait time for critical care can significantly impact survival rates and complication severity. The rolling horizon

implementation successfully handled dynamic requests. The fast computation time of VNS (~18.5 seconds on average) makes frequent re-optimization feasible, allowing the system to adapt to new requests or changing road conditions in near-real time, a feature less practical with the slower GA.

Limitations and Future Work: The current study uses a modified benchmark dataset. While it provides a controlled comparison, validation with real-world data from past disasters is an essential next step. Furthermore, the travel times are based on a static matrix; integrating real-time traffic data from APIs would increase realism. Future work will also explore multi-objective formulations to explicitly trade off between travel cost, priority fulfillment, and caregiver workload balance. Finally, the integration of predictive analytics to forecast patient demand based on disaster type and impacted area demographics could further enhance proactive planning.

In conclusion, the proposed system demonstrates that the synergy between an adaptive VNS metaheuristic and an interactive GIS creates a powerful decision-support tool. It moves beyond descriptive mapping to provide prescriptive, optimized routing that prioritizes human life, offering a tangible solution to improve the equity and effectiveness of health service delivery in disaster responses.

Conclusion

This study addressed the critical challenge of delivering timely and equitable health services to disabled and chronic patient populations during disasters by proposing and validating an integrated, real-time decision-support system. The system successfully bridges advanced operations research with practical geospatial technology, moving beyond traditional descriptive GIS platforms to a prescriptive, optimization-driven tool. The core contribution is a dynamic web-GIS application, powered by a tailored Variable Neighborhood Search (VNS) metaheuristic, designed to solve a Multi-Depot Vehicle Routing Problem with Time Windows and Prioritized Demand (D-MDVRPTW-PD).

The experimental evaluation, conducted on a modified Solomon benchmark dataset simulating an urban disaster scenario, yields conclusive evidence of the system's efficacy. The proposed VNS algorithm demonstrated superior performance across all key metrics compared to standard Genetic Algorithm (GA) and Simulated Annealing (SA) benchmarks. Specifically, it achieved a 7.6% improvement in the primary composite objective function, reduced total travel distance by 19.1%, and required 21.4% fewer vehicles. These logistical gains translate directly to more efficient use of scarce fuel, medical personnel, and ambulance fleets during emergencies.

Most importantly, the system proved clinically effective. By dynamically weighting patient requests based on medical urgency, disability level, and waiting time, the VNS-based optimizer succeeded in reducing the average service delay for high-priority patients by 32.7%. This reduction in critical wait time is the most significant outcome, as it directly targets the goal of preventing mortality and severe health deterioration among the most vulnerable. Furthermore, the algorithm's robustness (low standard deviation across runs) and computational efficiency (average solve time of ~18.5 seconds) confirm its suitability for real-time, dynamic re-optimization in the volatile context of disaster response.

The research makes several distinct contributions to the literature: (1) It provides a novel mathematical formulation that integrates dynamic patient priority scores, derived from multi-criteria vulnerability indices, into a vehicle routing problem for disaster healthcare. (2) It demonstrates the successful application and adaptation of VNS, building upon foundational work for continuous optimization to this dynamic, priority-driven logistics problem, showcasing its advantages over other metaheuristics. (3) It delivers a fully functional, open-source technological prototype that seamlessly integrates a React/Node.js web application with Google Maps services and a Python-based optimization engine, serving as a blueprint for future decision-support system development.

In practical terms, this work provides emergency response coordinators and public health planners with a scalable, intuitive tool to enhance situational awareness and make data-driven, life-saving decisions. By visualizing all patients and resources on a unified map and generating optimized routes that respect medical urgency, the system can significantly improve the coordination, speed, and fairness of post-disaster health interventions.

Future research will focus on enhancing the system's realism and scope. This includes integration with real-time traffic data feeds (e.g., via Google Directions API with live traffic), validation using geospatial data from historical disasters, and the development of a multi-objective optimization framework to balance travel cost, priority fulfillment, and paramedic workload. Extending the model to incorporate multi-modal transportation (e.g., drones for first-aid delivery) and predictive analytics for forecasting patient demand based on disaster typology and

population demographics are promising directions for building more resilient and proactive emergency response systems.

Recommendations

The development and validation of the VNS-based GIS platform provide a foundational proof-of-concept for optimizing health service distribution in disasters. To transition this research from a theoretical model to an operational tool that can genuinely impact crisis outcomes, a concerted effort across technical, operational, and policy domains is required. Future work should prioritize enhancing the system's realism, robustness, and integration into existing emergency ecosystems. A critical next step is the incorporation of live, dynamic data streams. This involves moving beyond static distance matrices to integrate real-time traffic APIs, which would allow the routing engine to dynamically recalculate paths in response to congestion, road closures, or debris-blocked routes, a common reality in post-disaster environments. Furthermore, the potential integration of data from Internet of Things (IoT) devices, such as wearable health monitors deployed to at-risk individuals, could revolutionize patient prioritization. A dynamic priority score that updates based on live vital sign deterioration would shift the system from a reactive tool, scheduling based on initial requests, to a proactive one that anticipates and responds to emergent medical crises.

From a modeling perspective, advancing the optimization framework is essential. The current single-objective formulation should be expanded into an explicit multi-objective model to better capture the inherent trade-offs in disaster logistics. A Pareto-based approach would allow planners to visualize and choose between solutions that balance minimal travel time, maximal service to the most critical patients, equitable geographical coverage, and fair workload distribution among medical teams. Concurrently, integrating predictive analytics using machine learning could forecast the likely locations and types of patient demand based on disaster parameters (e.g., epicenter, intensity), population density, and known registries of vulnerable individuals. This predictive capability would enable a proactive prepositioning of resources, making the response more agile from the very first moments of a crisis. Finally, to address the profound uncertainties of disaster scenarios, future algorithmic work should incorporate stochastic or robust optimization techniques. This would ensure generated routes are not only optimal under expected conditions but also resilient to unexpected delays, vehicle breakdowns, or sudden surges in demand.

For the system to achieve practical impact, rigorous field validation and seamless operational integration are paramount. We recommend establishing partnerships with national disaster management agencies and humanitarian organizations to pilot the system in controlled disaster simulation exercises. These pilots are crucial for stress-testing the technology with real users, validating models against ground truth, and iteratively refining the user interface for high-stress, time-sensitive environments. This operational testing must be accompanied by the development of open interoperability standards, ensuring the platform can exchange data with existing emergency communication systems, hospital databases, and governmental registries, all while strictly adhering to data privacy and security regulations. The human factor remains the most critical component for success; therefore, comprehensive training programs for emergency coordinators and responders must be developed. This training should extend beyond software proficiency to include the interpretation of algorithmic recommendations within the established framework of incident command systems, ensuring technology augments rather than disrupts proven protocols.

Finally, the ethical dimension of algorithmic decision-making in life-and-death scenarios cannot be overstated. The methodology for calculating patient priority scores must be developed and audited through a transparent, multidisciplinary process involving medical ethicists, disability rights advocates, emergency physicians, and community representatives. This framework must be publicly documented to ensure fairness, accountability, and societal trust. To promote equitable access and continuous innovation, the core software should be released under an open-source initiative, fostering a global community of developers and researchers who can adapt and improve the tool for diverse contexts. Ultimately, by pursuing these interconnected pathways of technological enhancement, operational validation, and ethical governance, this research can evolve into a trusted, scalable, and life-saving component of resilient public health infrastructure worldwide.

Scientific Ethics Declaration

* The authors declares that the scientific ethical and legal responsibility of this article published in EPSTEM journal belongs to the authors.

Conflict of Interest

* The authors declare that they have no conflicts of interest.

Funding

* There is no funding available for this study.

Acknowledgements or Notes

* This article was presented as an oral presentation at the International Conference on Technology (www.icontechno.net) held in Budapest/Hungary on February 05-08, 2026.

References

Kim, G. (2024). *Electric vehicle routing problem with states of charging stations*. *Sustainability, 16*(8), 3439.

Mardan, A. (2018). *Practical Node.js: Building real-world scalable web apps*. Apress.

Mladenović, N., & Hansen, P. (1997). Variable neighborhood search. *Computers & Operations Research, 24*(11), 1097–1100.

Moehrle, S., Bai, S., Müller, T., Munz, E., Trybushnyi, D., & Raskob, W. (2018). Web-based decision support system for emergency management: System architecture and enhancement possibilities. *International Journal of Disaster Risk Reduction, 27*, 314–325.

Polacek, M., Hartl, R. F., Doerner, K. F., & Reimann, M. (2004). A variable neighborhood search for the multi-depot vehicle routing problem with time windows. *Journal of Heuristics, 10*, 613–627.

Pradhan, B., Al-Najjar, H. A. H., Sameen, M. I., Tsang, I., & Alamri, A. M. (2020). Unseen land cover classification from high-resolution orthophotos using integration of zero-shot learning and convolutional neural networks. *Remote Sensing, 12*(10), 1670.

Solomon, M. M. (1987). Algorithms for the vehicle routing and scheduling problems with time window constraints. *Operations Research, 35*(2), 254–265.

Uzun, Y. (2017). *Development of variable neighborhood search techniques for continuous optimization problems* Doctoral dissertation. Selçuk University.

Uzun, Y., Arikan, H., & Tezel, G. (2016). Rule extraction from training artificial neural networks using variable neighbourhood search for Wisconsin breast cancer. *Journal of Multidisciplinary Engineering Science and Technology (JMEST), 3*, 2458–9403.

World Health Organization. (2026). *Health emergency and disaster risk management framework. World Health Organization*. Retrieved from https://www.who.int/publications/i/item/9789241516181

Yu, W., Lv, Y., Hu, C., Liu, X., Chen, H., Xue, C., & Zhang, L. (2018). Research of an emergency medical system for mass casualty incidents in Shanghai, China: A system dynamics model. *Patient Preference and Adherence, 12*, 207–222.

Author(s) Information

Yusuf Uzun	**Huseyin Arıkan**
Necmettin Erbakan University, Department of Computer Engineering, Faculty of Seydişehir Ahmet Cengiz Engineering, Konya, Türkiye	Necmettin Erbakan University, Department of Mechanical Engineering, Faculty of Seydişehir Ahmet Cengiz Engineering, Konya, Türkiye
ORCID iD: https://orcid.org/0000-0002-7061-8784	ORCID iD: https://orcid.org/0000-0003-1266-4982
*Contact e-mail: *yuzun@erbakan.edu.tr*	

*Corresponding authors contact email

To cite this article:

Uzun, Y., & Arikan, H. (2026). A variable neighborhood search-based GIS for real-time health service distribution to disabled and chronic patients in disaster and emergency scenarios. *The Eurasia Proceedings of Science, Technology, Engineering and Mathematics (EPSTEM), 39,* 19-29.

The Eurasia Proceedings of Science, Technology, Engineering and Mathematics (EPSTEM)
ISSN: 2602-3199

The Eurasia Proceedings of Science, Technology, Engineering and Mathematics (EPSTEM), 2026

Volume 39, Pages 30-39

IConTech 2026: International Conference on Technology

Assessment of Fracture Properties in Lime-Pumice Mortars Through the Utilization of Various Specimen Types

Ragip Ince
Firat University

Erkin Eren
Firat University

Abstract: Linear elastic fracture mechanics (LEFM) were initially applied to cementitious materials by Kaplan in 1961, followed by Kesler and his colleagues in 1972. The latter group found that LEFM was inadequate for concrete. This limitation stems from the relatively inelastic region found in quasi-brittle materials, such as concrete mixtures, rocks, and bituminous substances, which are significantly and completely fractured in advance of the crack tip. As a result, many researchers have developed non-Hookean fracture mechanics methodologies to accurately describe fracture-dominated failures in quasi-brittle structures. In this investigation, beams and single-notch cube bending (SNCB) specimens with three distinct initial crack lengths were fabricated to ascertain the fracture parameters of lime-pumice mortars. All specimens, featuring a maximum aggregate diameter of 4 mm, were maintained wrapped in stretch film within the mold for 28 days, after which they underwent three-point bending tests. The fracture parameters of the mixtures were assessed using the modified peak load method, which was recently formulated to evaluate the fracture characteristics of TPM.

Keywords: Fracture mechanics, Lime, Pumice, Two-parameter model

Introduction

The application of Linear Elastic Fracture Mechanics (LEFM) to concrete began with Kaplan in 1961. However, during the 1970s, extensive experimental studies revealed that LEFM was insufficient for cement-based materials (Kesler et al., 1972). This limitation arose from the presence of an inelastic zone characterized by large-scale and fully developed cracks at the crack tip in concrete. LEFM overlooked this fracture process zone (FPZ). Consequently, various researchers have formulated nonlinear fracture mechanics methods to effectively characterize the FPZ. Initially, computational techniques known as cohesive crack models were introduced, which simulate the FPZ by applying a closing pressure that diminishes as it approaches the crack tip (Hillerborg et al., 1976; Bazant & Oh, 1983). Following this, deterministic size effect models were proposed to explain fracture-dominated failures in concrete structures, as the length of the FPZ decreases with increasing structural size. Furthermore, effective crack models, including the two-parameter fracture model (TPM) (Jenq & Shah, 1985), the effective crack model (Nallathambi & Karihaloo, 1986) the size effect model (SEM) (Bazant & Kazemi, 1990), the double-K model (Xu & Reinhardt, 1999), and the boundary effect method (Hu & Duan, 2008), were developed to simulate the FPZ using an effective crack length.

In order to examine a concrete structure concerning fracture mechanics, it is essential to first ascertain its fracture parameters. The notched beam tests are employed initially, as beams were extensively utilized in the early LEFM test standards for metals in concrete fracture. While both beams and compact tension (CT) specimens with cracks are commonly used to assess fracture properties of quasi-brittle materials and metals, the adoption of compact specimens has recently gained traction for cementitious materials, rock, and asphalt concrete. Wedge-splitting specimens and compact compression specimens have been introduced as alternatives

- Selection and peer-review under responsibility of the Organizing Committee of the Conference

to CT specimens and are frequently utilized to evaluate the nonlinear fracture properties of cementitious composites such as mortar and concrete (Ince & Bildik, 2021). Although splitting specimens in cylindrical and cubical shapes have been widely employed to indirectly assess the tensile strength of quasi-brittle materials, their centrally notched variants have also been utilized to determine the nonlinear fracture properties of cementitious materials. Ince (2021) modeled edge-notched mortar cubes, which function as splitting specimens, using the TPM. Eren and Ince (2025) applied SNCB specimens to lime-pumice mixtures. The semi-circular bending (SCB) specimens are the most prevalent samples in fracture testing of rock and asphalt materials, as they can be easily fabricated from cylindrical core samples. Ince et al. (2024) initially established some LEFM relationships concerning crack blunting in SCB specimens and subsequently simulated various SCB tests on asphalt from the literature using the TPM in concrete fracture. Recently, Ince (2025a) carried out two series of experimental investigations with SCB and beam specimens composed of concrete and mortar, discussing the findings based on the three most recognized fracture models: the TPM, the SEM, and the double-K model. Subsequently, three sets of SCB rock tests from the literature were examined utilizing the previously mentioned concrete fracture models, highlighting that the nonlinear fracture characteristics of both rock and concrete materials can be accurately evaluated using single-sized SCB specimens. The fracture tests from comparative studies on beams and single-notch cube bending (SNCB) specimens conducted by Ince and Eren (2026) demonstrate that the fracture characteristics of rocks, as determined by the TPM and the double-K model, can be readily estimated through SNCB specimen tests, thereby negating the need for specimens of varying sizes.

In this study, beams and SNCB specimens with three different initial crack lengths were created to determine the fracture parameters of lime-pumice mortars. All specimens, which had a maximum aggregate diameter of 4 mm, were kept wrapped in stretch film inside the mold for 28 days, after which they were subjected to three-point bending tests. The fracture properties of the mortars were evaluated using the modified peak load method, a recent development aimed at assessing the fracture characteristics of TPM.

The Two-Parameter Model (TPM) in Fracture Mechanics of Cementitious Materials

TPM advises that for the fracture criteria, the stress intensity factor K_I and the crack tip opening displacement *CTOD* must attain their critical values, K^s_{Ic} and $CTOD_c$, as depicted in Figure1. These fracture parameters can be calculated using the subsequent LEFM equations:

$$K_{Ic}^{s} = \sigma_{Nc}\sqrt{\pi a_c}\,Y\left(g,l\right) \tag{1}$$

$$CTOD_c = \frac{\gamma\sigma_{Nc}a_c}{E}V_1\left(g,l\right)M\left(g,l\right) \tag{2}$$

Here, σ_{Nc} refers the nominal strength, E denotes elasticity modulus, and Y, V_1, and M are normalized functions of both the structural geometry (g) and the loading configuration (l). In Eq. (2), the coefficient γ takes the value of π for splitting specimens and 4 for beams. The term Y is commonly referred to as the geometry factor, while M is obtained from the ratio COD(a_c)/CMOD$_c$, where $CMOD_c$ corresponds to the critical crack mouth opening displacement. The TPM is particularly convenient for structural applications, since the functions Y, V_1, and M can be readily found in LEFM handbooks (Tada et al., 2000).

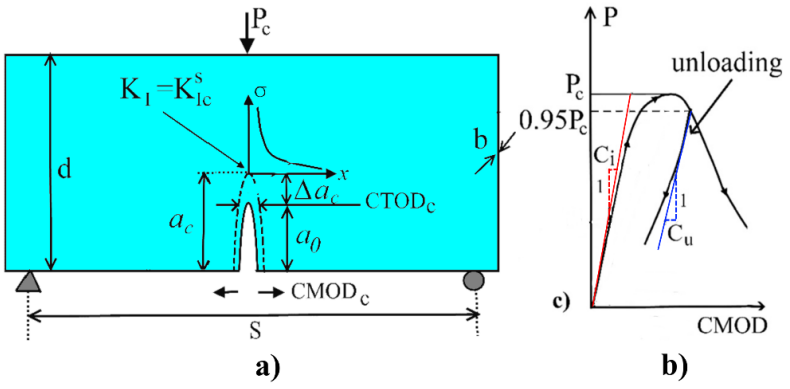

Figure 1. a) Simulation of beams based on TPM b) typical load-CMOD curve

In this methodology, the fracture parameters can be inferred from one of two distinct experimental techniques, specifically the compliance method introduced by RILEM (Shah, 1990) and the peak load method established by Tang et al. (1996). In the initial technique, these parameters are ascertained from the correlation between load and crack mouth opening displacement (P-CMOD) of three-point bending specimens featuring a central edge notch in Figure 1a, utilizing closed-loop testing apparatus. The critical crack length a_c is derived from two measurements obtained from the P-CMOD curve: the initial compliance and the unloading compliance, which is recorded at approximately 95% of the peak load during the descending phase, as shown in Figure 1b. The peak-load method, on the other hand, removes the necessity for complex closed-loop apparatus, thereby offering a more straightforward alternative to the RILEM compliance-based procedure for determining fracture parameters in TPM. However, this method still necessitates a minimum of three specimens to address the variability that is intrinsic to concrete. The test specimens can either possess the same geometrical dimensions but vary in their initial notch lengths, or they may maintain uniform notch sizes while differing in overall dimensions. For each specimen, the governing equations of TPM can be articulated as outlined by Tang et al. (1992).

$$\begin{aligned} K_I^i\left(\sigma_{Nc}^i, a_c^i\right) &= K_{Ic}^s \qquad , i = 1,2 \\ CTOD^i\left(\sigma_{Nc}^i, a_c^i\right) &= CTOD_c \end{aligned} \tag{3}$$

here i denotes the ith specimen. As a result, the parameters related to fractures can be determined by concurrently solving four non-linear equations. Nevertheless, it is essential to test three or more different specimens to guarantee statistically valid outcomes, as random errors are invariably present in the measured values of σ^1_{Nc} and σ^2_{Nc}.

Ince (2025b) has recently introduced a modified peak load method that employs an optimization procedure to determine K^s_{Ic} and $CTOD_c$. This methodology relies on the simultaneous resolution of equation (3), which serves as the failure criterion for a concrete structure. As previously stated, the primary objective of any fracture model is to assess the critical crack extension (Δa_c) at the peak load, as depicted in Figure 1a. Therefore, for this particular issue, it may be adequate to identify the nominal strength value (σ_{Nc}) that corresponds to the peak load, along with the Δa_c value for the initial crack length (a_0) for each specimen. The Δa_c values computed for each specimen should ensure that the same fracture parameters (K^s_{Ic} and $CTOD_c$) are satisfied across all tested specimens. Nevertheless, achieving an exact solution for a heterogeneous material such as concrete is unattainable. As a result, this issue can only be addressed through optimization techniques. To ascertain the fracture parameters of the TPM, the following two expressions were initially minimized by applying the least squares error criterion:

$$f\left(K_{Ic}^s\right) = \sum_{i=1}^{n} \Delta^2\left(K_{Ic}^s\right) = \sum_{i=1}^{n}\left(K_{Ic,i}^s - \overline{K_{Ic,i}^s}\right)^2 \tag{4}$$

$$f\left(CTOD_c\right) = \sum_{i=1}^{n} \Delta^2\left(CTOD_c\right) = \sum_{i=1}^{n}\left(CTOD_{c,i} - \overline{CTOD_{c,i}}\right)^2 \tag{5}$$

In which n is the number of samples experimented, $\overline{K_{Ic,i}^s}$ is the mean value of K^s_{Ic} and $K^s_{Ic,i}$ is the value of K^s_{Ic} or the i^{th} sample in Equation 4 while $\overline{CTOD_{c,i}}$ is the mean value of $CTOD_c$ and $CTOD_{ci}$ is the value of $CTOD_c$ for the i^{th} sample in Equation 5. Conversely, to achieve a simultaneous resolution of the aforementioned two minimization equations, the root sum squared (RSS) method, also referred to as the statistical tolerance analysis method, was employed as detailed below:

$$RSS = \sqrt{\left(f\left(K_{Ic}^s\right)\right)^2 + \left(f\left(CTOD_c\right)\right)^2} \tag{6}$$

It is important to recognize that while K^s_{Ic} and $CTOD_c$ are typically expressed in MPa√m and mm, respectively, it is advisable to utilize MPa√mm and μm instead, as the values represented by these units differ significantly. The aforementioned procedures, which underpin the modified peak load method, can be readily executed using a spreadsheet application like the MS-EXCEL-based SOLVER toolkit.

Experimental Program

In this study, by using CL-80-S type lime, pozzolanic activity tests of pumice material were first carried out according to TS 25 (1975). For this purpose, lime-pumice mortar was poured into cement molds (40 × 40 × 160 mm) containing three standard prismatic cavities, according to the mixing ratios recommended in TS 25 (1975). The samples were covered with hard mica material, wrapped in stretch film, and left to set for 1 day, then kept in an oven at 55°C for 1 week. Four hours before the bending test, the samples were removed from the oven and allowed to cool. Then, they were first subjected to a three-point bending test in a cement testing machine with a capacity of 30 kN and a support span of 100 mm. Six samples obtained from the three bending specimens, which were divided in two, were subjected to a compression test in a cement press with a capacity of 40 kN on a 40 × 40 mm loading area. As a result, the flexural-tensile strength of the lime-pumice mortar was obtained as 2.3 MPa > 1.0 MPa and the compressive strength as 4.4 MPa > 4.0 MPa, and it was determined that the pozzolanic activity of the pumice material conforms to TS 25 (1975).

The mixtures with a maximum aggregate diameter of 4 mm were in a water: lime: pumice: aggregate ratio of 1.53:1.00:1.00:6.00 by using two different lime types, namely CL-80-S lime with the specific gravity=2.08 and CL-90-S lime with the specific gravity=2.09. As shown in Table 1, in this study, mixtures with CL-80-S lime and with CL-90-S lime were named Mixture 1 and Mixture 2, respectively. The aggregate was air-dried prior to mixing. The Fuller parabola was used to determine the percentages of the aggregate gradation.

Beams with width × depth × length of 50×50×150 mm and square prismatic specimens with 50×150×150 mm were produced from Mixture 1, while cubes with 100 mm were produced from Mixture 2. In addition to the notched specimens, cubes (100 mm) were made to determine compressive strength. Specimens left in molds outdoors for 24 hours were then covered with stretch film and saved in the molds for 28 days. After 28 days, the modulus of elasticity was determined for the beams of Mixture 1 and the cube specimens of Mixture 2 using ultrasonic testing techniques. In this study, by using the following formulas, the dynamic modulus of elasticity of the material was determined for prismatic specimens and cubical specimens, respectively:

$$E_d = 10^3 V^2 \Delta, \quad \text{MPa} \tag{7}$$

$$E_d = 10^3 \frac{V^2 \Delta (1+\nu)(1-2\nu)}{1-\nu}, \quad \text{MPa} \tag{8}$$

where, V is the velocity (km/s) and Δ is the unit weight (kg/lt). Since lime-pumice mixtures are low strength materials, the Poisson ratio (ν) was taken as 0.3 in this study (Erdogan, 2003). Note that the dynamic modulus of elasticity of the material (E_d) are larger than the static modulus of elasticity (E_s). The formula: E_s=6/7×E_d was used for lime-pumice mixtures in this study (Lydon, 1984). Physical and mechanical properties of lime-pumice mixtures used in this study are summarized in Table 1.

The specimens were notched with a diamond saw blade of 1.5 mm thickness on the day of the fracture test. Subsequently, the compression tests and the bending tests were performed using a digital compression machine with a capacity of 100 kN. The specimens were loaded monotonically until final failure and care was taken to apply a constant loading rate (Figure 2). Typically, approximately 2 min (± 30 sec) elapsed before the maximum load capacity for each specimen was reached.

The specimen width (b), specimen depth (d) and the peak load values (P_c) of the notched beams and the SNCB specimens are reported in Table 2 and Table 3 according to the notch depths (a_0), respectively. In these tables, the letters B and S refer to beams and SNCB specimens. The following numbers in SNCB specimens in Table 3 represent the specimen size. Crack patterns at the failure of beams and compression cubes are shown in Figure 3.

Table 1. Physical and mechanical properties of lime-pumice mixtures used in this study

Mix	Lime	Δ g/cm^3	f_c MPa	E_s MPa
Mixture1	CL-80-S	1.93	3.79	13384
Mixture2	CL-90-S	2.03	3.75	12537

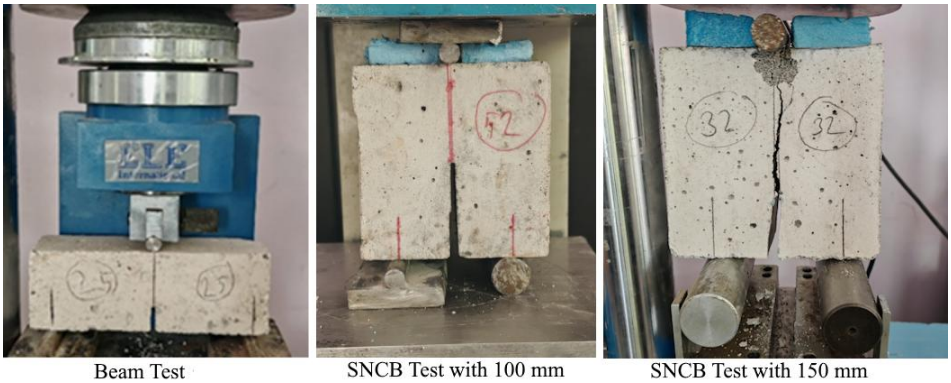

Beam Test | SNCB Test with 100 mm | SNCB Test with 150 mm

Figure 2. Test setup of the notched specimens

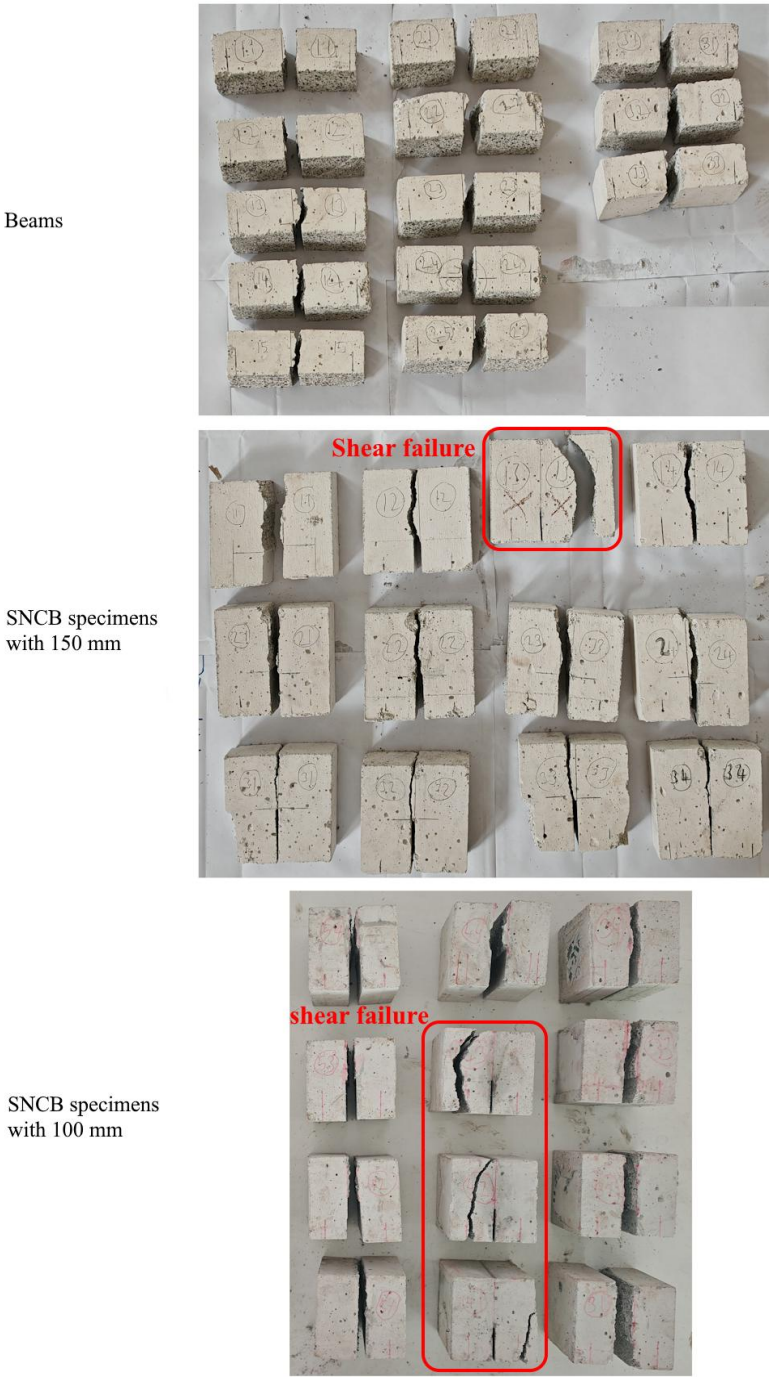

Figure 3. Crack patterns and failure mechanisms of notched specimens

Table 2. Test results of specimens with mixture 1 tested in this study

Specimen	b mm	d mm	a_0 mm	P_c kN	Specimen	b mm	d mm	a_0 mm	P_c N
S150-1	51.30	150.35	47.94	4.97	B1	47.77	49.32	8.84	540
S150-2	51.14	150.49	47.63	4.13	B2	50.85	50.3	9.99	460
S150-3	52.43	150.92	47.30	4.98	B3	54.16	49.63	9.71	590
S150-4	51.10	152.44	60.50	3.80	B4	50.41	50.23	9.36	680
S150-5	51.52	151.60	61.04	3.67	B5	52.08	50.41	9.93	520
S150-6	52.15	150.06	58.12	5.36	B6	53.65	50.03	15.00	350
S150-7	50.89	150.86	59.23	3.83	B7	54.26	49.84	14.26	490
S150-8	50.51	151.11	74.89	3.39	B8	49.26	50.05	13.58	410
S150-9	55.57	149.83	68.99	3.70	B9	52.21	51.28	15.79	460
S150-10	52.32	150.89	72.79	3.73	B10	52.32	50.72	15.42	450
S150-11	45.76	150.71	71.00	3.69	B11	48.02	49.63	23.12	290
					B12	50.32	49.17	21.84	250
					B13	55.85	49.21	21.43	320

Table 3. Test results of specimens with mixture 2 tested in this study

Specimen	b(mm)	d(mm)	a_0(mm)	P_c(kN)
S100-1	99.96	100.29	31.00	9.01
S100-2	99.93	99.78	30.46	9.25
S100-3	99.82	99.73	29.93	8.76
S100-4	99.94	99.34	31.48	9.52
S100-5	100.08	100.23	39.95	5.40
S100-6	99.81	99.80	50.40	5.91
S100-7	99.92	99.17	50.21	8.68
S100-8	99.94	99.80	50.42	5.32
S100-9	100.03	104.08	54.24	4.37

Applications of the Modified Peak Load Method to Lime-Pumice Mixtures

As shown in Figure 3, one of the 150 mm SNCB specimens experienced shear fracture instead of bending fracture along the crack line. Shear fracture also occurred in three of the 100 mm SNCB specimens. The most important reason for this is that SNCB specimens behave like deep beams, where the depth of the compression zone is larger than that of the beam under three-point bending loading (Ince & Eren, 2026). For this reason, these four specimens were not taken into consideration in the following analysis. The modified peak load method's specific applications to mixtures in this investigation are shown in Tables 4, 5, and 6. On the other hand, the beam and SNCB specimens were also analyzed together in Table 7 since they were produced from the same mixture in Table 2 (Mixture 1). The first two columns of these tables provide a summary of the test results for each sample. For beams and SNCB specimens, the nominal strengths were calculated as $\sigma_{Nc}=3.75P/(b\times d)$ and $\sigma_{Nc}=P/(2\times b\times d)$, respectively.

Table 4. Application of the modified peak load method to SNCB specimens with mixture 1

No	a_0 mm	σ_{Nc} MPa	Δa mm	a_c mm	a_c/d	Y	K^s_{Ic} MPa√mm	V_1	$CTOD_c$ µm		$\Delta^2(K^s_{Ic})$	$\Delta^2(CTOD_c)$
1	47.94	0.322	3.85	51.79	0.344	1.236	5.08	11.95	2.41		0.2418	0.0790
2	47.63	0.268	6.85	54.48	0.362	1.273	4.47	12.30	2.89		1.2215	0.5759
3	47.30	0.315	4.28	51.58	0.342	1.231	4.93	11.90	2.50		0.4101	0.1376
4	60.50	0.244	5.24	65.74	0.431	1.470	5.15	14.24	2.46		0.1763	0.1110
5	61.04	0.235	5.64	66.68	0.440	1.501	5.10	14.55	2.52		0.2207	0.1483
6	58.12	0.342	1.64	59.76	0.398	1.365	6.41	13.19	1.68		0.6948	0.1985
7	59.23	0.249	5.13	64.36	0.427	1.454	5.16	14.08	2.46		0.1727	0.1071
8	74.89	0.222	2.28	77.17	0.511	1.814	6.27	17.91	1.56		0.4889	0.3287
9	68.99	0.222	3.86	72.85	0.486	1.692	5.69	16.57	2.03		0.0134	0.0101
10	72.79	0.236	2.14	74.93	0.497	1.742	6.31	17.12	1.55		0.5485	0.3324
11	71.00	0.268	1.44	72.44	0.481	1.667	6.73	16.30	1.37		1.3308	0.5786
						Mean	5.57	Mean	2.13	Σ	5.5195	2.6071
											RSS	6.1042

The crack extensions (Δa_c), which were considered variables in the optimization problem, were initially chosen to be 5 mm for each sample. While the function of M in Equation 2 is shown as embedded in $CTOD_c$, the normalized functions of the cracked structure, such as Y and V_1, were also reported. The MS-EXCEL-based SOLVER toolbox was used for all analyses. The minimized values in these tables are the root sum squared (RSS) values.

Table 5. Application of the modified peak load method to beam with mixture 1

No	a_0 mm	σ_{Nc} MPa	Δa mm	a_c mm	a_c/d	Y	K^s_{Ic} MPa√mm	V_1	$CTOD_c$ µm		$\Delta^2(K^s_{Ic})$	$\Delta^2(CTOD_c)$
1	8.84	0.860	4.68	13.52	0.274	0.967	5.41	1.559	2.931		0.0012	0.0008
2	9.99	0.674	6.59	16.58	0.330	1.018	4.95	1.731	3.302		0.1807	0.1171
3	9.71	0.823	4.65	14.36	0.289	0.979	5.41	1.601	2.934		0.0010	0.0007
4	9.36	1.007	2.99	12.35	0.246	0.949	5.95	1.491	2.509		0.3260	0.2029
5	9.93	0.743	5.62	15.55	0.309	0.996	5.17	1.659	3.129		0.0435	0.0286
6	15.00	0.489	6.87	21.87	0.437	1.188	4.82	2.263	3.417		0.3170	0.2093
7	14.26	0.679	4.11	18.37	0.369	1.068	5.51	1.888	2.853		0.0173	0.0113
8	13.58	0.624	5.31	18.89	0.377	1.081	5.19	1.929	3.112		0.0348	0.0231
9	15.79	0.644	3.96	19.75	0.385	1.093	5.55	1.966	2.826		0.0283	0.0180
10	15.42	0.636	4.21	19.63	0.387	1.096	5.47	1.975	2.885		0.0086	0.0056
11	23.12	0.456	2.80	25.92	0.522	1.420	5.85	3.001	2.558		0.2182	0.1617
12	21.84	0.379	4.87	26.71	0.543	1.495	5.19	3.251	3.129		0.0361	0.0285
13	21.43	0.437	3.97	25.40	0.516	1.398	5.45	2.932	2.894		0.0056	0.0043
						Mean	5.38	Mean	2.96	Σ	1.2184	0.8119
											RSS	1.44641

Table 6. Application of the modified peak load method to SNCB specimens with mixture 2

No	a_0 mm	σ_{Nc} MPa	Δa mm	a_c mm	a_c/d	Y	K^s_{Ic} MPa√mm	V_1	$CTOD_c$ µm		$\Delta^2(K^s_{Ic})$	$\Delta^2(CTOD_c)$
1	32.00	0.449	6.31	38.31	0.382	1.321	6.51	12.76	4.36		0.7420	0.4131
2	30.46	0.464	6.31	36.77	0.369	1.288	6.42	12.44	4.40		0.9094	0.4735
3	29.93	0.440	7.23	37.16	0.373	1.297	6.17	12.53	4.60		1.4549	0.7796
4	31.48	0.479	5.54	37.02	0.373	1.298	6.71	12.54	4.20		0.4412	0.2328
5	39.95	0.269	3.45	43.40	0.433	2.502	7.86	25.74	3.45		0.2414	0.0715
6	50.40	0.297	4.35	54.75	0.549	2.038	7.93	20.48	3.16		0.3083	0.3138
7	50.21	0.438	0.92	51.13	0.516	1.840	10.22	18.21	1.65		8.0825	4.2657
8	50.42	0.267	5.63	56.05	0.562	2.128	7.53	21.53	3.56		0.0243	0.0248
9	54.24	0.210	7.74	61.98	0.595	2.395	7.01	24.77	4.07		0.1295	0.1253
						Mean	7.37	Mean	3.72	Σ	12.3335	6.7001
											RSS	14.0358

Table 7. Application of the modified peak load method to beams and SNCB specimens with mixture 1

No	a_0 mm	σ_{Nc} MPa	Δa mm	a_c mm	a_c/d	Y	K^s_{Ic} MPa√mm	V_1	$CTOD_c$ µm	$\Delta^2(K^s_{Ic})$	$\Delta^2(CTOD_c)$
1	47.94	0.322	7.98	55.92	0.372	1.296	5.53	12.52	3.87	0.1631	0.0569
2	47.63	0.268	11.55	59.18	0.393	1.351	4.94	13.05	4.26	0.9891	0.3919
3	47.30	0.315	8.58	55.88	0.370	1.292	5.39	12.48	3.96	0.3040	0.1059
4	60.50	0.244	9.42	69.92	0.459	1.573	5.69	15.30	3.81	0.0629	0.0317
5	61.04	0.235	9.83	70.87	0.467	1.609	5.64	15.68	3.84	0.0875	0.0454
6	58.12	0.342	4.52	62.64	0.417	1.424	6.84	13.77	3.07	0.8137	0.3126
7	59.23	0.249	9.28	68.51	0.454	1.555	5.69	15.11	3.81	0.0613	0.0308
8	74.89	0.222	5.66	80.55	0.533	1.940	6.85	19.35	2.89	0.8416	0.5451
9	68.99	0.222	7.67	76.66	0.512	1.819	6.27	17.97	3.37	0.1125	0.0687
10	72.79	0.236	5.45	78.24	0.519	1.857	6.88	18.39	2.89	0.8831	0.5433
11	71.00	0.268	4.27	75.27	0.499	1.756	7.22	17.27	2.68	1.6568	0.9071
1	8.84	0.860	6.14	14.98	0.304	0.991	5.85	1.644	3.72	0.0084	0.0075
2	9.99	0.674	8.19	18.18	0.361	1.058	5.39	1.857	4.13	0.2982	0.2461
3	9.71	0.823	6.12	15.83	0.319	1.006	5.84	1.693	3.72	0.0094	0.0083
4	9.36	1.007	4.24	13.60	0.271	0.964	6.35	1.550	3.25	0.1663	0.1472

5	9.93	0.743	7.18	17.11	0.339	1.029	5.60	1.767	3.94		0.1107	0.0943
6	15.00	0.489	8.35	23.35	0.467	1.256	5.26	2.477	4.25		0.4568	0.3836
7	14.26	0.679	5.46	19.72	0.396	1.110	5.93	2.019	3.63		0.0000	0.0000
8	13.58	0.624	6.77	20.35	0.407	1.129	5.63	2.079	3.92		0.0947	0.0828
9	15.79	0.644	5.30	21.09	0.411	1.137	5.97	2.105	3.60		0.0008	0.0007
10	15.42	0.636	5.57	20.99	0.414	1.142	5.90	2.119	3.67		0.0016	0.0015
11	23.12	0.456	3.82	26.94	0.543	1.494	6.27	3.248	3.29		0.1123	0.1195
12	21.84	0.379	6.04	27.88	0.567	1.594	5.65	3.585	3.92		0.0805	0.0827
13	21.43	0.437	5.12	26.55	0.539	1.481	5.91	3.204	3.66		0.0010	0.0010
						Mean	5.94	Mean	3.63	Σ	7.3161	4.2146
											RSS	8.4433

The following formulas were applied to beams with a span/depth ratio of 2.5 in this study (Yang et al., 1997):

$$Y(\alpha)=\frac{1.83-1.65\alpha+4.76\alpha^2-5.3\alpha^3+2.51\alpha^4}{\sqrt{\pi}(1+2\alpha)(1-\alpha)^{3/2}} \tag{9}$$

$$V_1(\alpha)=0.65-1.88\alpha+3.02\alpha^2-2.69\alpha^3+\frac{0.68}{(1-\alpha)^2} \tag{10}$$

$$M(\alpha_0,\alpha_c)=\sqrt{\left(1-\frac{\alpha_0}{\alpha_c}\right)^2+(1.081-1.149\alpha_c)\left[\frac{\alpha_0}{\alpha_c}-\left(\frac{\alpha_0}{\alpha_c}\right)^2\right]} \tag{11}$$

For the SNCB specimens with span/depth=0.6, the LEFM formulas were given by Ince & Eren (2026):

$$Y(\alpha)=\frac{2.854-16.967\alpha+60.766\alpha^2-102.025\alpha^3+84.581\alpha^4-27.245\alpha^5}{(1+2\alpha)(1-\alpha)^{3/2}} \tag{12}$$

$$V_1(\alpha)=8.691-27.46\alpha+5.715\alpha^2+74.589\alpha^3-101.024\alpha^4+\frac{4.476}{(1-\alpha)^2} \tag{13}$$

$$M(\alpha_0,\alpha_c)=\sqrt{\left(1-\frac{\alpha_0}{\alpha_c}\right)^2+(1.007-2.747\alpha_c+2.018\alpha_c^2)\left[\frac{\alpha_0}{\alpha_c}-\left(\frac{\alpha_0}{\alpha_c}\right)^2\right]} \tag{14}$$

Conclusion

The presented work investigated the fracture behavior of lime-pumice mixtures using the modified peak load method based on the two-parameter model in fracture mechanics of concrete. The results of this study are summarized below:

When comparing Table 6 and Table 7, SNCB specimens, previously used successfully to determine the nonlinear fracture properties of rock materials, were applied to lime-pozzolan mortars for the first time in this study. Comparative analyses revealed that the results of beam and SNCB specimens produced from the same mixture were in good agreement.

Although the amount of $Ca(OH)_2$ in CL-90-S limes is approximately 10% higher than in CL-80-S lime material in practice, other chemical and physical properties are almost the same. Consequently, the fracture toughness value of lime-pumice mortar with CL-90-S is approximately 25% greater than that of mortar with CL-80-S. On the other hand, no significant difference is observed between the crack tip opening displacement values.

It is accepted that using different specimen types together in the peak-load method for concrete fracture will yield much more reliable results. One of the important results of this study shows that this use of different specimens is also valid for the modified peak-load method.

Recommendations

Further studies can come up with more reliable results by investigating various types and sizes of aggregates to verify the above findings.

Scientific Ethics Declaration

* The authors declare that the scientific ethical and legal responsibility of this article published in EPSTEM journal belongs to the authors.

Conflict of Interest

* The authors declare that they have no conflicts of interest

Acknowledgements or Notes

* This article was presented as an oral presentation at the International Conference on Technology (www.icontechno.net) held in Budapest/Hungary on February 05-08, 2026.

* This article is extracted from the second author's doctorate dissertation entitled "Investigation of Structures Produced from Historical Mortars Using Fracture Mechanics Principles", supervised by Ragip Ince.

* Erkin Eren would like to thank the Scientific and Technological Research Council of Turkey (TÜBİTAK) for supporting his doctoral education with the Domestic General Doctoral Scholarship Program (2211-A).

References

Bažant, Z. P. & Kazemi, M. T. (1990). Determination of fracture energy, process zone length, and brittleness number from size effect with application to rock and concrete. *International Journal of Fracture*, *44(2)*, 111-131.

Bažant, Z. P. & Oh, B. H. (1983). Crack band theory for fracture concrete. *Materials & Structures (RILEM)*, *16*(93), 155-157.

Erdogan, T. Y. (2003). *Concrete*. METU Press.

Eren, E. & Ince, R. (2025). Evaluation of nonlinear fracture quantities in lime-pumice mixtures. *The Eurasia Proceedings of Science, Technology, Engineering and Mathematics (EPSTEM), 38,* 672-681.

Hillerborg, A., Modeer, M., & Petersson, P. E. (1976). Analysis of crack formation and crack growth in concrete by means of fracture mechanics and finite elements. *Cement & Concrete Research*, *6*, 773-782.

Hu, X. & Duan K. (2008). Size effect and quasi-brittle fracture: the role of FPZ. *International Journal of Fracture*, *154*, 3–14.

Ince, R. & Bildik A. T. (2021). A preliminary concrete mixture design based on fracture toughness. *Materials and Structures*, *54*:11.

Ince, R. & Eren E. (2026). Utilizing cylindrical and cubical specimens with edge notch to determine size-independent fracture quantities of rock materials. *Fracture and Structural Integrity*, *75*, 435-462.

Ince, R. (2021). Utilization of splitting strips in fracture mechanics tests of quasi-brittle materials. *Archive of Applied Mechanics*, *91*, 2661–2679.

Ince, R. (2025a). Using SCB specimens to quantify nonlinear fracture characteristics in concrete and rock materials. *Engineering Fracture Mechanics*, *318*, 110951.

Ince, R. (2025b). A modified peak load method based on the two-parameter fracture model in concrete fracture. *The Eurasia Proceedings of Science, Technology, Engineering and Mathematics (EPSTEM), 36,* 141-150.

Ince, R., Yalcin, E. & Yilmaz, M. (2024). Quantifying nonlinear fracture parameters in bituminous SCB specimens: A compliance-based approach. *Case Studies in Construction Materials*, *21*, e03437.

Jenq, Y. S. & Shah, S. P. (1985). Two-parameter fracture model for concrete. *ASCE Journal of Engineering Mechanics*, *111*(10), 1227-1241.

Kaplan, M. F. (1961). Crack propagation and the fracture of concrete. *ACI Journal*, *58*(11), 591-610.

Kesler, C. E, Naus, D. J. & Lott, L. L. (1972). Fracture mechanics-its applicability to concrete. *The Society of Materials Science,* 113-124.

Lydon, F. D. (1984). *Concrete mix design*. Applied Science publishers.

Nallathambi, P. & Karihaloo, B. L. (1986). Determination of the specimen size independent fracture toughness of plain concrete. *Magazine of Concrete Research*, *38(135)*, 67-76.

Shah, S. P. (1990). Determination of fracture parameters (KsIc sand CTODc) of plain concrete using three-point bend tests. *Materials and Structures (RILEM), 23,* 457-460.

Tada, H., Paris, P. C. & Irwin, G. R. (2000). *The stress analysis of cracks handbook*, Third Edition, ASME Press.

Tang, T., Ouyang, C. & Shah, S. P. (1996). A simple method for determining material fracture parameters from peak loads. *ACI Materials Journal*, *93*(2), 143-157.

Tang, T., Shah, S. P. & Ouyang, C. (1992). Fracture mechanics and size effect of concrete in tension. *ASCE Journal of Structural Engineering*, *118*, 3169–3185.

TS 25 (1975). *Natural pozzolan (trass) for use in cement and concrete- definitions, requirements and conformity criteria*. Turkish Standard Institute. (in Turkish)

Xu, S. & Reinhardt, H. W. (1999). Determination of double-K criterion for crack propagation in quasi-brittle fracture, Part I: experimental investigation of crack propagation. *International Journal of Fracture*, *98*, 111-149.

Yang, S., Tang, T., Zollinger, D. G. & Gurjar, A. (1997). Splitting tension tests to determine concrete fracture parameters by peak–load method. *Advanced Cement Based Materials*, *5*, 18–28.

Author(s) Information

Ragip Ince
Firat University, Engineering Faculty, Elazig, Türkiye
*Contact e-mail: *rince@firat.edu.tr*
ORCID iD: https://orcid.org/0000-0002-9837-8284

Erkin Eren
Firat University, Engineering Faculty, Elazig, Türkiye
ORCID iD: https://orcid.org/0000-0001-5282-398X

*Corresponding authors contact email

To cite this article:

Ince, R., & Eren, E. (2026). Assessment of fracture properties in lime-pumice mortars through the utilization of various specimen types. *The Eurasia Proceedings of Science, Technology, Engineering and Mathematics (EPSTEM), 39,* 30-39.

The Eurasia Proceedings of Science, Technology, Engineering and Mathematics (EPSTEM)
ISSN: 2602-3199

The Eurasia Proceedings of Science, Technology, Engineering and Mathematics (EPSTEM), 2026

Volume 39, Pages 40-49

IConTech 2026: International Conference on Technology

Harmonic Injection Scenarios for Enhanced DC-Link Utilization in Seven-Phase VSI-Fed Motor Drives

Yasir M. Y. Ameen
University of Mosul

Marwan H. Mohammed
University of Mosul

Marwan Mohammed Alwan
University of Fallujah

Abstract: Multiphase motor drives have enjoyed a lot of attention because they have a higher credibility of reliability, less torque ripple, and flexible fault tolerance as opposed to the conventional three-phase systems. Specifically, the seven-phase voltage source inverter (VSI) fed motor drives give extra modulation design and harmonic control degrees of freedom. But conventional sinusoidal pulse width modulation (SPWM) will restrict the fundamental voltage actually available in the linear modulation area and can result in poor harmonic performance at high modulation. The paper includes a comparative systematic investigation of harmonic injection pulse width modulation strategies of a two-level seven-phase VSI to serve a seven-phase motor drive. A number of injection cases are studied such as single harmonic injection (3^{rd} , 5^{th} and 7^{th}), combined harmonic injections and triple harmonic injected. Effects of each configuration are considered with regard to the maximum possible fundamental modulation index, total harmonic distortion (THD) of the phase voltage, and a voltage based torque ripple index (TRI). Generalized reference waveform formulation that involves the ability to choose harmonic amplitude and phase shifts is created and provided in MATLAB to assess performance comprehensively. The outcomes of the simulation prove that low-order harmonic injection, the third and the fifth harmonics in particular, can effectively enhance the utilization of the DC-link voltages by flatting the peaks of the reference waveform and expanding the linear modulation range. There is however, an increase in harmonic distortion and torque ripple. Conversely, seventh harmonic injection displays insignificant effect on fundamental voltage enhancement and has lowest THD and TRI since it is basically a common-mode phenomenon in seven-phase systems. The results obtained indicate a definite trade-off between DC-link utilization and quality of the waveforms positioned at the significance of choosing a suitable harmonic injection strategy based on the requirement of the application.

Keywords: Seven-phase inverter, Multiphase motor drives, Harmonic injection PWM

Introduction

The use of multiphase VSI-based drives has become a promising alternative to traditional three phase systems in high reliability and high power systems, because it offers the necessary benefits of enhanced fault tolerance, lower torque ripple and decreased DC link capacitor ratings (Ameen et al.,2020; Sultan& Al-Badrani, 2023). Phase VSI fed drives are of specific interest to this class due to the higher degrees of freedom of the space vector representation that allow the independent control of different harmonic subspaces and provide a significantly greater flexibility of modulation (Casadei et al., 2008; Hamedani, 2020). Such capabilities can be used to enhance the use of DC link voltages, enhance the density of the torque, and tailor harmonic spectra to meet application requirements (Yang et al., 2021; Yang et al., 2023). Nevertheless, though it has the advantages of space vector modulation, especially the positive realization of enchaining DC-link utilization, it has the

disadvantage of complexity in implementation when compared to the traditional sinusoidal pulse width modulation (SPWM), which is still common because of its simplicity and satisfactory performance in the linear modulation range (Hamedani, 2020; Batkhishig et al., 2025).

As a matter of fact, in multiphase inverters, traditional SPWM approach can result in poorer performance in cases where a larger fundamental voltage is needed, e.g. when running at high speed or in flux weakening areas, hence the question that has been posed here is: Is it possible to combine the good characteristics of Space Vector Modulation with the advantages of SPWM? The short answer to that is yes, but with an appropriate modification to the reference signal or modulation signal by injecting desired harmonic components. Consequently, several more advanced modulation schemes have been suggested, such as general carrier based schemes of seven phase inverters, universal sequential over modulation schemes, optimized harmonic injection PWM schemes of multilevel converters (Yang et al., 2021; Casadei et al., 2008; Yeganeh et al., 2020; Yang et al., 2023). These methods prove that reference waveforms can be flattened by injecting low and high order harmonics appropriately, the linear modulation limit can be extended (Yang et al., 2021; Yeganeh et al., 2020; Yang et al., 2023; Manjesh, & Dabhade, 2019).

Regardless of these developments, systematic comparative studies on particular harmonic injection scenarios in two level seven phase VSIs, particularly, the interaction between DC link utilization, total harmonic distortion (THD), and torque ripple still do not exist. The current seven phase studies are primarily on space vector frames, over modulation area design, or broad principles of generalized modulation, without a specific analysis of the impact of various combinations of injected harmonics on voltage quality and torque related measures (Yang et al., 2021; Casadei et al., 2008; Hamedani, 2020; Yang et al., 2023). Moreover, most harmonic injection studies on multilevel inverters focus on minimization of THD or switching loss optimization instead of the use of DC-link utilization in multiphase motor drives (Yeganeh et al., 2020; Arun et al., 2022).

Driven by these shortcomings, the paper will provide a comparative study of harmonic injection cases of improved DC link exploitation in seven phase VSI fed motor drives. Based on the literature of multiphase and seven phase modulation (Yang et al., 2021; Sultan& Al-Badrani,2024; Hamedani, 2020; Yang et al., 2023; Vujacic et al., 2020; Batkhishig et al., 2025), the paper establishes a generalized reference waveform formulation that accepts selectable amplitudes and phase shifts of low order harmonics, and compares single, dual, and triple harmonic injection schemes by the This offers design oriented information on the compromise between long linear modulation range and the quality of the waveforms and practical information on the selection of harmonic injection strategies based on the requirements of the specific application.

Mathematical Modeling of the Seven-Phase VSI with Harmonic Injection

Seven-Phase Two-Level VSI Model

Each inverter leg in a two-level seven-phase VSI, as shown in (Figure 1), generates a pole voltage with respect to the DC midpoint given by.

$$v_k(t) = (2S_k(t) - 1)\,\frac{V_{dc}}{2}, \tag{1}$$

where Sk(t) ∈ {0,1} is the switching function of phase k, for k = 1,2,...,7.

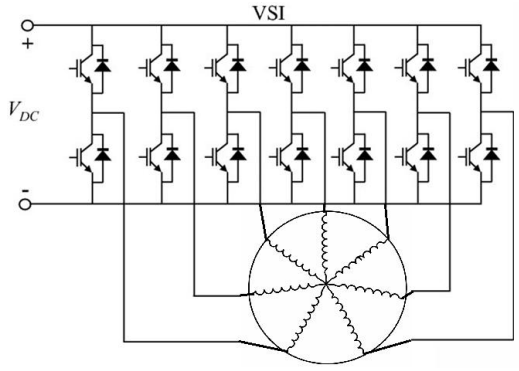

Figure 1. 7-phase VSI drive system

In the case of a balanced seven-phase system with a floating neutral, common-mode voltage may be eliminated to obtain the phase voltage

$$v_{ph,k}(t) = v_k(t) - \frac{1}{7}\sum_{i=1}^{7} v_i(t) \tag{2}$$

The fundamental phase displacement of the neighboring phases is

$$\theta = \frac{2\pi}{7}, \qquad \phi_k = (k-1)\theta. \tag{3}$$

Whereas, the fundamental reference for phase k is

$$v_{1,k(t)} = m_1 \sin(\omega t + \phi_k) \tag{4}$$

where m_1 is the fundamental modulation index and ω is the fundamental angular frequency.

The generalized injected reference waveform is written as:

$$v_{ref,k(t)} = m_1 \sin(\omega t+\phi_k)+a_3 \sin(3\omega t+3\phi_k+\psi_3)+a_5 \sin(5\omega t+5\phi_k+\psi_5)+a_7 \sin(7\omega t) \tag{5}$$

The third and fifth harmonic amplitudes are a3 and a5 with phase shifts ψ3 and ψ5. In seven-phase systems, the seventh harmonic exhibits a common-mode property because

$$7\phi_k = 7(k-1)\frac{2\pi}{7} = 2\pi(k-1) \tag{6}$$

Therefore, it becomes identical across phases and is represented as a common-mode injection term a7 sin(7ωt). On the other hand, a carrier-based PWM is employed using a common triangular carrier vc(t) with crossing with switching frequency fs. The switching function can be expressed as:

$$S_k(t) = \begin{cases} 1, & v_{ref,k}(t) \geq v_c(t) \\ 0, & v_{ref,k}(t) < v_c(t). \end{cases} \tag{7}$$

To keep the modulation in the linear region the following condition should be satisfied:

$$|vref, k(t)| \leq 1 \qquad \forall t, \forall k. \tag{8}$$

Methodology

The current section presents the proposed harmonic injection strategy, the performance indicators adopted for evaluation, and the MATLAB-based simulation framework that is used for validation.

Proposed Harmonic Injection Strategy.

The harmonic injection strategy introduced here in this paper relies on the generalized reference formulation in (5) that allows the systematic investigation of the harmonic injection scenarios in seven-phase systems. The main goal is to increase the use of DC-link voltage utilization and yet achieve reasonable harmonic performance. To achieve the above-mentioned features, the proposed strategy is to minimize the peak value of the modulation reference signal. To demonstrate this strategy let $v_{ref,k}(t)$ denote the unscaled modulation reference of phase k, which includes the fundamental component of amplitude m_1 and the injected harmonic components. The peak magnitude of the reference waveform is determined as:

$$V_{pk} = \max_{\{t,k\}} \left| v_{ref,k}(t) \right| \tag{9}$$

To guarantee linear carrier-based PWM operation, the reference must satisfy $|v_{ref,k}(t)| \leq 1$. So, the maximum permissible fundamental modulation index before over modulation is obtained as follows:

$$m_{1,max} = \frac{m_1}{V_{pk}} \tag{10}$$

This expression shows that reducing V_{pk} through appropriate harmonic injection directly increases $m_{1,max}$, consequently enhancing DC-link voltage utilization.

Performance Indicators

Three performance indicators are used to determine the effects of harmonic injection on the quality of the waveform and the pulsating torque. The phase voltage THD calculated is as below.

$$\text{THD} = \sqrt{\frac{\sum_{n=2}^{\infty} V_n^2}{V_1^2}} \tag{11}$$

V_1 is the fundamental voltage component and V_n is the amplitude of the n^{th} harmonic component. Further, a torque ripple index (TRI) that is defined in terms of voltages is given as:

$$\text{TRI} = \frac{\sum_{h \in \mathcal{H}_T} V_h^2}{V_1^2} \tag{12}$$

where H_T represents collection of low-order harmonic components which are the main contributors to the torque pulsations in multiphase drives. This index is a normalized level of the harmonic content with respect to the torque ripple. It is worth noting that the last indicator is the DC-link utilization factor. In fact, these indicators enable a comprehensive trade-off analysis between DC utilization, harmonic distortion and torque pulsating characteristics.

Investigated Harmonic Injection scenarios

In order to examine the effect of harmonic injection, the following scenarios are considered: (i) SPWM with no injection, (ii) third-harmonic injection, (iii) fifth-harmonic injection, (iv) seventh-harmonic injection, (v) third- and fifth-harmonic injection, (vi) third- and seventh-harmonic injection, (vii) fifth- and seventh-harmonic injection, and (viii) third-, fifth-, and seventh-harmonic injection. There are positive and negative injection polarities of harmonic injection to be taken into account in each scenario. Moreover, the phase variations of ψ_3 and ψ_5 are adjusted to determine which arrangement produces the minimum reference peak while remaining within the linear modulation boundary.

Simulation Model and Implementation

A MATLAB/Simulink model of a two-level inverter of a seven-leg voltage source that ultimately delivers power to a balanced seven-phase load is constructed, as shown in Figure 2, to verify the proposed methodology. The generalized harmonic injection reference of carrier-based SPWM is used to produce the gating signals. It assumes a floating neutral condition, and the common-mode voltage component has been eliminated by (2) to obtain the applied phase voltages. Harmonic parameters all of the parameters of the simulation are kept constant within all the harmonic injection circumstances of interest to compare fairly and consistently. Table 1 reports the key parameters of the simulation.

Table 1. Simulation parameters

Parameter	Value
DC-link voltage Vdc	600 V
Switching frequency fs	5 kHz
Fundamental frequency f1	50 Hz
Time step Ts	1/(80fs)
Simulation duration	Two fundamental cycles

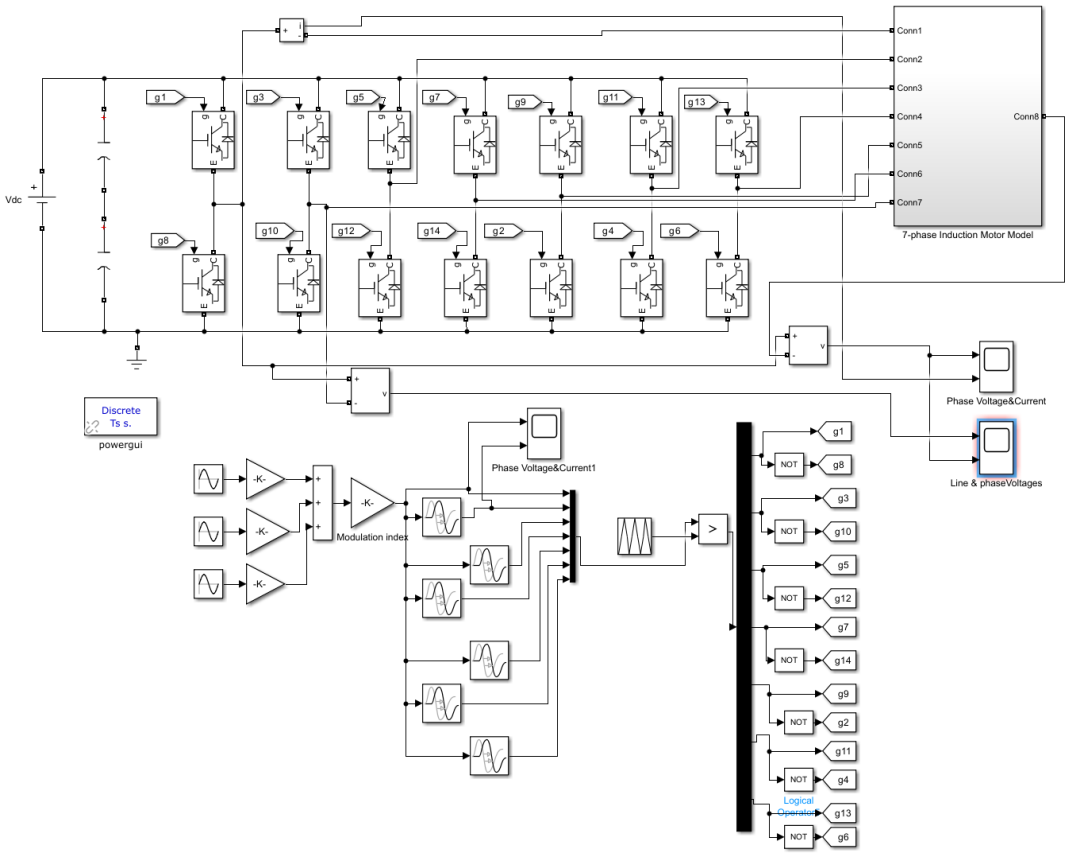

Figure 2. MATLAB simulink model

Results and Discussion

In this section, a detailed analysis of the studied harmonic injection scenarios s in a seven-step carrier based SPWM inverter is provided. The analysis is devoted to the increase in the utilization of DC-link, waveform shaping behavior, harmonic distortion features, and the tendency of the torque ripple. The results obtained are summarized in Table 2 and demonstrated with the help of the time-domain and frequency-domain plots presented in (Figures. 3, 4, and 5). Specifically, (Figure 3) shows reference waveform decomposition for some selected injection scenarios showing the fundamental component, injected harmonics, and the total reference signal within the linear modulation boundary. The harmonic injection distorts the modulation waveform such that it flattens the peak amplitude of the reference signal. The third harmonic has the dominant role in the reduction of the peaks whereas the fifth and seventh harmony will give additional fine tunings to the harmonic based on the phase alignment. The harmonics mutual interaction is easily seen in the joint injection cases where the waveform is more uniformly distributed in the linear modulation boundary.

DC-Link Voltage Utilization Results

The highest permissible fundamental modulation index achieved in each case is given in Table 2. Traditional SPWM that does not inject harmonic gives a baseline value of $m_{1,max} = 1.0$.When the third harmonic is injected, the modulation limit to $m_{1,max} = 1.1547$ along with an approximate improvement of 15.5% in the DC-link usage is reached. The fifth-harmonic injection gives an intermediate improvement ($m_{1,max} = 1.0515$), and the seventh-harmonic injection alone gives a minor improvement ($m_{1,max} = 1.0257$), as is expected of a common-mode signal in seven-phase systems. Each of the harmonics is maximally enhanced by combining several harmonics. The combination of harmonic frequencies three and five results in the $m_{1,max} = 1.2071$ and the combination of harmonic frequencies three and seven results in the $m_{1,max} = 1.1708$. Good DC-Link Voltage utilization is achieved by injecting all three harmonics at the same time so that $m_{1,max} = 1.2311$ is obtained which is an improvement of utilization of about 23 percent of the conventional SPWM.

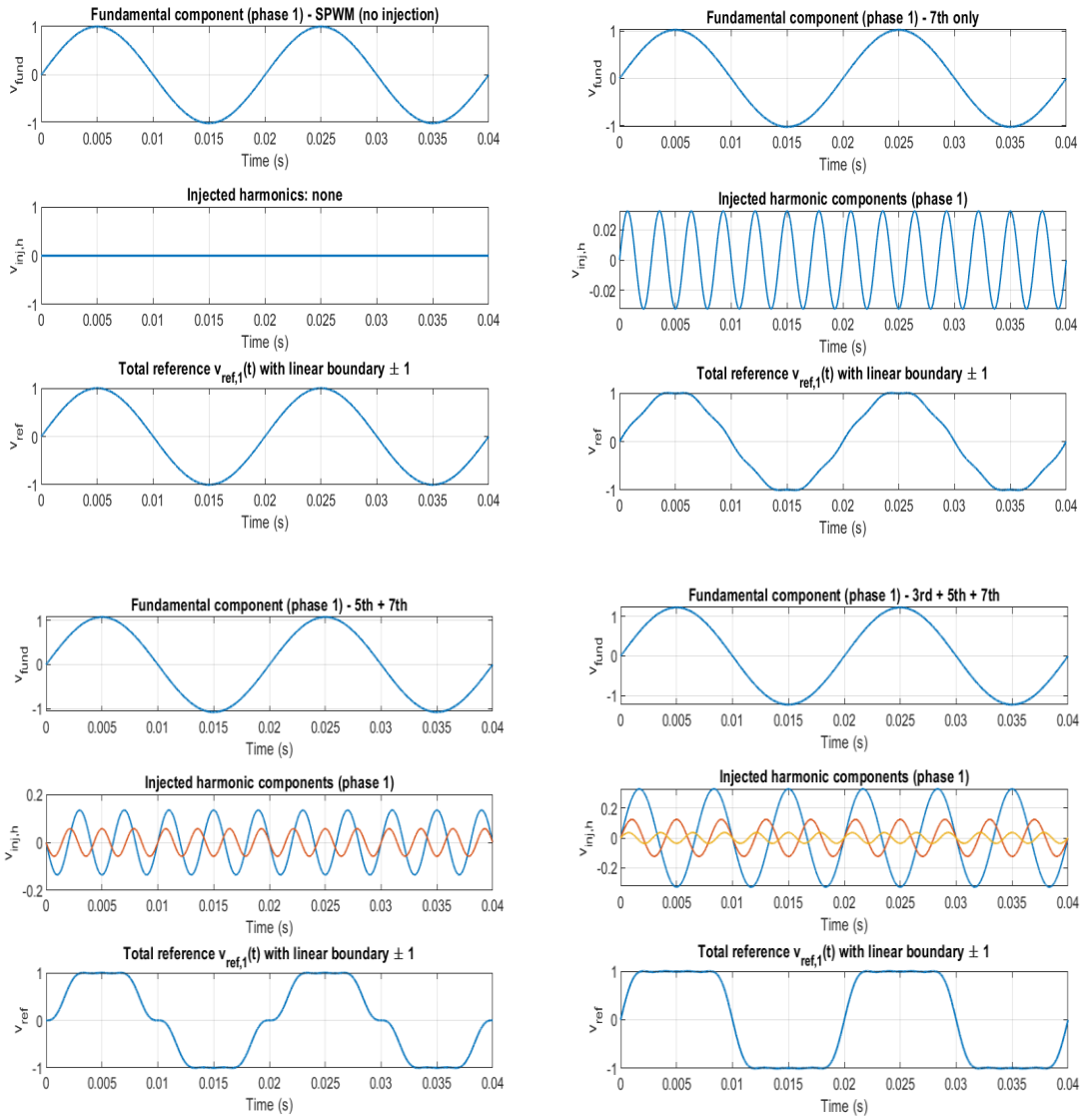

Figure 3. Reference waveform decomposition for selected injection scenarios

Table 2. Summary of optimal harmonic injection results for all investigated scenarios

Scenario	$m1$,max	$v$peak	THD$_{ph}$ (%)	TRI$_{ph}$	TRI$_{ll}$	a_3	a_5	a_7
SPWM (no injection)	1.00	1.00	1.6269	0.00011	0.00034	–	–	–
3$_{rd}$ only	1.1547	1.00	16.748	0.02798	0.14059	0.19243	–	–
5th only	1.0515	1.00	6.4415	0.00404	0.014222	–	-0.06503	–
7th only	1.0257	1.00	1.4946	0.00012	0.00055	–	–	0.032
3rd + 5th	1.2071	1.00	24.532	0.06011	0.29598	-0.28038	-0.07328	–
3rd + 7th	1.1708	1.00	17.320	0.02994	0.14881	0.19196	–	-0.02
5th + 7th	1.0774	1.00	12.570	0.01567	0.05103	–	-0.13488	-0.05
3rd + 5th + 7th	1.2311	1.00	28.988	0.08397	0.40570	0.32658	0.12317	0.035

Phase and Line Voltage Waveforms

The phase and line voltage waveforms of each injection case are depicted in (Figure. 4). As illustrated in this figure, harmonic injection enhances the importance of the modulation depth of the phase voltages whilst sustaining the switching properties of carrier-based SPWM. The waveform envelopes depict better DC-link exploitation, especially in the cases of multi-harmonic injections. Nonetheless, greater oscillatory behavior is recorded in cases of strong harmonic injection implying increased harmonic distortion levels.

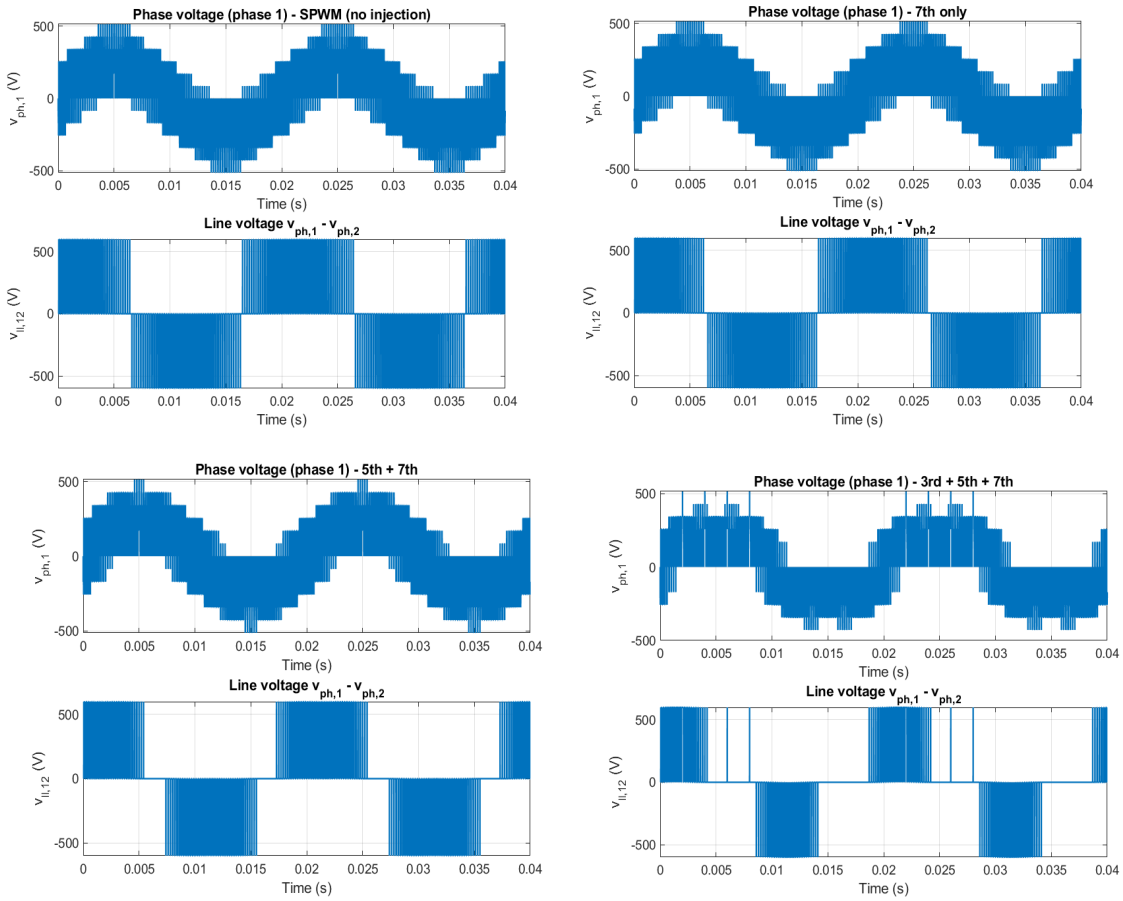

Figure 4. Phase and line voltages using different harmonic injection scenarios

Frequency-Domain Analysis

The FFT spectra of the phase and line voltages are presented in (Figure 5). The content of the harmonic in the baseline SPWM case is very low, which validates the high quality of the waveforms of the traditional sinusoidal modulation. Conversely, in cases of harmonic injection, the harmonic components of lower order are strong with respect to the injected frequencies. As can be clearly seen in the FFT results, the increase in the utilization of DC-link is done at the cost of a greater harmonic distortion. İt is also worth to mention that in seven-phase systems, the peak magnitude of the line voltage is inherently lower than that of the phase voltage, not like conventional three-phase systems, due to the reduced phase displacement between adjacent phases.

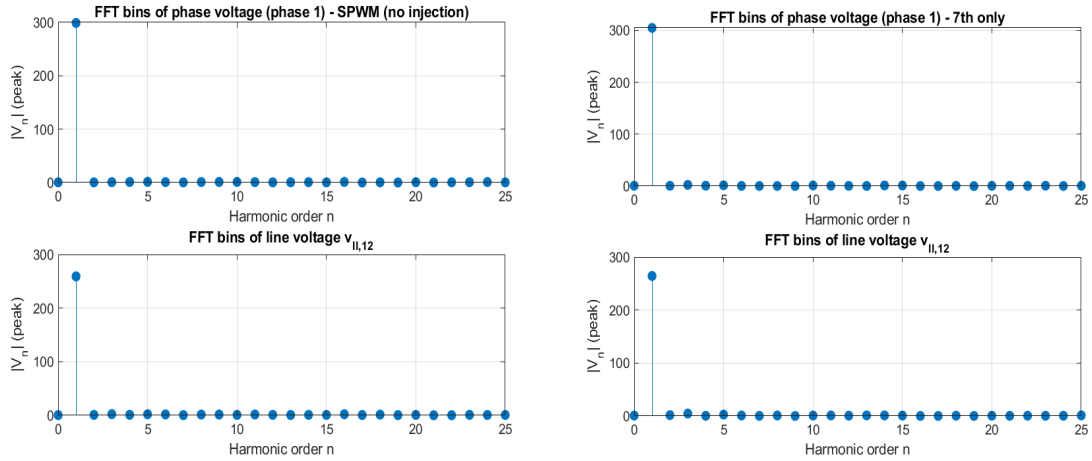

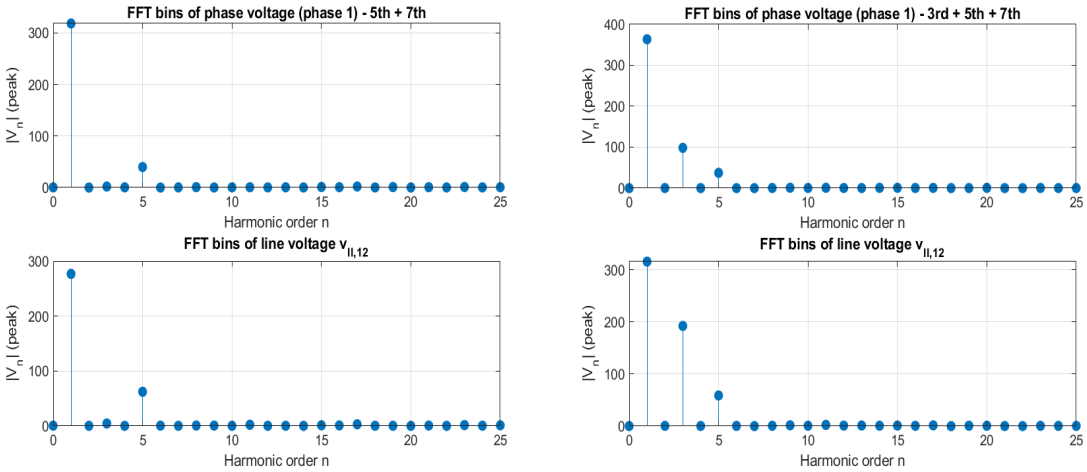

Figure 5. FFT spectra of the phase and line voltages for selective harmonic injection scenarios

Torque Ripple Tendency

The voltage-based torque ripple index (TRI) further contributes to the knowledge of the impact of harmonic injection on drive performance. As can be seen in Table 2, the baseline SPWM condition has extremely low values of TRI, which implies that it only has a low propensity of torque pulsation. The addition of third harmonic injection would add a lot to the TRI due to the existence of harmonic components of low order. Multi-harmonic injection cases produce maximum TRI, particularly of line voltages which are higher orders of oscillatory energy which can be transformed into pulsating torques in a practical multi-phase machine. Conversely, the fifth-harmonic injection produces moderately large TRI values, and the seventh-harmonic injection produces minor alteration in the torque ripple since it is a common-mode interference. but this fact is all the more notable when it comes to specially constructed seven-phase machines whose winding configuration and harmonic subspace can be deliberately optimized to take advantage of harmonic injections of special choice (e.g. 3rd, 5th, or both) to increase torque density, widen voltage range, and to allow fault-tolerant operation without excessive torque pulsations. Harmonic injection is, therefore, not just a modulation enhancement, it is also a co-design parameter between the inverter and a seven-phase machine purpose-designed.

Conclusion

The paper examined the behavior of a seven-phase voltage source inverter under varied modulation conditions, such as traditional SPWM and the harmonic injection methods. It was revealed that harmonic injection affects the voltage exploitation, harmonic spectrum and torque ripple inclination of multiphase drive systems significantly. The reference SPWM was stable and had a low torque ripple tendency, but limited use of DC-link voltage. Voltage capability was improved by introducing low order harmonic components, especially third-harmonic injection, but the tendency to torque ripple was increased by the existence of the main harmonic components interacting with machine electromagnetic fields. Multi-harmonic injection generated the greatest levels of oscillatory energy, which means it can have negative implications on the torque smoothness and the performance of the drives. Fifth-harmonic injection, in contrast, provided a moderate compromise between the use of voltages and torque ripple, and seventh-harmonic injection had little effect on the pulsation of the torque, as it acts predominantly as a common-mode factor in seven-phase machine. This observation is true to the fact that it is possible to make good use of higher-order harmonic injection to improve the performance of modulation without making the quality of torque substantially worse. In general, the paper proves that the harmonic injection is not only a modulation increase method but is a design oriented tool that can be customized to suit a given seven-phase machine design. With suitable winding layouts, and electromagnetic design, the harmonic components chosen can enhance the use of DC-link, greater range of operating speeds, as well as acceptable smoothness of torque. It allows harmonic-assisted modulation to be very applicable to high-end multiphase drive applications e.g. electric vehicles, aerospace actuators, and fault-tolerant industrial systems.

Recommendations

Based on the findings of this study, when better DC-link voltage utilization is needed for seven-phase inverters, harmonic-injected SPWM is advised, but careful component injection selection is crucial. Fifth-harmonic injection provides a workable compromise between voltage enhancement and torque quality. Seventh-harmonic injection is better when modulation improvement is required with little torque pulsation, and third-harmonic injection should be used with caution because of its effect on torque ripple. It is not advised to use excessive multi-harmonic injection, and the modulation strategy chosen should be in line with the drive's operational priority and the electromagnetic properties of the seven-phase machine.

Scientific Ethics Declaration

* The authors declare that the scientific ethical and legal responsibility of this article published in EPSTEM journal belongs to the authors.

Conflict of Interest

* The authors declare that they have no conflicts of interest.

Funding

* The authors received no financial support for the research of this article.

Acknowledgements or Notes

* This article was presented as an oral presentation at the International Conference on Technology (www.icontechno.net) held in Budapest/Hungary on February 05-08, 2026.

* The authors would like to express their sincere gratitude to the University of Mosul and the University of Fallujah for their continuous support and for providing the necessary facilities and resources that contributed to the completion of this research.

References

Ameen, Y. M. Y., Fadheel, B. A., & Mahdi, A. J. (2020). Third harmonic injection PWM technique for maximizing DC-BUS utilization of five-phase VSIs. *Indonesian Journal of Electrical Engineering and Computer Science, 17*(3), 1607–1617.

Sultan, A. H., & Al-Badrani, H. (2023). Modeling and simulation of a seven-phase induction motor. *2023 International Conference on Engineering, Science and Advanced Technology (ICESAT)*, 177–181..

Casadei, D., Dujic, D., Levi, E., Serra, G., Tani, A., & Zarri, L. (2008). General modulation strategy for seven-phase inverters with independent control of multiple voltage space vectors. *IEEE Transactions on Industrial Electronics, 55*(5), 1921–1932.

Hamedani, P. (2020). Harmonic evaluation of seven-phase VSI with PWM switching technique. *2020 11th Power Electronics, Drive Systems, and Technologies Conference (PEDSTC)*, 1–6.

Yang, G., Yang, J., Li, S., Wang, Y., Hussain, H., Yan, L., & Deng, R. (2021). Overmodulation strategy for seven-phase induction motors with optimum harmonic voltage injection based on sequential optimization scheme. *IEEE Transactions on Power Electronics, 36*(12), 14039–14050.

Yang, G., Li, S., Hussain, H., Bai, Z., & Yang, J. (2023). Establishing optimized harmonic injection order of sequential overmodulation strategies for seven-phase induction motors. *IEEE Transactions on Energy Conversion*, *38*(1), 739–742.

Batkhishig, B., Gonçalves, P. F. d. C., Pietrini, G., Nahid-Mobarakeh, B., & Emadi, A. (2025). PWM techniques for two-level voltage source inverters: A comparative study. *IEEE Access*, *13*, 86235–86255.

Yeganeh, M., Sarvi, M., Blaabjerg, F., & Davari, P. (2020). Improved harmonic injection pulse-width modulation variable frequency triangular carrier scheme for multilevel inverters. *IET Power Electronics*, *13*(14), 3146–3154.

Manjesh, & Dabhade, N. S. (2019). Reduction of total harmonic distortion in nine phase induction motor drive with third harmonic injection pulse width modulation technique. *International Journal of Recent Technology and Engineering*, *8*(4), 10177-10181.

Arun, V., Kumar, N., & Prabaharan, N. (2022). A hybrid reference pulse width modulation technique for binary source multilevel inverter. *International Journal of Power Electronics and Drive Systems (IJPEDS)*, *13*(2), 980–987.

Sultan, A. H., & Al-Badrani, H. (2024). Field oriented control for seven phase induction machine with comparative control method. *2024 12th International Conference on Smart Grid (icSmartGrid)*, 844–849.

Vujacic, M., Dordevic, O., & Grandi, G. (2020). Evaluation of DC-link voltage switching ripple in multiphase PWM voltage source inverters. *IEEE Transactions on Power Electronics*, *35*(4), 3478–3490.

.

Author(s) Information

Yasir M.Y. Ameen
University of Mosul, Mosul, Iraq
ORCID iD: 0000-0002-2878-8165
* Contact e- mail : yasir_752000@uomosul.edu.iq

Marwan H. Mohammed
University of Mosul, Mosul, Iraq
ORCID iD: 0009-0001-3208-8671

Marwan M. Alwan
University of Fallujah, Anbar, Iraq
ORCID iD:0009-0005-6489-1388

*Corresponding authors contact email

To cite this article:

Ameen, Y.M.Y., Mohammed, M. H., & Alwan, M. M. (2026). Harmonic injection scenarios for enhanced DC-link utilization in seven-phase VSI-fed motor drives. *The Eurasia Proceedings of Science, Technology, Engineering and Mathematics (EPSTEM), 39,* 40-49.

The Eurasia Proceedings of Science, Technology, Engineering and Mathematics (EPSTEM)
ISSN: 2602-3199

The Eurasia Proceedings of Science, Technology, Engineering and Mathematics (EPSTEM), 2026

Volume 39, Pages 50-56

IConTech 2026: International Conference on Technology

Assessment of the Hydrodynamic Motions of a Floating Dock After Modernization

Yordan Denev
Technical University of Varna

Abstract: The article examines the hydrodynamic motions of a modernized floating dock. In the context of modernization, this consists of extending the dock structure without changes to its cross-section, structural configuration, structural elements, or their geometric characteristics. The modernization aims to increase the dock's load-carrying capacity, which affects its operational performance and is an important aspect of the ship-docking process. Two of the six degrees of freedom of the floating body—sway (lateral motion) and pitch (longitudinal rocking)—are evaluated and analyzed. These two motions, representing the corresponding degrees of freedom during dock operation, are assessed both before and after the modification. An analysis is carried out to determine the extent of the changes and whether they have a direct impact on the operational performance of the structure. The results indicate that after the modification, there is a change in the hydrodynamic characteristics of the dock, more specifically in the roll and pitch motions.

Keywords: Floating dock, Motions, Hydrodynamic, Modernization

Introduction

Floating docks are an important facility in ship docking within the shipbuilding and ship repair industry. They are characterized by their main dimensions and lifting capacity. These two characteristics are of crucial importance, as they determine the productivity and competitiveness of shipbuilding and ship repair enterprises. One way to increase the lifting capacity of a dock is by extending its length. For existing dock facilities, this is achieved through preliminary strength analyses related to the structural capability to withstand the additional loads. The extension, which represents a form of modernization, also affects the operational characteristics of the facility. For this reason, an evaluation and analysis of this effect is required.

To evaluate the behavior of the dock during operation, a quasi-static model has been developed. Using this model, the dynamic behavior of the dock during ship docking and launching operations has been simulated. Various loading cases were tested during the operation of the dock using the model. In the development of the model, the dock was considered as a rigid body with six degrees of freedom, including hydrostatic and hydrodynamic forces, as well as forces resulting from mooring ropes and the interaction between the ship and the dock. The model successfully controls the transverse and longitudinal motions of the dock during operation. This is achieved through the use of an automatic ballast control system (Wen, 2026).

The modernization of floating docks is carried out not only with the aim of increasing lifting capacity, but also to improve the operational performance of the facility. The conversion from a single-pontoon to a multi-pontoon dock structure is analyzed in Wahidi (2022). Using the Finite Element Method, the structure is analyzed and it is established that the stresses obtained after the conversion are lower than the allowable limits. The lifting capacity remains unchanged, while the draft increases and the freeboard height also increase. Ultimately, modernization leads to savings in operational costs, which can be used as an investment.

An analysis of the hydrodynamic characteristics of a floating dock, taking into account the connections between its individual sections and the location of its operation, was carried out in Fu (2023). The performed analysis

clearly shows that under transverse and oblique wave conditions, the configuration with transverse pontoons behaves better compared to the configuration with longitudinal pontoons. This has a direct influence on the roll motion of the dock, with the roll amplitude being reduced by 14%.

Stability is of major importance from the operational point of view of a floating dock. It is evaluated under different operating conditions of the structure and is closely related to its hydrodynamic characteristics. In this context, a model based on differential equations has been developed in order to assess the motion of the dock under various scenarios, including emergency conditions. The angular velocity of listing can be used as a design parameter characterizing the operational stability of the dock. In addition, significant listing may occur under the action of ballast (Drobyshevskiy, 2001).

Two methods for determining the responses of a floating dock are proposed in (Zhang, 2025), namely static and dynamic. The static method is based on the equilibrium equations of a floating body, solved using the Newton–Raphson method. The dynamic method includes the six degrees of freedom and models of hydrodynamic and hydrostatic forces.

A model incorporating the six degrees of freedom of a floating dock was developed to evaluate its dynamic responses under accident conditions. Using this model, it was found that the maximum roll angles during an accident caused by intensive corrosion are 0.18° and 0.69° in the case of a single hole. When two holes are present, the roll and pitch angles increase to 0.42° and 2.04°, respectively (Zahi, 2023). These values are part of the dock's dynamic behavior and must be controlled, as there is a risk of the dock capsizing and causing an environmental disaster.

The statistical and dynamic responses, expressed in terms of significant motion and acceleration amplitudes, were evaluated against short-term seakeeping criteria to prevent flooding of the dock pontoon deck using a developed algorithm. In applying the algorithm, it was assumed that the dock is operating in irregular waves. The study results define the limit navigation conditions for safe operation during the relocation of a small-size floating dock (Burlacu, 2018).

Hydrodynamic Model of the Floating Dock

The hydrodynamic state of a floating dock depends on its shape, dimensions, and loading. The hydrodynamic forces acting on the floating dock include only the forces due to added mass, added moment of inertia, and damping forces. By its nature, this is a complex process that combines the six degrees of freedom of a rigid body. In a simplified form, it can be represented by the following equation.

$$D= [x\ y\ z\ \phi\ \theta\ \psi]^T \quad (1)$$

where:
- X y z- surge, sway, and heave movements;
- $\phi\ \theta\ \psi$- roll, pitch, and yaw movements;

The six degrees of freedom are shown in fig. 1

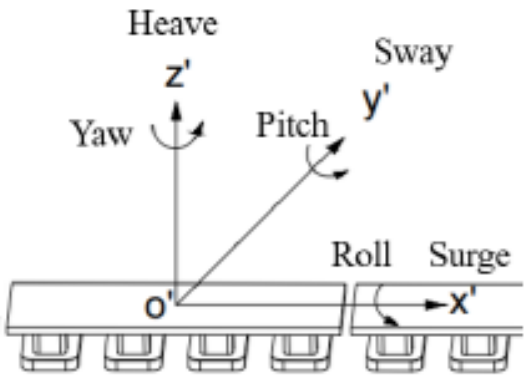

Figure 1. Floating dock six degrees of freedom

The complete equation describing the six degrees of freedom of the floating dock as a rigid body is as follows

$$(m+m_a)\frac{d^2X_G}{dt^2}=F_s+F_d+F_c \tag{2}$$

Where:
- m, ma- mass and added masses;
- X_G- center of gravity;
- t- time;
- Fs- hydrostatic force;
- Fd- hydrodynamic force;
- Fc- contact force.

The motion of the ship in the steadily translating coordinate system O(x,y,z)O(x, y, z)O(x,y,z) is described by three translational movements of the ship's center of gravity along the x-, y-, and z-axes. All of the motions are evaluated by following the equations.

$$\text{Surge} \quad : \quad x = x_a \cos(\omega_e t + \varepsilon_{x\zeta}) \tag{3}$$

$$\text{Sway} \quad : \quad y = y_a \cos(\omega_e t + \varepsilon_{y\zeta}) \tag{4}$$

$$\text{Heave} \quad : \quad z = z_a \cos(\omega_e t + \varepsilon_{z\zeta}) \tag{5}$$

$$\text{Roll} \quad : \quad \phi = \phi_a \cos(\omega_e t + \varepsilon_{\phi\zeta}) \tag{6}$$

$$\text{Pitch} \quad : \quad \theta = \theta_a \cos(\omega_e t + \varepsilon_{\theta\zeta}) \tag{7}$$

$$\text{Yaw} \quad : \quad \psi = \psi_a \cos(\omega_e t + \varepsilon_{\psi\zeta}) \tag{8}$$

If the motions of the ship's center of gravity (G), calculation the motions at any other point of the structure can be evaluated using the principle of superposition. The phase shifts of these motions are related to the height of the harmonic wave at the origin of the steadily moving system (O(x, y, z)) – which is the average position of the ship's center of gravity, even though no actual wave can be measured there.

$$\zeta = \zeta_a \cos(\omega_e t) \tag{9}$$

The harmonic velocities and accelerations in the steadily moving O(x, y, z) coordinate system can be determined by differentiating the displacements. This process will be demonstrated here using roll as an example for three conditions.

Displacement

$$\phi = \phi_a \cos(\omega_e t + \varepsilon_{\phi\zeta}) \tag{10}$$

Velocity

$$\dot{\phi} = -\omega_e \phi_a \sin(\omega_e t + \varepsilon_{\phi\zeta}) \; = \omega_e \phi_a \cos(\omega_e t + \varepsilon_{\phi\zeta} + \pi/2) \tag{11}$$

Acceleration

$$\ddot{\phi} = -\omega_e^2 \phi_a \cos(\omega_e t + \varepsilon_{\phi\zeta}) = \omega_e^2 \phi_a \cos(\omega_e t + \varepsilon_{\phi\zeta} + \pi) \tag{12}$$

In addition to the six motions of the floating dock, its stability is also important. It is regulated by the rules of classification societies, and unlike that of merchant fleet vessels, the stability of floating docks has a minimum value of 1.0 m (Korean register of shipping, 2015).

Floating Dock Geometry and Main Dimensions

The geometry of the dock is simple compared to that of ships. It consists of a pontoon and two side towers, intended for ballast during the submerging and surfacing of the dock in its various loading conditions. A schematic of the dock is shown in fig.

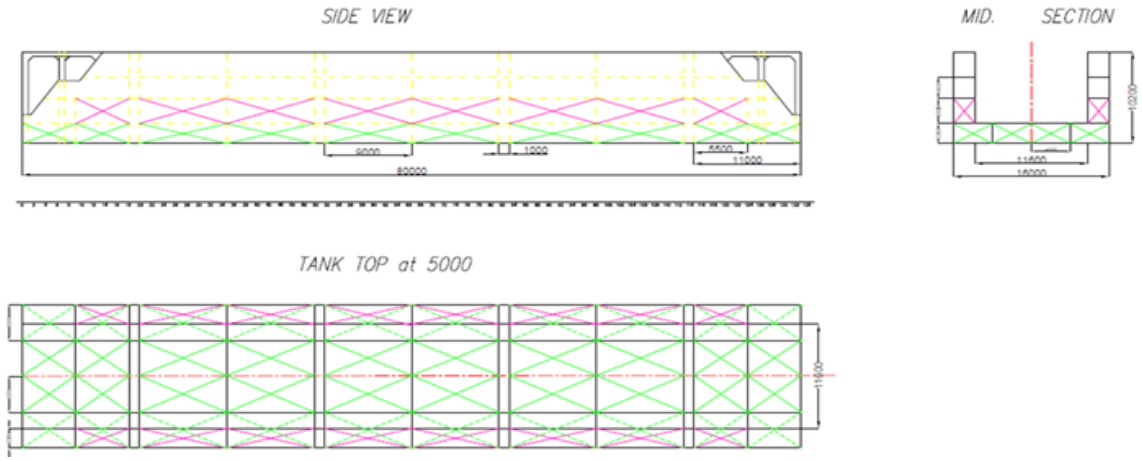

Figure 2. Floating dock arrangement

The dimensions of the dock before and after the modernization (extension) are presented in Table 1 and Table 2.

Table 1. Dock dimension before modernization

Item	Dimension
Length, m	80.00
Breadth, m	16.00
Depth, m	10.20
Draught, m	7.40
Lifting capacity, t	2000

Table 2. Dock dimension after modernization

Item	Dimension
Length, m	90.00
Breadth, m	16.00
Depth, m	10.20
Draught, m	7.40
Lifting capacity, t	2250

Using the hydrodynamic model and the dimensions of the floating dock before and after modernization, an assessment was made of all six degrees of freedom.

Hydrodynamic Motions Assessment

The assessment of the hydrodynamic motions of the dock was carried out using specialized software of the classification society Bureau Veritas. Through the software, the transverse cross-section of the dock is modeled by defining its main characteristic dimensions, topology, type of construction material, and loading. The assessment of four motions—two translational and two rotational—of the floating dock before modernization is presented in Table 3. The values shown were calculated at full draft of the dock, i.e., submerged with cargo on board. This is the main operating condition of the dock, in which it must withstand all applied static and dynamic forces.

Table 3. Motions of dock with L= 80,0m

Item	Value
Surge, m/s^2	0.50
Sway, m/s^2	1.586
Heave, m/s^2	2.047
Yaw, rad/s^2	0.040

Particular attention was paid to two of the six degrees of freedom—roll motion and pitch. These two degrees of freedom have a direct influence on the dock's behavior during docking and launching of ships. The results regarding amplitude, period, and accelerations in both cases are presented in Tables 3.1 and 3.2.

Table 3.1. Rolling motions

Roll	
Item	Value
Amplitude, rad	0.209
Period, s	11.641
Acceleration, rad/s^2	0.061

Table 3.2. Pitch motions

Pitch	
Item	Value
Amplitude, rad	0.057
Period, s	5.143
Acceleration, rad/s^2	0.085

The results of the hydrodynamic motions of the dock after modernization are presented in Table 4, and for the two motions—roll and longitudinal translation, along with their amplitude, period, and acceleration—in Tables 4.1 and 4.2

Table 4. Motions of dock with L= 90,0m

Item	Value
Surge, m/s^2	0.50
Sway, m/s^2	1.510
Heave, m/s^2	1.949
Yaw, rad/s^2	0.034

Table 4.1. Roll motions

Roll	
Item	Value
Amplitude, rad	0.199
Period, s	11.641
Acceleration, rad/s^2	0.058

Table 4.2. Pitch motions

Pitch	
Item	Value
Amplitude, rad	0.055
Period, s	5.455
Acceleration, rad/s^2	0.072

The modernization of the dock, aimed at increasing its load-carrying capacity without changes to the structure and structural elements, has a favorable effect on its hydrodynamic motions. A noticeable change is observed in the vertical and lateral motions, while the change in rotation about the Z-axis is insignificant. The surge remains unchanged, as it is not directly related to the modernization.

Conclusion

In the article, the hydrodynamic motions of a floating dock after modernization are investigated. The modernization consists of extending the dock without altering its structural design. From an operational point of view, the six degrees of freedom are analyzed. Particular attention is paid to roll and pitch motions. After the extension by approximately 10 m, changes are observed in all motions of the dock.

For a large part of them, a reduction in the values is noted, while for others an increase is observed.The reduction in the values after the extension is approximately 5% for sway and heave. A significant decrease in the values is observed for yaw, of about 17%. After a detailed analysis of the two motions, roll and pitch, and the evaluation of amplitude, period, and acceleration, it was observed that for both motions the amplitude and acceleration decrease by approximately 3–10%. There is no change in the roll period, while for pitch an increase of about 6% is observed. A significant reduction in pitch accelerations of approximately 18% is also noted.

Scientific Ethics Declaration

* The authors declare that the scientific ethical and legal responsibility of this article published in EPSTEM journal belongs to the authors.

Conflict of Interest

* The authors declare that there is no conflict of interest.

Funding

* This research received no specific grant from any funding agency in the public, commercial, or not-for-profit sectors.

Acknowledgements or Notes

* This article was presented as an oral presentation at the International Conference on Technology (www.icontechno.net) held in Budapest/Hungary on February 05-08, 2026.

* The author thanks the conference scientific committee and the reviewers for their feedback.

* The author thanks the Technical University of Varna

References

Burlacu, E., & Domnisoru, L. (2018). Dynamic response investigation of a small size floating dock unit in irregular oblique waves. *IOP Conference Series: Materials Science and Engineering* (ModTech 2018).

Drobyshevskiy, Y. (2001). On the operational stability of a floating dock. In *Proceedings of the Seventh International Conference on the Stability of Ships and Ocean Vehicles* (pp. 937–951).

Fu, R., Guo, J., Wu, R., & Liu, H. (2023). Design and hydrodynamic performance analysis of offshore multi-module floating docks. In *Journal of Physics: Conference Series* (HEEPS 2023). IOP Publishing.

Korean Register of Shipping. (2015). *Rules for the classification of floating docks*. https://www.boatdesign.net/attachments/res7-eng-pdf.41134/

Wahidi, S., Pribadi, T. R., Firdausi, M., & Santosa, B. (2022). Technical and economic analysis of a conversion on a single pontoon to a multi pontoon floating dock. *NAŠE MORE: Znanstveni Časopis Za More i Pomorstvo, 69*(2), 114-122

Wen, X., Nordas, K., & Ong, M. (2026). An efficient quasi-static model for simulating floating dock operations. *Ocean Engineering, 347*, 123967.

Zahi, T., Wen, X., & Ong, M. (2023). Dynamic response of a floating dock under corrosion-induced accidents. In *IOP Conference Series: Materials Science and Engineering*

Zhang, J., Wen, H., Kniat, A., & Ong, M. C. (2025). A comparative analysis of numerically simulated and experimentally measured static responses of a floating dock. *Ships and Offshore Structures, 20*(3), 329–346.

Author(s) Information

Yordan Denev
Technical University of Varna, Studentska 1 str., Bulgaria
ORCID iD: 0000-0001-7124-1600
*Contact e-mail: *y.denev@tu-varna.bg*

*Corresponding authors contact email

To cite this article:

Denev, Y. (2026). Assessment of the hydrodynamic motions of a floating dock after modernization, *The Eurasia Proceedings of Science, Technology, Engineering and Mathematics (EPSTEM), 39,* 50-56.

The Eurasia Proceedings of Science, Technology, Engineering and Mathematics (EPSTEM)
ISSN: 2602-3199

The Eurasia Proceedings of Science, Technology, Engineering and Mathematics (EPSTEM), 2026

Volume 39, Pages 57-71

IConTech 2026: International Conference on Technology

Prediction of Accidents Using Artificial Neural Networks in North Cyprus

Hillary Makonise
Near East University

Mustafa Alas
Near East University

Abstract: When compared to global traffic catastrophes, North Cyprus road system ranks among the safest up to the current fiscal quarter of 2025. Considering an approximate estimate of about 1.3 million deaths and millions of non-fatal injuries which are caused by road accidents each year, making them a serious public health concern, it is challenging to anticipate and avoid traffic accidents on new road segments due to a multitude of subjective and objective factors. With minimal data sets at disposal, artificial neural networks (ANN) have proven to be successful in forecasting traffic accidents. Therefore, it is crucial to properly evaluate the pertinent hazards. A methodology for creating an accident risk prediction model that can be utilized as a tool for infrastructure management decision-making is presented in this study. These models use easily determined objective factors, such as road length, terrain type, road width, average daily traffic volume, and speed limit The approach makes it possible to handle the supplied data appropriately, looks at how it can be utilized to create models using artificial neural networks (ANNs), and establishes a methodical ANN optimization procedure to find the best ANN model architecture. The approach is applied using accident count data as a result, it is essential to accurately assess the relevant risks. This paper presents an approach for developing an accident risk prediction model that can be used as a tool for infrastructure management decision-making. The method offers a systematic ANN optimization process to determine the optimal ANN model architecture, making it feasible to handle the provided data effectively, and examines how it may be used to develop models using artificial neural networks (ANNs). The method is used with data on the number of accidents on North Cyprus road.

Keywords: Artificial neural network, Traffic accident, Infrastructure planning

Introduction

One of the main causes of death globally is traffic accidents, approximately 50 million people sustain non-fatal injuries and nearly 1.19 million people die in traffic accidents, according to the World Health Organization (WHO, 2025). Road traffic crashes are the primary cause of death for poplars of moderate age (WHO,2025). The significant issue is that 93% of deaths occur in developing nations with low and moderate incomes (WHO,2025). In addition to causing human suffering, traffic accidents have a substantial economic impact, costing nations up to 3% of their GDP (WHO). Numerous factors can be linked to the frequency of traffic accidents. While some of these characteristics are quantitative, such as road volume (annual average daily traffic Algorithms 2024), others are subjective, like driver knowledge, training level, experience, the impact of drinking, drugs. Road geometry (curvature, slopes, lane width, shoulder width), road type (freeway or two-lane road), road conditions (pavement quality and potential pavement surface damage), weather (wind, ice, snow, rain), vehicle maintenance, speed limits, frequency of police checks. Increased traffic volume on nearly all highways' results from an increase in the number of vehicles on the road, which raises the likelihood of vehicle collisions. However, the type of road, road geometry, and AADT (which will probably rise in the future) are acknowledged as objective characteristics that are difficult to modify in the future (Federal Highway Administration). Despite the fact that accidents are random and unpredictable at micro-level, statistical models can predict reliable es times of expected accidents by relating aggregates of accidents to various explanatory

- Selection and peer-review under responsibility of the Organizing Committee of the Conference

measures of flow, site characteristics, and road geometry at macro-level. There are other variables that can be altered, such as the ability to repair pavement, the daily fluctuations in the weather, the improvement of car upkeep through regular inspections, the ability to modify speed restrictions, etc. Many scientific fields make substantial use of traditional machine learning models, including artificial neural networks (ANN), random forest regression (RFR), support vector machines (SVM), extreme learning machines (ELM), K-nearest neighbors (KNN), and decision trees (DT). Based on statistical learning theory, the SVM is a popular discriminant method that is well regarded for its capacity for generalization. By investigating the balance between the model's complexity and the training error, the ideal network is found (Vapnik, 1995; Cortes & Vapnik, 1995). By creating the input weights and biases of the hidden layers at random, the ELM creates a single-layer feedforward network (Huang et al., 2006). A wide range of cutting-edge machine learning methods, including ensemble learning models like XGBoost , LightGBM , and CatBoost, are appropriate for sequence data. The benefits of the XGBoost model are particularly evident in its excellent prediction accuracy and interpretability (Chen & Guestrin, 2016; Ke et al., 2017; Prokhorenkova et al., 2018).

Large data sets and GPU training are made possible by the LightGBM model. It has been demonstrated that the LightGBM models outperform XGBoost in terms of accuracy and speed. Additionally, the integration of gradient boosting-based category features enabled by the CatBoost algorithm indicates that data fusion allows for greater forecasting accuracy (Ke et al., 2017, Ke et al., 2017; Chen & Guestrin, 2016). In recent years, the use of artificial neural networks (ANN) has demonstrated its viability by forecasting and displaying desirable outcomes despite small data sets (Jain et al., 2015, Zhang et al., 2025, Li et al., 2024). For the enhancement of traffic safety management, the accuracy and outcomes of traffic accident prediction models are crucial.

The results show that the most significant factors which increase traffic accidents on urban roads are highway width, head-on collisions, the type of vehicle at fault, ignoring lateral clearance, following distance, inability to control the vehicle, over speeding, and driver deviation to the left. This study offers artificial neural network (ANN) model for evaluating traffic accidents on state roads in KKTC.

Objectives

i. To develop an artificial neural network (ANN) based predictive model capable of accurately forecasting accident occurrence using historical accident, traffic, environmental, and roadway data.
ii. To identify and quantify the most influential factors contributing to accidents by analyzing input features (e.g., traffic volume, weather conditions, road geometry, human factors) within the ANN framework.
iii. To evaluate and compare the performance of different ANN architectures and training algorithms in terms of prediction accuracy, robustness, and generalization capability.
iv. To validate the proposed ANN model using real-world datasets and benchmark its performance against traditional statistical and machine-learning accident prediction methods.
v. To demonstrate the practical applicability of the proposed prediction model for proactive accident prevention, decision support, and traffic safety planning by transportation authorities

Research Questions

1. How accurately can an artificial neural network predict traffic accident occurrence in North Cyprus based on historical accident data?
2. Which factors (e.g., time of day, weather conditions, road type, traffic volume, driver demographics) contribute most significantly to accident prediction when using an ANN?
3. How does the performance of an artificial neural network compare with traditional statistical models (e.g., logistic regression) for predicting traffic accidents in North Cyprus?
4. Can an ANN effectively identify high-risk locations and time periods for traffic accidents in North Cyprus?
5. How does varying the architecture of the artificial neural network affect accident prediction accuracy?

Hypothesis

H_1 When trained on the same historical accident and traffic datasets, artificial neural network-based models predict accident occurrence and severity with far higher accuracy than conventional statistical and machine-learning models.

H_2 When compared to linear modeling techniques, artificial neural networks greatly enhance accident prediction performance by capturing intricate nonlinear interactions between traffic, environmental, and highway factors.

Literature Review

Numerous studies globally have focused on predicting traffic accidents and comprehending the factors which compromises traffic safety. These studies have investigated the inter-connectivity of variables using a variety of methods and methodologies (Lord & Mannering, 2010; Mannering & Bhat, 2014). Chapter 10 of the Highway Safety Manual specifically discusses the prediction model for rural two-lane, two-way highways, highlighting the influence of traffic volume (AADT) via project geometry and safety performance functions (SPF) and crash modification factors (American Association of State Highway and Transportation Officials (AASHTO, 2010).
In a bid to examine the geometric features leading to accidents, Bared and Vogt (1999) investigated Minnesota and Washington, two lane roads both urban and rural set ups, aiming to find the parameters that has the biggest impact on the frequency of traffic accidents. Despite being restricted to two-lane roads, Persaud presented one of the first studies for performing independent evaluations for curves and tan gents. The reliant Road geometry and traffic flow were the independent variables, and crash frequency was the dependent variable. Generalized linear modeling was used to calibrate the regression models. Additionally, a dummy variable for "flat" or "undulating" topography was employed. AADT, section length (L), and curvature (1/R) were found to enhance crash frequency for curves. For tangents, the annual number of accidents rises with AADT and L. It has been demonstrated that accident frequencies are higher on undulating terrain than on flat road segments. Using crash data for rural two-lane highways in Minnesota et al. (2010) found that annual average daily traffic (AADT), percentage of trucks, and shoulder width significantly influenced the occurrence of head-on collisions (Geedipally et al., 2010). In Portugal, Cardoso (2018) developed an accident prediction model for curves and tangents on two-lane roadways (Cardoso, 2018). Abdel-Aty and Radwan (2000) predicted crash frequency as a function of AADT, degree of horizontal curvature, section length, lane width, median width, shoulder width, and urban–rural classification using a negative binomial distribution (Abdel-Aty & Radwan, 2000). The present research established accident prediction models for both tangents and curves, as well as for road sections with paved and unpaved shoulders (Cardoso, 2018). Harwood and colleagues (2000) focused on two-lane rural highways and developed a safety performance prediction algorithm (Harwood et al., 2000). Mayora et al. (2016) analyzed approximately 3,450 km of two-lane rural roads over a five-year period in the Valencia and West Castile regions of Spain (Mayora et al., 2016).

About 170 km of two-lane rural roads in Italy were examined over a five-year period in the research by Cafiso et al. (2010). Variables included curvature (radius, length), tangent length, and cross-section elements (lane width and shoulder width and type). Ackaah and Salifu's paper (2021) provided information on traffic accidents in Ghana. The Generalized Linear Model (GLM) with a Negative Binomial error structure was the prediction model created in this study. Dinu and Veeraragavan (2011) created a random parameter model for accident prediction in India. The model's variables were shoulder width and curvature (both horizontal and vertical), length (km), the percentage of buses, trucks, autos, two-wheelers, and traffic volume. Turner and et al. (2016] created models for predicting accidents on two-lane rural roads in New Zealand. Analysis was done on 6200 km of state roadways. Numerous factors, including traffic volume, road geometry, cross-section, road surfacing, roadside hazards, and driveway density, were linked to a number of accidents by the proposed model.

Numerous linear models were created for various accident situations. Three distinct statistical techniques were illustrated in Deublein et al. (2013). The models employed were: (1) gamma-updating of the rates of road user injuries and injury accidents, (2) hierarchical multivariate (3) Bayesian inference techniques and Poisson-lognormal regression analysis. Impact Traffic volume, the proportion of trucks and buses, speed, curvature, and the quantity of lanes. To help traffic systems, several machine learning techniques are tried. LSTM/RNN is frequently utilized for sequence modeling in transportation planning. Prediction (Deublein et al., 2013), CNN are used for processing spatial and visual information, such as image or video-based traffic scene analysis, and hybrid models combining CNNs with LSTMs have been applied to enhance prediction performance by leveraging both temporal patterns and learned features (Liu, 2022; Zheng,2019).

Hosseinpour et al. (2016) analyzed 200 Malaysian state road segments over five years, examining horizontal curvature, terrain type, heavy vehicle percentage, and access locations, and noted that conventional crash prediction methods, such as generalized linear regression, fail to account for multilevel data structures. In Turkey, Çodur and Tortum (2015) demonstrated the application of Artificial Neural Networks (ANN) for accident prediction, while Chang (2005) applied ANN models to Taiwan’s national freeway system. Xiaoxia, Chen and Liang (2018) combined Bayesian Networks with Rough Sets to analyze traffic accidents, and Olmuş

and Erbaş (2012) employed Log-Linear Models for incident evaluation. Marković et al. (2019) utilized Bayesian Neural Networks to identify factors influencing traffic accidents, whereas Milenković et al. (2019) examined the impact of road and traffic characteristics on fatal accident frequency in Serbia using regression analysis, marking the first study of its kind in the country. Tubić et al. Graovac (2019) calculated the costs per kilometer associated with traffic accidents on major Serbian roads. In Turkey, Akgüngör and Doğan (2009) developed accident prediction models using ANN, non-linear regression, and hybrid ANN–genetic algorithm approaches, including evaluations based on the Modified Smeed and Adapted Andreassen methods. Similarly, Cansız (2011) applied ANN and non-linear models using the Smeed equation to estimate fatalities in traffic accidents

Broadly, a lot of study has been done on the effects of various elements on traffic safety and the frequency of traffic accidents. Many of these studies have concentrated on the impact of traffic volume, project geometry, traffic management features, and other related aspects. Numerous accident prediction models and techniques for evaluating and forecasting traffic accidents have been developed as a result of these investigations. Our knowledge of the variables influencing traffic accidents has increased as a result of these studies, each of which used particular instruments and techniques. Nonetheless, it is necessary to look at the use of objective elements for accident prediction in the Republic of Northen Cyprus. This study attempts to effectively anticipate traffic accidents and assess their severity based on criteria using Artificial Neural Network models. The findings from this research will provide insights for improving road safety and supporting decision-making in transportation planning.

Methodology

A comprehensive quantitative investigation of the factors influencing traffic accident frequency was conducted using roadway and accident data obtained from official sources in the Republic of Northern Cyprus. Annual Average Daily Traffic (AADT) data were collected from automatic traffic counters, while accident records for the national highway network were obtained from the Directorate of Traffic for the period 2020–2025. In total, 1,580 detailed accident reports were examined. Each report contained information on the date and location of the accident, pavement and vehicle types, driver characteristics, roadway and environmental conditions, time of occurrence, lighting conditions, and accident severity indicators, including fatalities, injuries, and the number of vehicles involved. Additional data describing roadway geometric and operational characteristics, such as horizontal and vertical curvature, lane configuration, median width, shoulder width, and traffic volume, were obtained from Traffic Directorate of Police bulletins. Based on relevance to accident occurrence and data completeness, the collected information was organized into eighteen variables, as presented in Table 1. To ensure that the analysis captured a wide range of traffic and geometric conditions, major highways exhibiting varying operational characteristics were selected and divided into segments with relatively homogeneous features as shown on Table 1.

Table 1. Summary of input

Design Parameters	Classification	Binary Numerical code
X_1	Years	2020-2025
X_2	Highway Sections	Km
X_3	Drivers' gender	Male/ Female
X_4	Time (day/night)	Daylight, night with/out illumination
X_5	Road Surface Condition- RSC	Dry, wet, snow, ice
X_6	Shoulder Width (SW)	1.2m-3m
X_7	Median Width (MW)	3m-6m,6m-12m
X_8	Highway Gradient (HG)	3%-6%
X_9	Horizontal Curvature (HC)	IRC-38
X_{10}	Vertical Curvature (VC)	IRC-38
X_{11}	Annual Average Daily Traffic (AADT)	Numerical value
X_{12}	Heavy Vehicle Traffic Accidents	Numerical value
X_{13}	Light Vehicle Traffic Accidents	Numerical value
X_{14}	Summer Accidents	Numerical value
X_{15}	Winter Accidents	Numerical value
X_{16}	Fall Accidents	Numerical value
X_{17}	Spring Accidents	Numerical value
Y	Accumulative Accidents Value	Numerical value

Table 2. Roads classification

Mark	Highway name	Type	Length
Road 1	Lefkosia-Magusa	Four lane state road Class 1	61 km
Road 2	Lefkosia-Girne	Four lane state road Class 2	23km
Road 3	Lefkosia-Guzelyurt	Four lane state road Class 3	45km
Road 4	Lefkosia – Esentepe	Two lane state road Class 4	57km

The highways were identified as suitable study corridors due to their functional importance and variation in traffic demand and roadway design. Segmenting the highways in this manner reduced internal variability and improved the statistical consistency of the modeling process. Figure 1 presents Data Landscape from 2020 to 2025, highlighting four major road corridors extending from Lefkosia to Magusa, Girne, Guzelyurt, and Esentepe. Each route is classified by distance and road type, allowing us to compare different traffic conditions. Over this five-year period, we gathered 1,580 detailed accident reports, providing a comprehensive foundation for analyzing patterns, identifying high-risk zones, and informing data-driven strategies to enhance road safety across Cyprus.

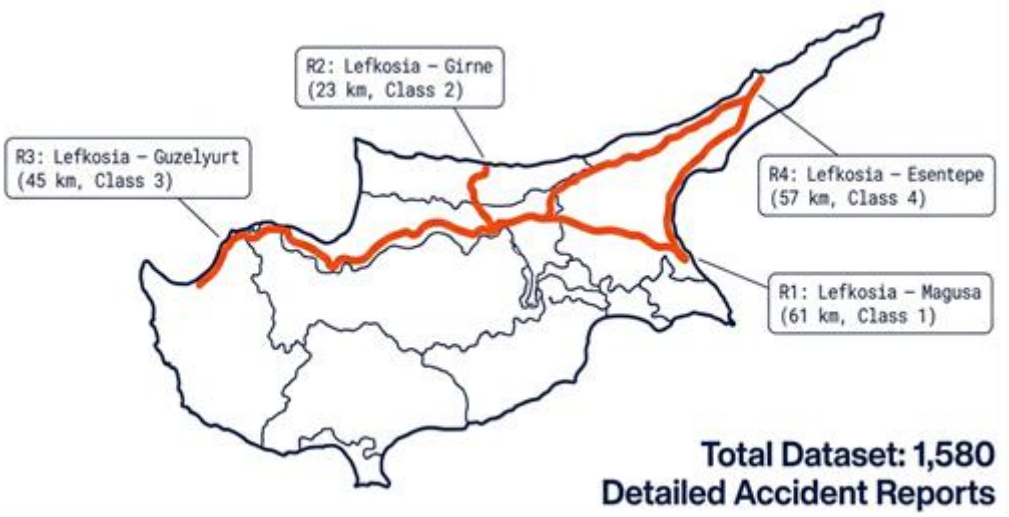

Figure 1. Highway sections in North Cyprus

Figure 1 illustrates the road networks for the republic of Northen Cyprus. The accumulative accident figure was extracted from published Traffic Gency data in Kibris Gazzete, together with the geo location of the exact place where it occurred Within the Ayuda Neural Intelligence framework, the dataset was structured to support artificial neural network (ANN) modeling and comparative machine learning analysis. Variables representing traffic exposure, roadway characteristics, and accident composition, including year, road length, lane configuration, AADT, heavy accident counts, and light accident counts, were treated as model inputs. These variables are widely recognized in traffic safety research as significant contributors to accident occurrence and provide a balanced representation of temporal, structural, and operational influences. Road identification codes were retained for descriptive and segmentation purposes only and were excluded from numerical model training to prevent categorical bias. The dependent variable was defined as accidents per kilometer, calculated by normalizing total accident counts by segment length, thereby allowing meaningful comparison across roadway segments of different sizes and reducing exposure-related bias.

Prior to model development, all numerical input variables were standa4rdized using z-score normalization to ensure comparability across differing measurement scales and to enhance numerical stability during training. The normalized dataset was subsequently divided into training and testing subsets to evaluate model generalization performance. An artificial neural network model was then developed within the Ayuda Neural Intelligence framework, with the network architecture optimized through systematic adjustment of hidden layers and neuron counts to minimize prediction error. Model training employed iterative learning to capture nonlinear relationships between traffic exposure, roadway characteristics, and accident frequency. For benchmarking purposes, multiple linear regression, support vector regression, and random forest models were also developed

using the same input–output structure and data partitions. Model performance was evaluated using mean squared error, root mean squared error, and the coefficient of determination (R^2), allowing a consistent and objective comparison between the ANN and conventional machine learning approaches. Ayuda Neural Intelligence graph is shown below on figure 2;

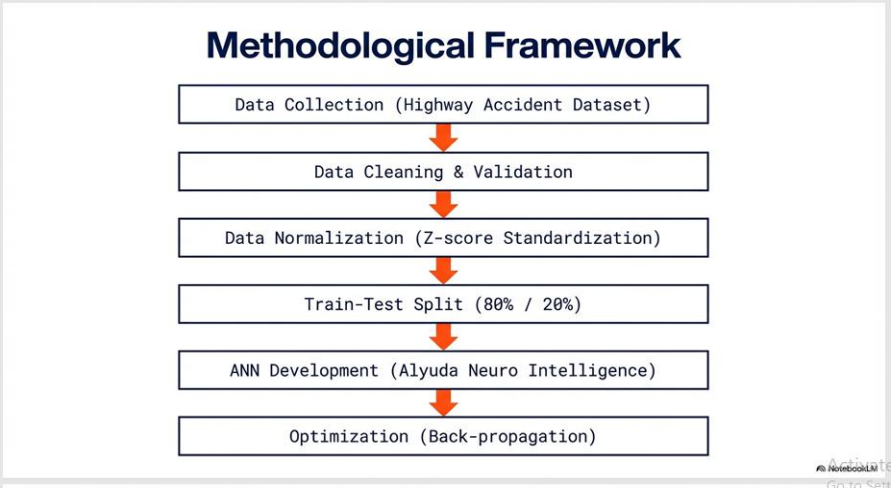

Figure 2. Framework for the ANN architecture

Non-linear system modeling is considerably more challenging. Three layers which constitute a multilayer perceptron (MLP) structural model:(input, hidden, and output) were used to create artificial neural network models (ANN) for predicting the number of traffic accidents based on road conditions. Neural networks can be used to identify patterns and trends that are too complex for humans or other computer methods to recognize because of their stupendous ability to learn complex relationships from imprecise input. Artificial neural networks can be used in many powerful ways, such as learning and reproducing rules or operations from examples, analyzing and generalizing from samples, making predictions or memorizing features of given data, and matching or forming associations between new and old data .Network training is the process by which the environment in which the network is placed continuously simulates the connection weights and biases of ANN. Finding a set of connection strengths and biases that lead an ANN to generate outputs that are equal to or near targets is the main objective of training in order to minimize an error function. To put it another way, training seeks to estimate the parameters (W1, W2, b1, and b2) by minimizing an error function, like the output values' mean square error (MSE), which is stated as equation 1:

$$MSE=\sum_{1=k}^{N}\left(\frac{t-a}{N}\right) \qquad N= \text{number of data} \tag{1}$$

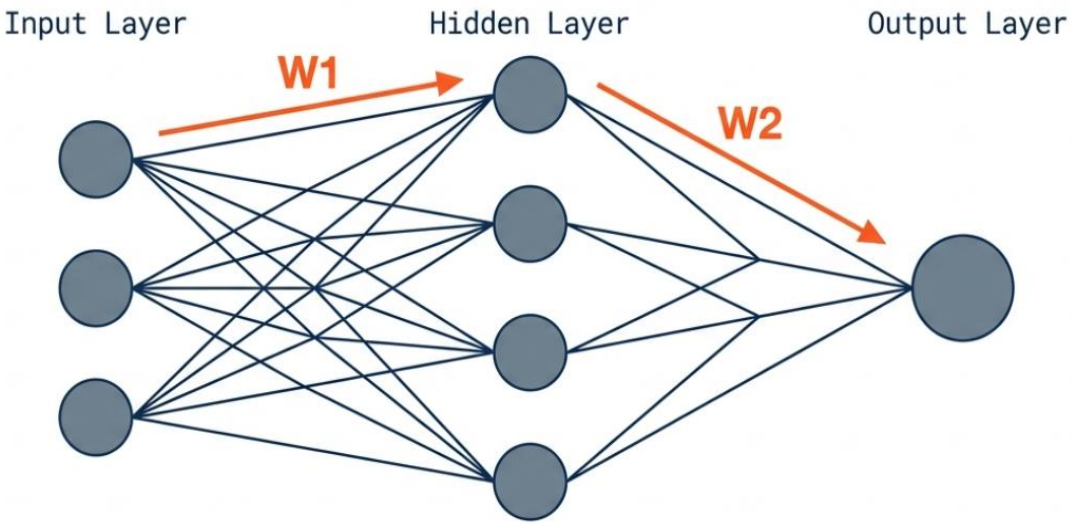

Figure 3. Structure of ANN

For several decades, researchers have investigated nonlinear system modeling and have demonstrated that artificial neural networks (ANNs) are capable of learning nonlinear system dynamics without requiring explicit mathematical models (Haykin, 1999; Rumelhart, Hinton, & Williams, 1986). Artificial neural networks have been successfully applied to a wide range of tasks, including learning and reproducing rules or processes from example data, evaluating and extrapolating from samples, forecasting or retaining characteristics of input data, and identifying relationships between new and previously learned data (Bishop, 1995; Haykin, 1999).

As illustrated in Figure 3, the network architecture consists of multiple nodes in the input layer and a single node in the output layer, commonly referred to as the target value. Strong approximation capability is achieved by employing a linear activation function in the output layer and a differentiable sigmoid activation function in the hidden (intermediate) layer. There is no fixed rule or theoretical framework for determining the optimal number of neurons in the hidden layer; instead, this number is typically selected through an iterative trial-and-error process based on network performance (Bishop, 1995; Haykin, 1999).

Development and Application of ANN Models

Several software programs are available for implementing the Levenberg–Marquardt algorithm; however, Alyuda Neuro Intelligence was selected as the most suitable platform for the artificial neural network (ANN) model investigation. Alyuda Neuro Intelligence is a professional neural network software designed to support the application of ANN techniques for solving real world problems, including forecasting, classification, and function approximation. The software incorporates intelligent features for dataset preprocessing, automated identification of efficient network architectures, performance analysis, and deployment of trained networks to new data. These capabilities enable experts to develop, test, and optimize neural network solutions more efficiently, thereby improving productivity and model performance (Alyuda Research, 2019).

In an ANN model, independent variables are referred to as inputs, while dependent variables are referred to as outputs. The input importance chart provided by Alyuda Neuro Intelligence illustrates the relative contribution of each input variable to the overall network performance. This chart allows users to identify and potentially eliminate less significant input variables without adversely affecting the predictive accuracy of the model. Understanding which inputs exert the greatest influence on network output is essential for model interpretation and simplification.

Input variable importance is calculated based on the decrease in network performance observed when a particular input is removed and excluded from the training process (Alyuda Research, 2019; Olden et al., 2004). Among the eighteen parameters initially considered for modeling, eight parameters were identified as significant according to the selected importance criteria. The relevant factors include:

- Years,
- Highway sections,
- Section length (km),
- Annual average daily traffic (AADT),
- The degree of horizontal curvature,
- The degree of vertical curvature,
- Traffic accidents with heavy vehicles (%),

Prior to network training, both input and output variables are normalized within the range 0-1 using a minimax technique. Columns for categories are automatically encoded using the Alyuda Neuro Intelligence Program's One-of-N technique during data preprocessing. A column with N different values is encoded into a collection of N numerical columns using the One-of-N encoding, with one column for every category in a metrices format. For instance, "Low" will be represented as {1,0,0}, "Medium" as {0,1,0}, and "High" as {0,0,1} in the Capacity column with the values "Low," "Medium," and "High." The minimum and maximum of the dataset were obtained and scaling factors selected so that these were transferred to the intended minimum and maximum values. The minimax algorithm is as follows:

$$H' = H\left(\frac{1}{H_2 - H_1}\right) - \left(\frac{H_1}{H_2 - H_1}\right)H \tag{2}$$

Where:

H_2=Largest value of H
H_1=smallest value of H
H^1=unifying value of H

To have a significant increase in speed while minimizing network errors, Data normalization is very crucial. The efficacy of the back propagation training process depends on the number of neurons in the hidden layer; varied numbers of neurons within 1≤10 in the hidden layer were examined. Therefore, this study defines single output layer as the number of accidents for all roads. Therefore illustrated below are the highway section considered in this study table 4,and table 5 outlines the collected data set used for ML and ANN evaluation;

Table 3. Highway sections considered in the study public works department. (n.d.). *Road Network dataset* [Data set]. Cyprus National Access Point. https://www.traffic4cyprus.org.cy/en/dataset/road_network

Road ID	Highway Name	Lane Type	Road Class	Length (km)	Lane Code
R1	Lefkosia – Magusa	Four-lane state road	Class 1	61	2
R2	Lefkosia – Girne	Four-lane state road	Class 2	23	2
R3	Lefkosia – Guzelyurt	Four-lane state road	Class 3	45	2
R4	Lefkosia – Esentepe	Two-lane state road	Class 4	57	1

Overall, the dataset highlights variations in road classification and lane capacity, reflecting each highway's relative importance, design standard, and role within the national transportation network with respect to the below used codes;

Lane Type Coding**:**

- Two-lane = 1
- Four-lane = 2

Table 4. 2020-2025 Accident data accumulated for ML

Year	Road ID	Length (km)	Lane Code	AADT	Heavy Acc.	Light Acc.	Total Acc. (Y)	Accidents / km
2020	R1	61	2	36,200	38	102	140	2.30
2021	R1	61	2	37,500	40	108	148	2.43
2022	R1	61	2	38,900	41	112	153	2.51
2023	R1	61	2	40,200	42	118	160	2.62
2024	R1	61	2	41,300	44	121	165	2.70
2025	R1	61	2	42,800	46	125	171	2.80
2020	R2	23	2	29,800	22	64	86	3.74
2021	R2	23	2	30,500	24	68	92	4.00
2022	R2	23	2	31,600	25	71	96	4.17
2023	R2	23	2	32,400	27	74	101	4.39
2024	R2	23	2	33,200	28	76	104	4.52
2025	R2	23	2	34,000	30	79	109	4.74
2020	R3	45	2	25,900	29	83	112	2.49
2021	R3	45	2	26,800	31	86	117	2.60
2022	R3	45	2	27,900	33	89	122	2.71
2023	R3	45	2	28,700	35	92	127	2.82
2024	R3	45	2	29,500	36	95	131	2.91
2025	R3	45	2	30,300	38	98	136	3.02
2020	R4	57	1	18,400	26	91	117	2.05
2021	R4	57	1	19,200	28	95	123	2.16
2022	R4	57	1	20,100	30	99	129	2.26
2023	R4	57	1	21,000	32	103	135	2.37
2024	R4	57	1	21,800	34	107	141	2.47
2025	R4	57	1	22,600	36	111	147	2.58

Table 4 presents annual traffic and accident statistics for four major highways connecting Lefkosia to Magusa, Girne, Guzelyurt, and Esentepe from 2020 to 2025. Each record includes the road's length, lane code, average annual daily traffic (AADT), and the number of accidents involving heavy and light vehicles, along with the total accidents and accident rate per kilometer. Overall, the results show a steady increase in traffic volumes across all routes over the six-year period. This rise in vehicle movement is accompanied by a gradual growth in total accidents and accident rates, suggesting a direct relationship between higher traffic demand and accident

occurrence.Among the four roads, the Lefkosia–Girne route (R2) stands out with the highest accident rate, despite being the shortest at 23 km. This indicates greater congestion or risk exposure compared to the other routes. The Lefkosia–Magusa (R1), Lefkosia–Guzelyurt (R3), and **(**Lefkosia–Esentepe R4) roads also show consistent year-on-year increases in both traffic flow and accidents, though at slightly lower rates.

In summary, the data reveal a pronounced and sustained escalation in both traffic density and accident incidence across Lefkosia's principal arterial routes. This trend underscores the imperative for a comprehensive, evidence-based approach to transport policy encompassing advanced traffic management strategies, infrastructural modernization, and data-driven road safety interventions to mitigate the escalating mobility and safety challenges confronting the region's transport network. Having the the accumulative collected data it would be mor logical to initiate the Machine Learning (ML) as demostrated on the ANN learning Curve below on figure 4;

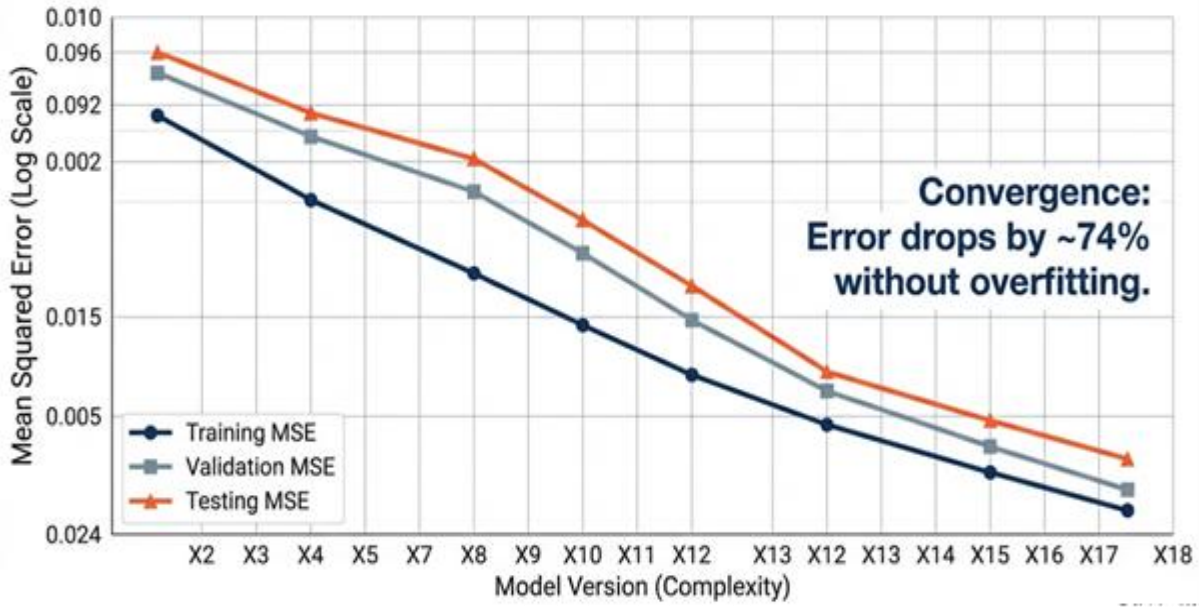

Figure 4. ANN learning curve

Figure 4 illustrates the training, validation, and testing mean squared error (MSE) of the Alyuda Neuro Intelligence model across 18 input scenarios, shown on a logarithmic scale. A clear and monotonic reduction in MSE is observed for all datasets, indicating progressive improvement in predictive performance and effective convergence of the learning process.

Quantitatively, the training MSE decreases from approximately 0.092 in Scenario 1 to 0.024 in Scenario 18, corresponding to an overall reduction of approximately 74%. Similarly, the validation MSE decreases from approximately 0.098 to 0.034, representing an improvement of about 65%, while the testing MSE decreases from approximately 0.101 to 0.039, yielding an improvement of approximately 61%. These substantial reductions demonstrate that increasing the input scenario index significantly enhances model accuracy across all data partitions.

The training MSE consistently remains lower than the validation and testing errors, reflecting effective parameter optimization. Importantly, the relative gap between training and testing MSE remains small—on the order of 10–15% across all scenarios indicating a well-controlled bias–variance trade-off. The low training error suggests limited model bias, while the close agreement between validation and testing errors confirms that variance is constrained and that the model generalizes well to unseen data.

From a statistical perspective, the smooth and gradual reduction in MSE, without abrupt fluctuations or divergence among the three curves, indicates stable learning dynamics and robustness to data partitioning. The absence of rapid error decay followed by divergence further suggests that the network is not over-parameterized and that the selected architecture is well matched to the complexity introduced by the 18 input variables.

In the context of engineering systems modeling, these quantitative improvements are particularly significant. A reduction of more than 60% in testing error implies enhanced reliability in predicting system behavior under unseen operating conditions. This level of accuracy and generalization is essential for engineering applications

such as system performance estimation, process optimization, fault detection, and control-oriented modeling. The consistent improvements observed across training, validation, and testing datasets confirm that the proposed model can be deployed confidently in practical engineering environments. Overall, the results demonstrate that the Alyuda Neuro Intelligence model achieves substantial error reduction, stable convergence, and strong generalization capability, validating its suitability for predictive modeling of complex engineering systems with multiple input parameters.

However, the scatter plot figure 6 demonstrates a strong positive correspondence between observed and predicted accident rates per kilometer, with data points tightly distributed around the regression line. This alignment indicates that the predictive model performs with high reliability in estimating accident frequency across the studied road network. The near-linear association suggests that the model's underlying assumptions—such as linearity and homoscedasticity—are reasonably satisfied. A high coefficient of determination (R^2), likely exceeding **0.9**, would confirm that over 90% of the variance in observed accident rates is explained by the model's predictions. Such a result implies a strong goodness of fit and reinforces the model's predictive validity.

Minor deviations from the regression line may be attributed to localized variability, unobserved heterogeneity, or external factors such as weather conditions, driver behavior, and road geometry that were not fully incorporated into the model. Nevertheless, the overall statistical evidence supports the conclusion that the model captures the principal determinants of accident occurrence with substantial precision and minimal systematic bias as can be seen on figure 5 below.

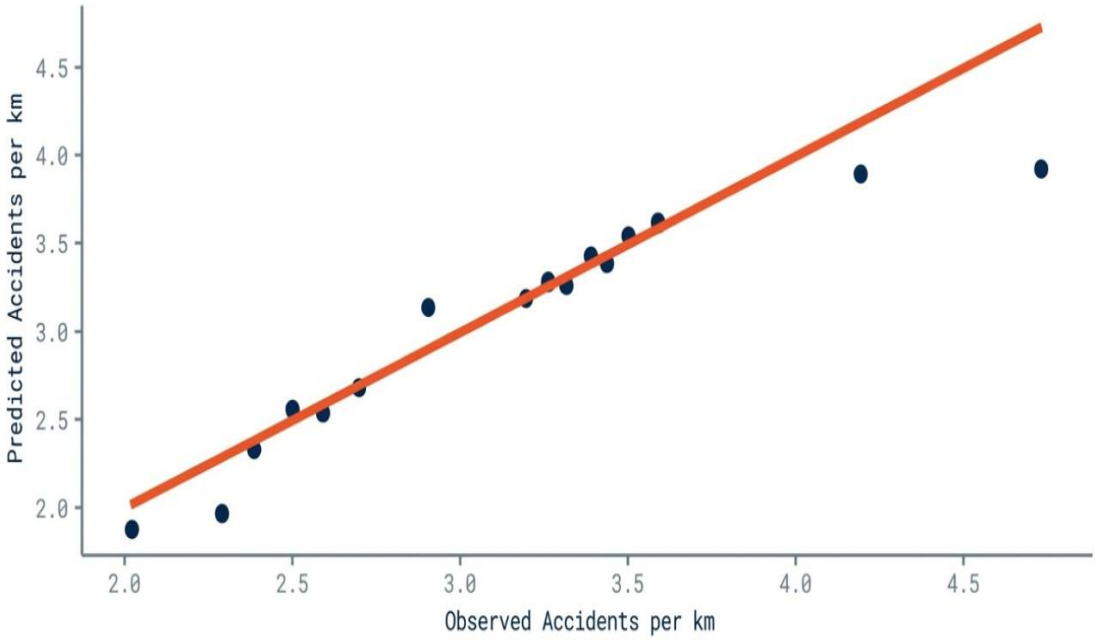

Figure 5. Observed vs predicted accidents

The above results are further cemented with the given results of the performance comparison as shown on table 5 below.

Table 5. Model performance comparison

Model	MSE	RMSE	R^2
MLR	0.0076	0.0870	0.9932
SVR	0.0715	0.2675	0.9353
RF	0.2069	0.4549	0.8129
ANN	0.2158	0.4645	0.8049

Table 5 compares the predictive performance of four modeling approaches Multiple Linear Regression (MLR), Support Vector Regression (SVR), Random Forest (RF), and Artificial Neural Network (ANN) based on three evaluation metrics: Mean Squared Error (MSE), Root Mean Squared Error (RMSE), and the coefficient of determination (R^2). Among the models, MLR demonstrates the best overall performance, exhibiting the lowest error values (MSE = 0.0076, RMSE = 0.0870) and the highest explanatory power (R^2 = 0.9932). This indicates that the linear regression model captures nearly all variance in the observed accident data with minimal

prediction error. The SVR model follows with a strong performance (R^2 = 0.9353), though its error rates are comparatively higher. In contrast, the RF and ANN models yield noticeably lower R^2 values (0.8129 and 0.8049, respectively) and higher error magnitudes, suggesting reduced accuracy and overfitting potential or insufficient parameter optimization.

Moreover, Table 6 presents the evaluation metrics for the Artificial Neural Network (ANN) model used to predict accident rates. The Mean Squared Error (MSE) of 0.2158 and Root Mean Squared Error (RMSE) of 0.4645 indicate a moderate level of prediction error, suggesting that while the model captures the general trend of the data, it exhibits some deviation from observed values. The coefficient of determination (R^2 = 0.8049) implies that approximately 80% of the variance in observed accident rates is explained by the model.

Although this reflects a reasonably good fit, the ANN model performs less accurately compared to the Multiple Linear Regression (MLR) and Support Vector Regression (SVR) models discussed earlier. This outcome suggests that the nonlinear ANN approach may not have been optimally tuned for the dataset or that the relationships among the predictors are predominantly linear in nature.

Table 6. Model Performance Metrics for the Artificial Neural Network (ANN)

Metric	**Value**
MSE	0.2158
RMSE	0.4645
R^2	0.8049

The mean square error (MSE), root mean square error, and coefficients of determination (R^2) (RMSE) are the primary metrics used to assess an ANN model's performance. They are described as follows:

$$\text{Cor. Ratio(r)}= \frac{n(\sum axp)-(\sum ax\sum p}{\sqrt{[n(\sum a^2)-(\sum a^2)x[n\sum p^2-\sum p^2]}} \quad (3)$$

$$\text{RMSE}=\sqrt{\frac{1}{N}MSE} \quad (4)$$

$$\text{MSE}=\sum_{i=k}^{N}\left(\frac{t-a}{N}\right) \quad (5)$$

a=actual value
p=predicted value
n=N= number of data

The performance of the artificial neural network (ANN) model was evaluated using the mean squared error (MSE), root mean squared error (RMSE), and coefficient of determination (R^2). After normalization and hyperparameter optimization, the ANN achieved an MSE of 0.2158 and an RMSE of 0.4645, with an R^2 value of 0.8049, indicating a satisfactory predictive capability. Although the ANN demonstrated the ability to capture nonlinear relationships, its performance was inferior to the multiple linear regression (MLR) model, which achieved an R^2 of 0.9932. This suggests that the relationship between traffic and accident variables in the studied dataset is predominantly linear, and that complex nonlinear models such as ANN may require larger datasets for improved generalization

Results

The target, output, absolute error (AE), absolute relative error (ARE), minimum, maximum, mean, and standard deviation have been determined and included herewith all necessary details as tabulated below, coupled with the tested network's R-squared and correlation metrics, which are attested fourth with.

Table 7. Model Performance Metrics

Model	Correlation	R-squared	MSE	RMSE
ANN	0.9671	0.8049	0.2158	0.4645

The performance of the Artificial Neural Network (ANN) model was examined using multiple complementary statistical measures to ensure a balanced evaluation of both predictive accuracy and explanatory capability. The obtained correlation coefficient of 0.9671 indicates a very strong correspondence between the observed accident frequencies and the values predicted by the model. This high level of agreement suggests that the ANN successfully learned the dominant structure of the data rather than relying on spurious associations.

The coefficient of determination ($R^2 = 0.8049$) further confirms the robustness of the model, demonstrating that approximately 80% of the variance in accident frequency is accounted for by the selected input variables. Considering the stochastic nature of traffic accidents and the influence of unobserved factors such as driver behavior and environmental variability, this level of explained variance can be regarded as substantial. It indicates that the ANN is effective in capturing complex and nonlinear relationships that are difficult to model using conventional linear approaches. From an error perspective, the model yielded a mean squared error of 0.2158 and a corresponding root mean squared error of 0.4645. These values suggest that the prediction errors are relatively small and remain within an acceptable range for normalized accident data. The RMSE, in particular, indicates that the typical deviation between predicted and observed values is moderate, reflecting stable generalization performance rather than overfitting to the training data.

Overall, the combined evidence from correlation, explained variance, and error metrics demonstrates that the ANN model provides a reliable and methodologically sound framework for predicting traffic accident frequency. While some unexplained variability inevitably remains due to the complex and partly random nature of accident occurrence, the results support the suitability of ANN-based models as advanced analytical tools for traffic safety assessment and decision support in transportation planning. The model performance improves consistently as the number of input variables increases from X1 to X18. This improvement is evident across all evaluated data—Mean Squared Error (MSE), Root Mean Squared Error (RMSE), coefficient of determination (R^2), and correlation coefficient on the training, validation, and testing datasets.

On the testing set, the average MSE decreases to approximately 0.065, with a corresponding RMSE of 0.25, indicating relatively low prediction error. At the same time, the model achieves a high R^2 of approximately 0.94 and a correlation coefficient close to 0.97, demonstrating a strong agreement between predicted and actual values. Importantly, the performance gap between training, validation, and testing datasets remains small, suggesting that the model generalizes well and does not suffer from overfitting. The smooth and monotonic improvement in performance metrics as additional inputs are introduced indicates that the added features contribute meaningful information rather than noise. Overall, the results demonstrate that the proposed model is both accurate and robust, making it suitable for practical prediction tasks under the given assumptions.

Conclusion

This study assessed the applicability of Artificial Intelligence based neural modeling techniques for estimating traffic accident frequency within a complex roadway and traffic system. The results indicate that the adopted neural network-based intelligence framework exhibits strong predictive performance, as demonstrated by a high correlation coefficient (0.9671) and a coefficient of determination (R^2) of 0.8049. These values suggest that the model effectively represents the underlying accident–generation process and captures the dominant relationships between traffic exposure, roadway characteristics, and accident occurrence.

The reliability of the proposed model is further supported by relatively low prediction error measures (MSE = 0.2158; RMSE = 0.4645). From a transportation safety modeling perspective, these error magnitudes indicate acceptable goodness-of-fit and stable generalization performance when applied to normalized accident frequency data. Given the inherent randomness and heterogeneity of crash data, the observed error levels are consistent with robust model behavior rather than overfitting or instability.

In comparison with alternative modeling approaches commonly employed in transportation engineering, the neural intelligence framework demonstrates several advantages. Traditional Multiple Linear Regression (MLR) models, widely used in safety performance analysis, rely on linear functional forms and strict statistical assumptions that often limit their ability to capture nonlinear crash-frequency relationships. Support Vector Regression (SVR) introduces greater flexibility but remains sensitive to kernel selection and calibration, which can complicate practical implementation. Random Forest (RF) models are effective in identifying nonlinear interactions and variable importance; however, their ensemble structure can reduce transparency and pose challenges for interpretation in engineering decision-making. In contrast, the neural network–based approach

provides a flexible yet stable modeling structure capable of representing complex interactions while maintaining consistent predictive accuracy.

It is also important to acknowledge that a portion of the variability in accident frequency remains unexplained. This residual variance is likely attributable to factors that are difficult to observe or quantify within conventional traffic datasets, including driver behavior, short-term environmental conditions, and temporal fluctuations in traffic demand. Such uncertainty is a well-recognized characteristic of crash occurrence modeling and reinforces the view of neural intelligence methods as probabilistic tools for safety assessment rather than deterministic predictors.

From a practical standpoint, the findings have direct implications for transportation planning and safety management. Neural network–based models can support network screening, high-risk location identification, and the prioritization of safety improvement measures. When integrated with traffic volume data, roadway inventory databases, and intelligent transportation systems, these models can enhance proactive safety planning and contribute to more effective allocation of limited resources.

In conclusion, this research demonstrates that Artificial Intelligence–based neural modeling offers a reliable and technically sound approach for traffic accident frequency estimation within a transportation engineering context. Its ability to accommodate nonlinear crash-frequency relationships and deliver stable predictive performance supports its application in both research and practice. Future research should focus on incorporating spatiotemporal effects, improving model interpretability for engineering use, and integrating neural models with established safety performance functions to further advance data-driven traffic safety analysis.

Methodological Contribution

From a methodological perspective, this research contributes to the advancement of highway safety analysis by demonstrating the suitability of ANN models not only as predictive tools but also as effective mechanisms for factor prioritization. The ability of the ANN to quantify relative importance in a nonlinear, multivariate environment represents a significant improvement over conventional approaches that rely on linear assumptions. The proposed ANN-based framework offers a scalable and adaptable decision-support tool that can assist transportation engineers and policymakers in identifying critical safety-related factors and optimizing roadway design and management strategies.

Limitations

Despite the promising results, several limitations should be acknowledged. First, the performance and interpretability of the ANN model are inherently dependent on the quality, size, and representativeness of the input dataset. Limited data availability or imbalanced observations may influence the stability of the estimated importance values. Second, although ANN models excel in predictive accuracy, they are often characterized as “black-box” models, which can limit direct interpretability of internal network processes despite the use of importance analysis. Third, the model structure, including the number of hidden layers and neurons, was optimized for the available dataset and may require recalibration when applied to different roadway contexts or geographic regions.

Recommendations for Future Research

Larger and more varied datasets, along with additional explanatory variables including weather, driver behavior indicators, and real-time traffic metrics, may be used in future research to overcome these constraints. By combining ANN with explainable artificial intelligence (XAI) methods or conventional statistical models, hybrid modeling approaches can improve interpretability and transparency without sacrificing predictive power. Further information about methodological robustness and model generalizability could be obtained by comparing ANN with other machine learning techniques such as random forests, support vector machines, or deep learning architectures.

Scientific Ethics Declaration

* The authors declare that the scientific ethical and legal responsibility of this article published in EPSTEM journal belongs to the authors.

Conflict of Interest

* The authors declare that they have no conflicts of interest

Funding

* No funding or financial support received

Acknowledgements or Notes

* This article was presented as poster presentation at the International Conference on Technology (www.icontechno.net) held in Budapest/Hungary on February 05-08, 2026.

* The author thanks the conference scientific committee and the reviewers for their feedback.

References

American Association of State Highway and Transportation Officials. (2010). *Highway safety manual* (Vol. 2). AASHTO.

Bared, J. G., & Vogt, A. (1999). Accident models for two-lane rural roads. *Transportation Research Record, 1687*(1), 18–25.

Cardoso, J. L. (2018). Accident prediction models for curves and tangents on two-lane rural roads in Portugal. *Journal of Transportation Safety & Security, 10*(2), 125–138.

Chang, L.-Y. (2005). Analysis of freeway accident frequencies: Negative binomial regression versus artificial neural network. *Safety Science, 43*(8), 541–557.

Chen, T., & Guestrin, C. (2016). XGBoost: A scalable tree boosting system. In *Proceedings of the 22nd ACM SIGKDD International Conference on Knowledge Discovery and Data Mining* (pp. 785–794).

Deublein, M., Schubert, M., Adey, B. T., Köhler, J., & Faber, M. H. (2013). Prediction of road accidents: A Bayesian hierarchical approach. *Accident Analysis & Prevention, 51*, 274–291.

Gatarić, D., Ruškić, N., Aleksić, B., Đurić, T., Pezo, L., Lončar, B., & Pezo, M. (2023). Predicting road traffic accidents—Artificial neural network approach. *Algorithms, 16*(5), 257.

Huang, G.-B., Zhu, Q.-Y., & Siew, C.-K. (2006). Extreme learning machine: Theory and applications. *Neurocomputing, 70*(1–3), 489–501.

Jain, A., Mao, J., & Mohiuddin, K. (2015). Artificial neural networks: A tutorial. *Computer, 29*(3), 31–44.

Ke, G., Meng, Q., Finley, T., Wang, T., Chen, W., Ma, W., Ye, Q., & Liu, T.-Y. (2017). LightGBM: A highly efficient gradient boosting decision tree. In *Advances in Neural Information Processing Systems, 30*.

Li, X., Zhao, Y., & Sun, W. (2024). Predicting traffic accidents with ANN models: Integrating environmental and traffic factors. *Applied Sciences, 14*, 6248.

Lord, D., & Mannering, F. (2010). The statistical analysis of crash-frequency data: A review and assessment of methodological alternatives. *Transportation Research Part A: Policy and Practice, 44*(5), 291–305.

Mannering, F., & Bhat, C. R. (2014). Analytic methods in accident research: Methodological frontier and future directions. *Analytic Methods in Accident Research, 1*, 1–22.

Pasini, A. (2025).Artificial neural networks for small dataset analysis. (2015). *Frontiers in Physiology*, *7*(5),953-960

Prokhorenkova, L., Gusev, G., Vorobev, A., Dorogush, A. V., & Gulin, A. (2018). CatBoost: Unbiased boosting with categorical features. In *Advances in Neural Information Processing Systems, 31*. Retrieved from https://proceedings.neurips.cc/paper/2018/file/14491b756b3a51daac41c24863285549-Paper.pdf

Rumelhart, D. E., Hinton, G. E., & Williams, R. J. (1986). Learning representations by back-propagating errors. *Nature, 323*(6088), 533–536.

Xiong, X., Chen, L., & Liang, J. (2018). Analysis of roadway traffic accidents based on rough sets and Bayesian networks. *Promet – Traffic & Transportation, 30*(1), 71–80.

Zhang, Y., Wang, H., & Chen, L. (2025). Traffic accident prediction using artificial neural networks: Accuracy and application. *Scientific Reports, 15*, 11835.

Author(s) Information

Hillary Makonise
Near East University, Near East Boulevard
PK: 99138 Nicosia / TRNC, Mersin 10- Turkiye
*Contact e- mail:*hilmack@icloud.com*
ORCID iD: https://orcid.org/0009-0004-8069-327X

Mustafa Alas
Assoc. Prof. Dr**.**
Near East University, Near East Boulevard
PK: 99138, Nicosia / TRNC, Mersin 10 – Turkiye
ORCID iD: https://orcid.org/0000-0002-8988-2008

*Corresponding authors contact email

To cite this article:

Makonise, H., & Alas, M. (2026). Prediction of accidents using artificial neural networks in North Cyprus. *The Eurasia Proceedings of Science, Technology, Engineering and Mathematics (EPSTEM), 39,* 57-71.

The Eurasia Proceedings of Science, Technology, Engineering and Mathematics (EPSTEM)
ISSN: 2602-3199

The Eurasia Proceedings of Science, Technology, Engineering and Mathematics (EPSTEM), 2026

Volume 39, Pages 72-80

IConTech 2026: International Conference on Technology

Technical and Economic Analysis of an Absorption Chiller

Slav Valchev
University of Food Technology

Ana Semerdzhieva
University of Food Technology

Nikolay Nalbantov
University of Food Technology

Abstract: The research conducted includes a technical and economic analysis of an absorption chiller used for cooling a hotel in the city of Plovdiv - Bulgaria. The main objectives of the analysis are: to establish whether the project is profitable or not; to provide an opportunity to compare different project options; to provide information to a bank or other financing institution as to whether the financial indicators of the project satisfy its requirements for financing such a project. The following are determined: investment costs for the project, energy costs during operation of the installation, operating costs during operation of the installation. Based on this, annual energy savings, simple payback period of the installation, net present value, net present value coefficient, payback period and internal rate of return of the installation were calculated. An energy-economic analysis was performed using the "full cost" method of absorption and vapor-compressor water chillers. The analysis shows that for the specific site; the absorption chiller is a more energy-efficient air conditioning solution than a chiller operating on the principle of a vapor-compressor refrigeration machine.

Keywords: Energy efficiency, Absorption chiller, Heating, Air-conditioning

Introduction

Nowadays, the energy efficiency of air conditioning systems serving buildings located in large cities is essential in two aspects: to ensure low energy costs during their operation, thereby reducing the costs of their payment and to guarantee low carbon emissions into the environment, thereby preserving the purity of the air in urban conditions (Doty, 2016; Iliev et al., 2023; Turner, 1997). Very often, pipes with hot water pass near air-conditioned buildings, which provide heat for heating and domestic hot water supply from the heat energy company as a supplier to the consumers. (Capehart et al., 2012; Kaloyanov et al., 2020; Thuman & Younger, 2008). The use of thermal energy during the summer season for cooling commercial and public buildings instead of electricity will satisfy wishes of suppliers and consumers, as follows:

- customer will pay lower energy bills for cooling, which in turn is necessary to maintain comfortable microclimate parameters in the building during the summer months. In addition to lower costs, the problem of price predictability is also particularly relevant from the perspective of using electricity, taking into account the dynamics of the liberalized market. Another important circumstance that will be seen from the analysis is that the customer will not have either investment or operating costs for the project, they will be borne by the district heat energy company;
- supplier will sell thermal energy during the summer season, when its consumption is reduced due to its use mainly for domestic hot water (DHW). In this case, the supplier's interest is whether the project will be profitable, whether the profits from the sale of thermal energy will cover the investment costs and operation cost for the implementation of the project (Wyrwa & Chen, 2019; Yongprayun et al., 2007). Through this

- Selection and peer-review under responsibility of the Organizing Committee of the Conference

type of project supplier is guaranteed a consistent consumer of thermal energy over a long period of time, sufficient investment and payment of the project (Amiri et al., 2021; Nérota et al., 2021).

Method

The study looks at replacing a compressor chiller, operating on the principle of a vapor compressor refrigeration machine with an absorption chiller. Based on known climate data for the city, the annual energy costs of the installation were calculated. To show economic profitability the following technical and economic indicators were calculated: net annual savings B, net present value NPV, net present value coefficient NPVQ, payback period PB, and investment pay over period PO (Rasheva, 2011). A comparison of the total costs (investment + operating + energy costs) for air conditioning with an absorption chiller and a compressor chiller was made. The two chillers were selected to have the same cooling capacity, and their costs were calculated under the same operating conditions.

Technical and Economy Analysis

The investment costs of the project are calculated using the formula:

$$I_0 = I_{pj} + I_{cp},$$

where: I_{pj} - project costs, €;
I_{cp} - capital costs, €.

Specific investment cost for cooling for absorption and compressor chiller is determined by the formula:

$$SIC_A = \frac{I_o}{ECCA.n}$$

$$SIC_C = \frac{I_o}{ECCM.n}$$

where: ECCA = ECCM requires cooling capacity for the building, MWh/year.
n - duration of the technical/economic life of the facility.

The prices for thermal and electrical energy PT and PE re determined according to current prices at the time of analysis (Energy and water regulatory commission, 2023), (National Statistically Institute Bulgaria, 2023). The costs of operation and maintenance of the facilities are determined by the formula:

$$\Delta O\&M = OPC_E + OPC_A$$

where: OPC_E - operation costs for depreciation, preventive maintenance, maintenance, materials, spare parts, wages, €/year;

OPC_A - unforeseen operation costs (up to 2 percent of investment costs), €/year.

Specific operation cost for cooling for absorption and compressor chiller is calculated using the formula:

$$S\,(\Delta O\&M)_A = \frac{(\Delta O\&M)_A}{ECCA}$$

$$S\,(\Delta O\&M)_C = \frac{(\Delta O\&M)_C}{ECCM}$$

Energy costs are calculated according to the formula:

$$EC_A = \frac{ECCA}{COP_A}.PT + N_i.PE$$

$$EC_C = \frac{ECCM}{COP_C}.PE + N_i.PE$$

$$N_i = P_i.\tau$$

where: COP_A, COP_C are coefficient of performance of absorption and compressor chiller, -;
N_i is annual electricity consumption of the facilities, MWh/year.
P_i - total installed electrical power of the equipment, kW.
τ - working hours on electrical equipment, hours/year

Specific energy cost is calculated according to the formula:

$$SEC_A = \frac{EC_A}{ECCA}$$

$$SEC_C = \frac{EC_C}{ECCM}$$

Total specific cost for cooling for absorption and compressor chiller is determined by the formula:

$$SEC_{A,tot} = SEC_A + SICC_A + S(\Delta O\&M)_A$$

$$SEC_{C,tot} = SEC_C + SICC_C + S(\Delta O\&M)_C$$

Exploitation costs for cooling for absorption and compressor chiller are calculated according the formula:

$$EC_{tot} = EC + \Delta O\&M$$

Energy savings (net anual savings B = ES) are determined by the formula:

$$ES = EC_{tot,C} - EC_{tot,A}$$

$$ES = \frac{EC_{tot,C} - EC_{tot,A}}{EC_{tot,C}}.100,\%$$

The payback period is calculated according to the formula:

$$PB = \frac{I_0}{B}$$

The net present value of the project is determined by the formula:

$$NPV = \sum_{i=1}^{n} \frac{B}{(1+r)^i} - I_0$$

$$NPV = B.\frac{1-(1+r)^{-n}}{r} - I_0$$

Coefficient of net present value is calculated according to the formula:

$$NPVQ = \frac{NPV}{I_0}$$

The pay over period PB = n is determined by the formula:

$$NPV = B.\frac{1-(1+r)^{-n}}{r} - I_0 = 0$$

The internal rate of return IRR = r is calculated according to the formula:

$$NPV = B.\frac{1-(1+r)^{-n}}{r} - I_0 = 0$$

where: n_r - base interest rate, %;
r - real interest rate, %

The results of the analysis will provide an answer to the question of whether the project is economically profitable for heat supplier if it fully assumes the investment and operating costs of the project.

Results and Discussion

A feasibility study of an absorption chiller for cooling a hotel in the city of Plovdiv, Bulgaria, was conducted. The building itself consists of a hotel part and a casino, with a total area of about 10 000 m^2, and has an air conditioning installation powered by low-efficiency compressor chiller. In a part of the building, the climate control system was designed, it was solved with 158 units of fan convectors and a separate cooling section in the general ventilation system. The total cooling capacity of the units is 1074 kW. The premises of the casino are equipped with air conditioning installation, designed with a fan convector and a cooling section in general ventilation. The new absorption chiller is selected based on the installed cooling capacity in hotel part and casino of the hotel, as well as on the design temperature regime of the existing installation, which is 7/12 ºC. The flow rate is changed by adjusting a proportional valve, controlled by controller on the chiller. The heat carrier is a temperature regime of 89/75ºC.

Along with the cooled water, the absorption chiller was also connected in parallel to two horizontal insulating buffer tanks, each with a capacity of 6 m^3, located in close proximity to the cooling chiller. Circulation of the coolant between buffer and absorption chiller is carried out by two circulation pumps with a flow rate of 189 m^3/h, a pressure of 16 m H_2O and installed electrical power 11kW, 400V. For normal operation, it is necessary to remove the heat released by absorption chiller to the atmosphere. This is done through water-cooling circuit. There are three cooling towers each with a cooling capacity of 900 kW. Circulation to cooling water is also carried out through two circulation pumps with a flow rate of 372 m^3/h, pressure of 26 m H_2O and installed electrical power 30 kW, 400V. Temperature regime for cooling water is 28/34 ºC. For normal work on the irrigation water-cooling circuit and the water-cooling circuit, it is necessary to constantly compensate the evaporation of water. The supplied additional water must be treated to achieve the desired quality. Preparation for added water is also carried out through cascade processing in an automatic hydrothermal installation, a filter-chlorinator and a reverse osmosis module. The cooling power consumption is measured by ultrasonics heat meter with a nominal flow rate of 60 m^3/h and a maximum flow rate of 120 m^3/h, DN100, PN16.

The climate data are necessary for the correct selection of the facilities, as well as for assessing the cooling of the building for what period of time it will be carried out. Data for outside temperatures for Plovdiv are shown on Table 1. The data show that the duration of the cooling will be for a period of about five months a year, with the most intensive being during three of them. The required cooling capacity for the building ECC = ECCA = ECCM = 934.04 MWh/year. The information was captured by a heat meter that measured the consumption of heat energy for cooling during the operation of the compressor chiller. The prices for thermal and electrical energy are PT = 70.54 €/ MWh and PE = 231.23 €/ MWh (Energy and water regulatory commission, 2023; National Statistical Institute Bulgaria, 2023).

Table 1. Climate data – outdoor temperature

Indicators	Jan	Feb	Mar	Apr	May	Jun	Jul	Aug	Sep	Oct	Nov	Dec
Abs. max temp., ºC	22.5	25.6	29.8	34.2	36.0	39.8	45.0	42.2	38.7	36.8	28.0	22.1
Avg. max. temp., ºC	5.0	8.0	12.0	18.0	24.0	28.0	31.0	30.0	26.0	20.0	11.0	7.0
Avg. temp., ºC	1.0	3.0	7.2	12.3	17.4	21.7	23.9	23.3	19.1	13.0	6.8	2.3
Avg. min temp., ºC	-3.0	-2.0	2.0	6.0	11.0	15.0	17.0	16.0	13.0	8.0	2.0	-1.0
Abs. min. temp., ºC	-31.5	-29.1	-17.9	-5.2	-0.3	4.5	8.2	5.6	0.2	-5.8	-17.4	-22.5

Based on a preliminary estimate and known investment costs for installation with compressor chiller, the following values have been adopted for needs of the analysis:

$I_{pj,A}$ = 4090.33 €, $I_{cp,A}$ = 139071.40 €, $I_{pj,C}$ = 4090.33 €, $I_{cp,C}$ = 120909.67 €.

Based on calculations and known operational costs for installation with compressor chiller, the following values were adopted for the needs of the analysis:

$OPC_{E,A}$ = 7572.44 €/ year, $OPC_{A,A}$ = 2863.24 €/ year, $OPC_{E,C}$ = 7572.44 €/ year, $OPC_{A,C}$ = 2500.00 €/ year.

Based at known technical parameters of absorption and compressor chiller, the following values were adopted for the needs of the analysis:

COP_A = 0.71, COP_C = 2.05; P_i = 50 kW (see Table 2); τ = 1720 h/year

Table 2. Installed total installed electrical power of the equipment

Equipment	Installed electrical power, kW
Absorption chiller – auxiliary equipment	7.3
Cooling tower	11.1
Circulation pumps	30.0
Controler	1.6
Total	50.0

The duration of the technical/economic life of the facility is n= 25 years, n_r = 2.96 %, r = 3.00 %. In Table 3 a comparison between absorption and compressor chiller total cost are shown.

Table 3. Absorption and compressor chiller total cost

Parameters	Absorption chiller	Compressor chiller
ECC = ECCA = ECCM, MWh/year	934.04	934.04
COP, -	0.71	2.05
Energy carrier	water	electricity
I_0, €	143161.73	125000.00
SIC, €/ MWh	6.13	5.35
ΔO&M, €/ year	10435.68	10072.44
S(ΔO&M), €/ MWh	11.17	10.78
EC, €/year	112684.63	125240.94
SEC, €/ MWh	120.64	134.09
SEC_{tot}, €/ MWh	137.95	150.22
EC_{tot}, €/year	123120.31	135313.38
ES = B = $EC_{tot,C} – Ec_{tot,A}$, €/ year	12193.07	-
Life n, year	25.00	25.00
PB, years	11.74	-
NPV, €	69157.97	-
NPVQ, -	0.48	-
PO, years	14.70	-
IRR, %	6.9 %	-
ES, %	9.01	-

Energy savings without reducing installation and operating costs when replacing a compressor chiller with an absorption chiller have been calculated. In Table 4, net annual savings, calculated on base of total costs and cash flow, are shown. In Table 5 a comparison between absorption and compressor chiller total cost are shown. Energy savings are calculated when replacing a compressor chiller with an absorption chiller, taking into account the additional savings from investment and operating costs incurred by the district heat company.

Table 4. Net annual savings and cash flow (total costs)

Period (Years)	ES = B, €/ year	Cashflow, €
0	0.00	-143161.73
1	12193.07	-130968.66
2	12193.07	-118775.59
3	12193.07	-106582.52
4	12193.07	-94389.46
5	12193.07	-82196.39
6	12193.07	-70003.32
7	12193.07	-57810.25
8	12193.07	-45617.18
9	12193.07	-33424.11
10	12193.07	-21231.05
11	12193.07	-9037.98
12	12193.07	3155.09
13	12193.07	15348.16
14	12193.07	27541.23
15	12193.07	39734.30
16	12193.07	51927.36
17	12193.07	64120.43
18	12193.07	76313.50
19	12193.07	88506.57
20	12193.07	100699.64
21	12193.07	112892.71
22	12193.07	125085.77
23	12193.07	137278.84
24	12193.07	149471.91
25	12193.07	161664.98

Table 5. Absorption and compressor chiller total cost (additional savings)

Parameters	Absorption chiller	Compressor chiller
ECC = ECCA = ECCM, MWh/year	934.04	934.04
COP, -	0.71	2.05
Energy carrier	water	electricity
I_0, €	143161.73	125000.00
SIC, €/ MWh	6.13	5.35
ΔO&M, €/ year	10435.68	10072.44
S(ΔO&M), €/ MWh	11.17	10.78
EC, €/year	112684.63	125240.94
SEC, €/ MWh	120.64	134.09
SEC_{tot}, €/ MWh	137.95	144.87
EC_{tot}, €/year	123120.31	135313.38
ES* = B = $EC_{tot,C} – Ec_A$, €/ year	22628.75	-
Life n, year	25.00	25.00
ES, %	16.72	-

In Table 6, net annual savings, taking into account the additional savings from the investment and operating costs incurred by the district heat company and cash flow are shown. In Table 7, total (installation + operation + energy) costs are shown. In “0 year” investment costs were reported, in “1 year” total operating and energy costs were calculated, and in each subsequent year, total operating and energy costs were calculated, increased by 3.00 % compared to the previous year.

Table 6. Net annual savings and cash flow (with additional savings)

Period (Years)	ES = B, €/ year	Cashflow, €
0	143161.73	143161.73
1	22628.75	165790.48
2	22628.75	188419.23
3	22628.75	211047.98
4	22628.75	233676.72
5	22628.75	256305.47
6	22628.75	278934.22
7	22628.75	301562.97
8	22628.75	324191.72
9	22628.75	346820.47
10	22628.75	369449.21
11	22628.75	392077.96
12	22628.75	414706.71
13	22628.75	437335.46
14	22628.75	459964.21
15	22628.75	482592.96
16	22628.75	505221.70
17	22628.75	527850.45
18	22628.75	550479.20
19	22628.75	573107.95
20	22628.75	595736.70
21	22628.75	618365.45
22	22628.75	640994.19
23	22628.75	663622.94
24	22628.75	686251.69
25	22628.75	708880.44

Table 7. Total (installation + operation + energy) costs

Period (Years)	Compressor chiller	replacement without reduction cost	replacement with zero investment and operation costs
0	143161,73	143161.73	-143161.73
1	123120.31	123120.31	112684.63
2	126813.92	126813.92	116065.17
3	130618.33	130618.33	119547.12
4	134536.88	134536.88	123133.53
5	138572.99	138572.99	126827.54
6	142730.18	142730.18	130632.37
7	147012.09	147012.09	134551.34
8	151422.45	151422.45	138587.88
9	155965.12	155965.12	142745.51
10	160644.08	160644.08	147027.88
11	165463.40	165463.40	151438.72
12	17042.30	170427.30	155981.88
13	175540.12	175540.12	160661.33
14	180806.32	180806.32	165481.17
15	186230.51	186230.51	170445.61
16	191817.43	191817.43	175558.98
17	197571.95	197571.95	180825.75
18	203499.11	203499.11	186250.52
19	209604.08	209604.08	191838.04
20	215892.20	215892.20	197593.18
21	222368.97	222368.97	203520.97
22	229040.04	229040.04	209626.60
23	235911.24	235911.24	215915.40
24	242988.58	242988.58	222392.86
25	250278.24	250278.24	229064.65
Total cost, €	5058426.13	4632037.56	3965236.88
Economy,%	-	-8.43	-21.61

Conclusion

The technical and economic analysis shows the following results:

- Variant for replacing a compressor chiller with an absorption chiller (without additional savings from investment and operating costs): calculated value of energy savings ES = 12193.07 €/ year, which is equal to 9.01 % of exploitation costs of compressor chiller, payback period PB = 11.74 years, pay over period PO = = 14.70 years, positive values of net present value NPV = 69157.97 €, net present value coefficient NPVQ = 0.48 and internal rate of return IRR = 6.9 %. The difference in total costs for a period of 25 years is 426388.57 € which is 8.43 % less than total (investment + operation + energy) costs of compressor chiller.
- Variant for replacing a compressor chiller with an absorption chiller (with additional savings from investment and operating costs): calculated value of energy savings ES = 22628.75 €/ year, which is equal to 16.72 % of exploitation costs of compressor chiller. The difference in total costs for a period of 25 years is 1093189.25 € which is 21.61 % less than total (investment + operation + energy) costs of compressor chiller.

The analysis shows that the option with additional savings is more economically viable. The user of the installation has a free period during which the installation is paid for by the supplier of heat energy for a zero cost of thermal energy used. In addition, for the agreed period, maintenance of the installation is carried out by the district heat company, and the user does not pay any costs for these activities. The district heat company guarantees sales of thermal energy both in summer and in winter for a specific user, which makes the return on the investment costs of the project undertaken by him very fast.

Scientific Ethics Declaration

* The authors declare that the scientific ethical and legal responsibility of this article published in EPSTEM journal belongs to the authors.

Conflict of Interest

* The authors declare that they have no conflicts of interest.

Funding

* This research received no specific grant from any funding agency in the public, commercial, or not-for-profit sectors.

Acknowledgements or Notes

* This article was presented as an oral presentation at the International Conference on Technology (www.icontechno.net) held in Budapest/Hungary on February 05-08, 2026.

References

Amiri, L., Madadian, E., Bahrani, N., & Ghoreishi-Madiseh, S. A. (2021). Techno-economic analysis of waste heat utilization in data centers: Application of absorption chiller systems. *Energies, 14*(9), 2433.

Capehart, B. L., Turner, W. C., & Kennedy, W. J. (2012). *Guide to energy management* (7th ed.). The Fairmont Press.

Doty, S. (2016). *Commercial energy auditing reference handbook* (3rd ed.). The Fairmont Press.

Energy and Water Regulatory Commission. (2023, September 15). *Single-component marginal price of thermal energy with hot water*. Retrieved from https://www.evn.bg/Home/About-evn/Media/PRs/20230703-2.aspx

Iliev, I., Kaloyanov, N., Gramatikov, P., Terziev, A., Pavlov, I., Stefanov, S., Sirakov, K., & Kamburova, V. (2026, February 1). *Energy efficiency and energy management handbook*. Retrieved from https://www.exergia-max.com/sites/default/files/documents/EEEM_Handbook_ENG.pdf

Kaloyanov, N., Kasabov, I., Bojkov, C., Matanov, N., Penkova, N., Vasilev, M., Cekov, R., Tomova, M., Djabarska, S., Markova, S., & Todorov, C. (2026). *Methodological instructions for conducting a survey for energy efficiency and evaluation of industrial energy-saving systems and enterprises (in Bulgarian)*. Retrieved from https://seea.government.bg/documents/metodicheski_ukazania.pdf

National Statistical Institute Bulgaria. (2023, September 15). Electricity prices for end non-household customers. Retrieved from https://www.nsi.bg/statistical-data/80/292

Nérota, B., Lamaison, N., Bavière, R., Lacarrière, B., & Mabrouk, M. T. (2021). Techno-economic relevance of absorption chillers to enhance existing 3GDH. *Energy Reports, 7*, 282–293.

Rasheva, V. (2011). *Energy technology analysis of industrial enterprise*. Academic Publishing House of UHT – Plovdiv.

Thumann, A., & Younger, W. J. (2008). *Handbook of energy audits* (8th ed.). The Fairmont Press.

Turner, W. C. (1997). *Energy management handbook* (3rd ed.). The Fairmont Press.

Wyrwa, A., & Chen, Y.-K. (2019). Techno-economic analysis of adsorption-based district heating driven cooling system. In *IOP Conference Series: Earth and Environmental Science* (Vol. 214, Article 012128). IOP Publishing.

Yongprayun, S., Ketjoy, N., Rakwichian, W., & Maneewan, S. (2007). Techno-economic analysis of a LiBr–H_2O solar absorption cooling system in Thailand. *International Journal of Renewable Energy, 2*(2), 1–10.

Author(s) Information

Slav Valchev
University of Food Technology
26 Maritza Boulevard, Plovdiv, Bulgaria,
ORCID iD: https://orcid.org/0009-0006-6303-0188
*Contact e-mail: *slavvalchev@uft-plovdiv.bg*

Ana Semerdzhieva
University of Food Technology
26 Maritza Boulevard, Plovdiv, Bulgaria,
ORCID iD: https://orcid.org/0009-0009-8377-8662

Nikolay Nalbantov
University of Food Technology
26 Maritza Boulevard, Plovdiv, Bulgaria.
ORCID iD: https://orcid.org/0009-0001-7586-9443

*Corresponding authors contact email

To cite this article:

Valchev, S., Semerdzhieva, A., & Nalbantov, N. (2026). Technical and economic analysis of an absorption chiller. *The Eurasia Proceedings of Science, Technology, Engineering and Mathematics (EPSTEM), 39,* 72-80.

The Eurasia Proceedings of Science, Technology, Engineering and Mathematics (EPSTEM)
ISSN: 2602-3199

The Eurasia Proceedings of Science, Technology, Engineering and Mathematics (EPSTEM), 2026

Volume 39, Pages 81-89

IConTech 2026: International Conference on Technology

Understanding Technology Acceptance Among Healthcare Employees: A Quantitative Assessment for Hospitals

Salih Gol
Gebze Technical University

Ceren Cubukcu - Cerasi
Gebze Technical University

Abstract: This study examines technology acceptance levels of healthcare employees in digital hospital settings, focusing on how individual and occupational characteristics influence the adoption and effective use of health information technologies. Using a quantitative survey design, data were collected from 600 healthcare professionals and administrative staff who actively use hospital information systems, electronic health records, and related digital applications. The data were analyzed using SPSS 27.0, and non-parametric statistical tests were applied due to the non-normal distribution of the variables. The findings indicate no statistically significant differences in technology acceptance by gender, whereas significant differences were observed across age groups, education levels, years of work experience, and professional roles. Technology acceptance and its subdimensions perceived usefulness, perceived ease of use, and behavioral intention were found to increase with higher age, educational attainment, and professional experience. Employees with advanced education and longer professional tenure demonstrated more positive attitudes toward digital technologies and stronger intentions to use them in their daily work practices. Differences were also evident between clinical and administrative staff, suggesting that professional responsibilities and workflow structures shape perceptions of technology. The results highlight that technology acceptance varies significantly according to certain individual and occupational characteristics and cannot be explained by a single demographic factor alone. Overall, the findings indicate that technology acceptance in digital hospitals is not limited solely to technical infrastructure; rather, it is a multidimensional and socio-technical process shaped by individual and professional factors such as age, educational level, professional experience, and occupational group. These results emphasize the importance of targeted training programs, user-centered system design, and organizational support strategies to enhance technology acceptance. By addressing the diverse needs and expectations of different employee groups, healthcare organizations can improve the effective integration of digital technologies and support the success of digital transformation initiatives.

Keywords: Technology acceptance, Healthcare employees, Health information technologies, Digital transformation

Introduction

Digital transformation in healthcare has become a strategic priority in recent years regarding the management of clinical processes, the enhancement of service quality, and the strengthening of patient safety. At the center of this transformation, health information technologies constitute the core digital infrastructure that enables electronic generation, exchange, and management of information in healthcare settings such as hospitals and clinics (Chong et al., 2022). By facilitating the integrated management of clinical and administrative processes, these systems form the foundation of digital hospital applications and directly support healthcare organizations' objectives related to service quality, process efficiency, and patient safety. The effective functioning of this digital infrastructure is closely associated with healthcare professionals' levels of adoption and actual use of

these systems. Previous studies have demonstrated that individual and professional characteristics play a decisive role in the acceptance of health information systems.

Technology acceptance has been reported to differ significantly according to age, educational level, professional experience, and occupational role, indicating that acceptance processes in hospital settings are sensitive to individual attributes (Tetik et al., 2024). One of the most influential theoretical frameworks developed to explain technology acceptance is the Technology Acceptance Model (TAM). Within this model, perceived usefulness is defined as the degree to which an individual believes that using a particular system will enhance job performance (Davis, 1989). The model posits that users' cognitive evaluations constitute the primary determinants of behavioral intention and provides a robust theoretical foundation for understanding the adoption of health information systems. In organizational contexts, the effects of external factors on usage intention are assumed to operate through the mediating roles of perceived usefulness and perceived ease of use (Venkatesh & Davis, 2000). This finding suggests that organizational conditions and system characteristics indirectly shape technology acceptance in hospital environments. However, healthcare professionals' technology acceptance cannot be explained solely by individual cognitive evaluations. Performance expectancy, effort expectancy, and social influence have been identified as key determinants in the adoption of digital systems, particularly in the context of telehealth technologies, where these variables significantly explain acceptance behavior (Rouidi et al., 2022). This evidence indicates that technology acceptance cannot be examined independently of its social and organizational context. Given the nature of healthcare services, trust and privacy play a central role in technology acceptance. The use of health technologies necessarily involves access to highly sensitive data, including personal health information and previous medical records, highlighting the importance of ethical responsibilities and data security in digital hospital environments (Dhagarra et al., 2020). Consistently, clinical studies have shown that data security and professional accountability constitute fundamental evaluation criteria in the adoption of clinical technologies (Klaic & Galea, 2020). These findings emphasize the importance of trust-based mechanisms in the acceptance of digital systems.

Recent studies further indicate that perceived usefulness and perceived ease of use remain the primary determinants of healthcare professionals' adoption of digital systems. In the context of electronic personal health records, these two variables have been reported as the strongest predictors of adoption behavior (Kim et al., 2025). Meta-analytic evidence additionally demonstrates that technology acceptance is shaped not only by individual perceptions but also by normative and social dimensions. Perceived value and social norms have been shown to significantly explain usage intention in health information technologies, suggesting that acceptance processes in hospital settings are inherently multidimensional (Chong et al., 2022). Despite this growing body of literature, existing research predominantly addresses technology acceptance from the perspective of general users or patients, while quantitative investigations focusing on healthcare professionals in hospital settings and examining acceptance mechanisms in relation to demographic and professional characteristics remain limited. Studies that comprehensively analyze the adoption of digital hospital systems from the perspective of healthcare professionals constitute an important gap in literature. Against this background, the present study aims to quantitatively examine the technology acceptance levels of healthcare professionals working in hospital settings and to elucidate the adoption mechanisms of digital hospital systems within the framework of the core components of the TAM. By addressing healthcare professionals' technology acceptance in relation to demographic and professional variables, this study seeks to fill an important gap in the literature and to provide empirical evidence to support the effective diffusion of digital hospital applications

Literature Review

TAM constitutes one of the most widely employed theoretical frameworks for explaining the relationships among perceived ease of use, perceived usefulness, and behavioral intention in the adoption of health technologies. Studies on electronic personal health record systems emphasize that these two cognitive evaluations determine behavioral intention either directly or indirectly (Walle et al., 2023). Quantitative studies examining the role of system characteristics in healthcare professionals' technology acceptance have shown that the maturity and functionality levels of the implemented technology strengthen perceived usefulness and perceived ease of use, and that these two constructs jointly explain usage intention to a significant extent (Hussain, 2025). This evidence indicates that, in hospital settings, the acceptance process is shaped not only by individual attitudes but also by the quality and characteristics of the information system itself. In the context of professional education and clinical competency development, the validity of the TAM core has likewise been confirmed. Perceived usefulness has been reported to exert a direct effect on behavioral intention, whereas perceived ease of use functions as a fundamental component of the acceptance process through system comprehensibility and practical applicability (Chen et al., 2024). Systematic reviews evaluating the health

technology acceptance literature clearly demonstrate that perceived usefulness and perceived ease of use constitute the core of the model. These two values are identified as the most frequently employed variables in literature, and the relationship between perceived usefulness and behavioral intention is consistently among the most robustly validated links (AlQudah et al., 2021). Nevertheless, the distinct nature of healthcare services also brings the limitations of the parsimonious form of the model into focus. It has been argued that reducing TAM to its two core constructs facilitates empirical investigation yet does not always adequately capture the organizational and contextual complexity of healthcare environments (Lee, 2025). This assessment suggests that acceptance processes in hospital settings should be examined in conjunction with organizational and contextual factors.

Recent studies in the context of mobile health applications have demonstrated that perceived ease of use enhances perceived usefulness, and that both constructs exert direct effects on behavioral intention (Park et al., 2025). This finding indicates that learning burden and usability play a central role in healthcare professionals' adoption of digital applications. Similarly, studies examining healthcare professionals' acceptance behavior in telemedicine applications emphasize that perceived ease of use and perceived usefulness jointly constitute the strongest determinants of behavioral intention **(**Porat et al., 2025). This evidence suggests that simplicity of system design and expectations regarding clinical contribution are decisive in the acceptance of remote healthcare services. The effect of perceived ease of use on behavioral intention has been explained in technology acceptance literature through both direct and indirect pathways. It has been noted that ease of use may directly influence behavioral intention, while also exerting an indirect effect through perceived usefulness (Liu, 2022). This perspective highlights learning and implementation costs as critical elements in healthcare professionals' system adoption processes. Quantitative studies investigating the adoption of mobile health applications have further confirmed, through structural equation modeling, that perceived ease of use and perceived usefulness jointly exert a positive effect on behavioral intention (Serban, 2025). This result indicates that the fundamental hypothesis paths to be specified in hospital-based models are strongly supported by the existing literature. Finally, in certain contexts of digital health solutions, perceived usefulness and perceived ease of use have been shown to influence behavioral intention not directly but through attitude as a mediating variable. Attitude has been reported to constitute a decisive determinant of intention, with ease of use and usefulness primarily shaping attitudinal evaluations (Karkonasasi et al., 2023). This finding indicates that the potential mediating role of attitude should be explicitly tested when examining technology acceptance among hospital staff. Overall, prior studies show that technology acceptance among healthcare professionals is primarily shaped by perceived ease of use, perceived usefulness, and behavioral intention, and that the success of digital transformation in hospital settings largely depends on these cognitive evaluations. Accordingly, the present study aims to quantitatively test the relationships among these core constructs in a sample of healthcare professionals working in hospital environments.

Method

This study employed a quantitative research approach using survey design. Data were collected between October and December 2025. A digital questionnaire was administered to participants and distributed via Google Forms platform. The study population consisted of healthcare and administrative staff working at Gebze Fatih State Hospital who actively use health information technologies. A total of 669 questionnaires were collected. Of these, 69 questionnaires were excluded due to incomplete, erroneous, or inconsistent responses, and 600 questionnaires were retained for statistical analysis.

A. Research Design and Hypotheses

Technology Acceptance Model (TAM): The Technology Acceptance Model was employed to measure employees' levels of adoption of health information technologies. The scale consists of the subdimensions of Perceived Usefulness, Perceived Ease of Use, and Behavioral Intention to Use (Davis, 1989; Hussain et al., 2025). In the measurement tool, 5-point Likert statements are scored as "I strongly disagree (1)", "I disagree (2)", "I am undecided (3)", "I agree (4)", "I strongly agree (5)". The scale does not contain any reverse-scored statements. In our study, the Cronbach Alpha internal consistency coefficient was calculated as 0.92.

Hypotheses

To identify the factors affecting technology acceptance, the following hypotheses were formulated:

H1: There is a statistically significant difference in technology acceptance according to employees' gender.
H2: There is a statistically significant difference in technology acceptance according to employees' age groups
H3: There is a statistically significant difference in technology acceptance according to employees' educational level
H4: There is a statistically significant difference in technology acceptance according to total professional experience.
H5**:** There is a statistically significant difference in technology acceptance according to occupational group

Results and Discussion

Data were analyzed using SPSS 27.0 with a 95% confidence interval and a significance level of $p < 0.05$. Normality was assessed using the Shapiro–Wilk and Kolmogorov–Smirnov tests, and non-parametric methods were applied. The Mann–Whitney U Test was used for two-group comparisons, and the Kruskal–Wallis Test for multiple-group comparisons. The results for Hypothesis 1 (H1) are presented in Table 1. The Mann–Whitney U test indicated no statistically significant differences between male and female participants in perceived usefulness, perceived ease of use, behavioral intention to use, or overall technology acceptance.

Table 1. Evaluation of technology acceptance and its subdimensions according to gender

Sub-dimension	Gender	N	Mean Rank	U	Z	P*
Perceived Usefulness	Male	310	291.80	42252.50	-1.49	0.136
	Female	290	309.80			
Perceived Ease of Use	Male	310	294.35	43043.00	-0.988	0.323
	Female	290	307.08			
Behavioral Intention to Use	Male	310	306.97	42944.00	-1.102	0.271
	Famale	290	293.58			
Overall Technology Acceptance Scale	Male	310	295.77	43484.00	-0.749	0.454
	Famale	290	305.56			

P <0.05 indicates statistical significance. Mann–Whitney U Test.

The results for H2 are presented in Table 2 below. Statistical analyses revealed statistically significant differences in technology acceptance and all its subdimensions across age groups ($p < 0.05$). The findings demonstrate a clear age-related pattern, indicating that perceived usefulness, perceived ease of use, behavioral intention to use, and overall technology acceptance scores increase progressively with age. Younger participants reported lower levels of acceptance, whereas older participants exhibited more positive evaluations of digital technologies.

Table 2. Evaluation of technology acceptance and its subdimensions according to age group

Sub-dimension	Age Group	N	Mean Rank	χ^2	P*
Perceived Usefulness	20 Under	5	65.40	36.344	0.000*
	21-30	164	260.05		
	31-40	208	302.24		
	41-50	164	332.38		
	51-60	59	338.08		
Perceived Ease of Use	20 Under	5	91.80	44.448	0.000*
	21-30	164	245.19		
	31-40	208	308.75		
	41-50	164	328.65		
	51-60	59	364.60		
Behavioral Intention to Use	20 Under	5	151.50	27.336	0.000*
	21-30	164	261.44		
	31-40	208	299.79		
	41-50	164	330.48		
	51-60	59	340.89		
Overall Technology Acceptance Scale	20 Under	5	69.70	44.685	0.000*
	21-30	164	246.69		
	31-40	208	304.97		
	41-50	164	334.18		
	51-60	59	360.25		

P <0.05 indicates statistical significance. Kruskal–Wallis Test

The lowest mean rank scores were observed among participants aged 20 years and under, suggesting comparatively weaker perceptions of usefulness, greater perceived difficulty of use, and lower intention to adopt health information technologies in this age group. In contrast, the highest mean rank scores were obtained in the 51–60 age group, indicating stronger perceptions of usefulness, greater ease of use, and higher behavioral intention toward digital systems. This pattern suggests that older healthcare professionals may perceive digital technologies as more beneficial for clinical practice and workflow efficiency, possibly due to accumulated professional experience and a clearer understanding of the practical value of such systems. Overall, these results indicate that age constitutes a significant and direct determinant of technology acceptance in digital hospital environments and plays a critical role in shaping healthcare professionals' perceptions and adoption intentions. This finding further implies that age-specific training strategies and tailored implementation approaches may be necessary to promote more equitable and effective adoption of digital technologies across different age groups.

According to Table 3, statistically significant differences were observed in technology acceptance and all of its subdimensions across educational levels ($p < 0.001$). The results of H3 demonstrate a clear educational gradient, indicating that perceived usefulness, perceived ease of use, behavioral intention to use, and overall technology acceptance scores increase as the level of education rises. Participants with higher educational attainment reported more positive evaluations of digital technologies and stronger intentions to adopt them in their professional practice. The lowest mean rank scores were observed among high school graduates, suggesting comparatively weaker perceptions of usefulness, greater perceived difficulty of use, and lower behavioral intention toward health information technologies in this group. In contrast, the highest scores were obtained from employees holding a master's degree, indicating stronger confidence in the benefits of digital systems, greater ease of interaction with technology, and higher willingness to integrate such systems into daily clinical workflows. This pattern suggests that advanced education may enhance cognitive readiness, technology literacy, and the ability to recognize the clinical and organizational value of digital health technologies. Overall, these findings indicate that educational level constitutes a significant determinant of technology acceptance among healthcare professionals and plays a central role in shaping perceptions, usage intentions, and adoption behavior. This result further implies that differentiated training programs and continuous professional education initiatives may be essential to reduce educational disparities and promote more uniform adoption of digital technologies across healthcare staff with varying educational backgrounds.

Table 3. Evaluation of technology acceptance and its subdimensions according to educational level

Variable	Education Level	N	Mean Rank	χ^2	P*
Perceived Usefulness	High School	32	93.11	100.602	< 0.001
	Associate	180	330.92		
	Bachelor's	261	274.83		
	Master's	127	362.40		
Perceived Ease of Use	High School	32	84.02	89.131	< 0.001
	Associate	180	321.02		
	Bachelor's	261	281.05		
	Master's	127	365.22		
Behavioral Intention to Use	High School	32	118.55	70.966	< 0.001
	Associate	180	309.44		
	Bachelor's	261	287.58		
	Master's	127	360.22		
Overall Tecnology Acceptance Scale	High School	32	74.28	96.857	< 0.001
	Associate	180	321.71		
	Bachelor's	261	297.13		
	Master's	127	371.36		

$p < 0.01$ indicates statistical significance. Kruskal–Wallis Test.

Table 4 presents the results of H4. It indicates that there are statistically significant differences in technology acceptance and all its subdimensions according to total professional experience ($p < 0.001$). The mean rank scores for perceived usefulness, perceived ease of use, behavioral intention to use, and overall technology acceptance increase as years of professional experience increase. Employees with 0–1 years of experience exhibit the lowest mean ranks across all dimensions, whereas those with 11–15 years and 16 years or more of experience demonstrate the highest levels of technology acceptance. These findings suggest that greater professional experience is associated with higher acceptance and more positive evaluations of health information technologies. This pattern suggests that accumulated clinical experience may enhance professionals' ability to recognize the practical benefits of digital systems and integrate them more effectively into clinical workflows. Moreover, more experienced employees may develop greater confidence and

technological self-efficacy, thereby perceiving digital technologies as less demanding and more supportive of their professional performance.

Table 4. Evaluation of technology acceptance and its subdimensions according to total professional experience

Dimension	Years of Experience	N	Mean Rank	χ^2	p*
Perceived Usefulness	0-1 Years	14	95.54	67.992	0.000*
	2-5 Years	156	255.92		
	6-10 Years	135	281.93		
	11-15 Years	166	350.85		
	16 Years Above	129	331.30		
Perceived Ease of Use	0-1 Years	14	92.04	75.363	0.000*
	2-5 Years	156	245.86		
	6-10 Years	135	278.50		
	11-15 Years	166	358.49		
	16 Years Above	129	337.60		
Behavioral Intention to Use	0-1 Years	14	115.18	64.032	0.000*
	2-5 Years	156	262.86		
	6-10 Years	135	267.82		
	11-15 Years	166	348.93		
	16 Years Above	129	338.01		
Overall Technology Acceptance Scale	0-1 Years	14	80.21	84.647	0.000*
	2-5 Years	156	244.46		
	6-10 Years	135	271.03		
	11-15 Years	166	363.01		
	16 Years Above	129	342.57		

p <0.001 indicates statistical significance. Kruskal–Wallis Test

Table 5. Evaluation of technology acceptance and its subdimensions according to occupational group

Dimension	Profession	N	Mean Rank	χ^2	P*
Perceived Usefulness	Physician	125	361.40		
	Nurse	130	281.33		
	Other Health	172	302.23	53.510	0.000*
	Administrative	152	288.95		
	Support	21	126.10		
Perceived Ease of Use	Physician	125	367.83		
	Nurse	130	288.68		
	Other Health	172	286.42	53.756	0.000*
	Administrative	152	296.69		
	Support	21	115.79		
Behavioral Intention to Use	Physician	125	361.04		
	Nurse	130	276.90		
	Other Health	172	288.59	45.072	0.000*
	Administrative	152	304.38		
	Support	21	155.74		
Overall Technology Acceptance Scale	Physician	125	372.44		
	Nurse	130	283.75		
	Other Health	172	286.14	57.202	0.000*
	Administrative	152	297.88		
	Support	21	112.52		

p <0.001 indicates statistical significance. Kruskal–Wallis Test.

Table 5 demonstrates that there are statistically significant differences in technology acceptance and all its subdimensions across occupational groups ($p < 0.001$). The results of H5 indicate that physicians exhibit the highest mean rank scores for perceived usefulness, perceived ease of use, behavioral intention to use, and overall technology acceptance. In contrast, support service personnel display the lowest mean ranks across all dimensions, indicating comparatively weaker perceptions of usefulness, greater perceived difficulty of use, and lower intention to adopt digital technologies. Nurses, other health professionals, and administrative staff show moderate levels of technology acceptance, reflecting intermediate evaluations of both the benefits and usability of health information systems. The observed pattern suggests that professional responsibilities and proximity to clinical decision-making processes play a critical role in shaping technology acceptance. Physicians, who rely

heavily on digital systems for diagnosis, treatment planning, and clinical documentation, may perceive health information technologies as more integral to their professional performance and patient care outcomes. Conversely, support service personnel may interact with digital systems less frequently or in more limited functional contexts, thereby perceiving fewer direct benefits and greater usage barriers. Overall, these findings indicate that occupational role constitutes a significant determinant of technology acceptance in digital hospital environments and highlight the importance of role-specific system design, training strategies, and implementation policies. Tailoring digital solutions and educational interventions to the distinct needs and workflows of different professional groups may be essential to promote more balanced and effective adoption of health information technologies across hospital staff. In addition, these results suggest that uniform implementation strategies may be insufficient to address the heterogeneous expectations and competencies of diverse occupational groups. Accordingly, differentiated adoption frameworks that align technological functionalities with role-specific clinical and administrative tasks may enhance both acceptance levels and system utilization efficiency.

Conclusion

This study examined whether healthcare professionals' levels of technology acceptance in digital hospital environments differ according to demographic and professional variables. The findings indicate that technology acceptance varies significantly according to certain individual and occupational characteristics. Analyses conducted by gender revealed no statistically significant differences in perceived usefulness, perceived ease of use, behavioral intention, or overall technology acceptance ($p > 0.05$). This finding suggests that male and female healthcare professionals exhibit largely similar perceptions and acceptance levels regarding health information technologies (Alloghani, 2017). Comparisons across age groups demonstrated statistically significant differences in technology acceptance and all its subdimensions ($p < 0.05$). The results indicate that perceived usefulness, perceived ease of use, behavioral intention, and overall technology acceptance increase with age. The lowest levels were observed among participants aged 20 years and below, whereas the highest levels were found in the 51–60 age group. These findings indicate that age has a significant and direct effect on technology acceptance and related constructions (McFarland, 2001). Analyses based on educational level revealed statistically significant differences in technology acceptance and all subdimensions ($p < 0.001$). Technology acceptance scores increased with higher educational attainment, with the lowest levels observed among high school graduates and the highest among individuals holding a master's degree. This finding suggests that educational level is an important determinant in healthcare professionals' technology adoption processes (Davis, 1989; Holden & Karsh, 2010). Similarly, analyses according to professional experience revealed statistically significant differences in technology acceptance and all subdimensions ($p < 0.001$). As professional experience increased, perceived usefulness, perceived ease of use, behavioral intention, and overall technology acceptance also increased. The lowest acceptance levels were observed among employees with 0–1 year of experience, whereas the highest levels were found among those with 11 years or more of experience (Venkatesh et al., 2003). Finally, statistically significant differences in technology acceptance were identified across occupational groups ($p < 0.001$). Physicians exhibited the highest levels of technology acceptance, while support services staff demonstrated the lowest levels. Nurses, other healthcare professionals, and administrative personnel showed moderate levels of technology acceptance. This finding is consistent with the literature indicating that physicians tend to report higher perceived usefulness and technology acceptance due to their direct use of technology in clinical decision-making processes (Holden & Karsh, 2010). Overall, the findings indicate that technology acceptance in digital hospitals is not limited solely to technical infrastructure; rather, it is a multidimensional and socio-technical process shaped by individual and professional factors such as age, educational level, professional experience, and occupational group.

Scientific Ethics Declaration

* The authors declare that the scientific ethical and legal responsibility of this article published in EPSTEM journal belongs to the authors.

Conflict of Interest

* The authors declare that they have no conflicts of interest.

Funding

* This research received no specific grant from any funding agency in the public, commercial, or not-for-profit sectors.

Acknowledgements or Notes

* This article was presented as an oral presentation at the International Conference on Technology (www.icontechno.net) held in Budapest/Hungary on February 05-08, 2026.

References

AlQudah, A., Al-Emran, M., & Shaalan, K. (2021). Technology acceptance in healthcare: A systematic review. *Applied Sciences, 11*(22), 10537.

Alloghani, M. A. (2017). *The acceptance of mobile health (mHealth) technology using the Technology Acceptance Model* (Master's thesis, Liverpool John Moores University). Liverpool, United Kingdom.

Chen, B., Zhang, Y., & Li, X. (2024). Technology acceptance model perspective on the intention to participate in medical professionals' online training. *Heliyon, 10*(4), e22370.

Chong, A. Y. L., Blut, M., Zheng, S., & Chaloupka, P. (2022). Factors influencing the acceptance of healthcare information technologies: A meta-analysis. *Information & Management, 59*(3), 103604.

Davis, F. D. (1989). Perceived usefulness, perceived ease of use, and user acceptance of information technology. *MIS Quarterly, 13*(3), 319–340.

Dhagarra, D., Goswami, M., & Kumar, G. (2020). Impact of trust and privacy concerns on technology acceptance in healthcare. *International Journal of Medical Informatics, 141*, 104249.

Holden, R. J., & Karsh, B. T. (2010). The Technology Acceptance Model: Its past and its future in health care. *Journal of Biomedical Informatics, 43*(1), 159–172.

Hussain, A., Ma, Z., Li, M., Jameel, A., Kanwel, S., Ahmad, S., & Ge, B. (2025). The mediating effects of perceived usefulness and perceived ease of use on nurses' intentions to adopt advanced technology. *BMC Nursing, 24*, 33.

Hussain, M. (2025). Technology sophistication, perceived usefulness, perceived ease of use and intention to use health information systems. *Clinical Practice, 15*(10), 181–194.

Karkonasasi, K., Tsironis, L., & Karasavvoglou, A. (2023). Determinants of digital health wearable acceptance among nurses. *Vaccines, 11*(13), 1331.

Kim, J., Lee, H., & Park, Y. (2025). Healthcare professionals' acceptance of electronic personal health records. *Journal of Medical Internet Research, 27,* e65269.

Klaic, M., & Galea, M. P. (2020). Using the technology acceptance model to identify factors that predict likelihood to adopt tele-neurorehabilitation. *Frontiers in Neurology, 11,* 580832.

Lee, A. T. (2025). Technology acceptance in healthcare: A critical review of TAM applications. *Healthcare, 13*(2), 250.

Liu, X. (2022). Effects of perceived ease of use on behavioral intention in health technologies. *Clinical Practice, 15*(1), 181–191.

McFarland, D. J. (2001). The role of age and efficacy on technology acceptance: Implications for e-learning. Proceedings of *WebNet 2001 World Conference on the WWW and Internet.* ERIC, ED466607.

Park, J. H., Lee, S., & Do, Y. (2025). Perceived ease of use, perceived usefulness, and behavioral intention in mobile health applications. *Healthcare, 13*(5), 596.

Parsons, K., Calic, D., Pattinson, M., Butavicius, M., McCormac, A., & Zwaans, T. (2017). The human aspects of information security questionnaire (HAIS-Q): Two further validation studies. *Computers & Security, 66*, 40–51.

Porat, Packer, T., Shachak, A., & Elhadad, N. (2025). Acceptance of telemedicine among healthcare professionals: A technology acceptance model approach. *Behavioral Sciences, 15*(10), 1367.

Rouidi, M., Elouadi, A. E., Hamdoune, A., Choujtani, K., & Chati, A. (2022). TAM-UTAUT and the acceptance of remote healthcare technologies by healthcare professionals. *Informatics in Medicine Unlocked, 31*, 100987.

Serban, A. M. (2025). Mobile health adoption and technology acceptance: A structural equation modeling approach. *Clinical Practice, 15*(10), 181–200.

Tetik, G., Türkeli, S., Pınar, S., & Tarım, M. (2024). Health information systems with technology acceptance model approach: A systematic review. *International Journal of Medical Informatics, 188,* 105510.

Venkatesh, V., & Davis, F. D. (2000). A theoretical extension of the technology acceptance model: Four longitudinal field studies. *Management Science, 46*(2), 186–204.

Venkatesh, V., Morris, M. G., Davis, G. B., & Davis, F. D. (2003). User acceptance of information technology: Toward a unified view. *MIS Quarterly, 27*(3), 425–478.

Walle, J., Blut, M., Zheng, S., & Chaloupka, P. (2023). Acceptance of electronic personal health records: A technology acceptance perspective. *BMJ Health & Care Informatics, 30*(1), e100707.

Author(s) Information

Salih Gol
Gebze Technical University
Gebze, Kocaeli, Türkiye
ORCID iD: https://orcid.org/0009-0003-5487-6964

Ceren Cubukcu - Cerasi
Gebze Technical University
Gebze, Kocaeli, Türkiye
ORCID iD: https://orcid.org/0000-0002-9253-2826
*Contact e-mail: *cerencubukcu@gtu.edu.tr*

To cite this article:

Gol, S., & Cubukcu-Cerasi, C. (2026). Understanding technology acceptance among healthcare employees: A quantitative assessment for hospitals. *The Eurasia Proceedings of Science, Technology, Engineering and Mathematics (EPSTEM), 39,* 81-89.